Computer simulation of time-resolved optical imaging of objects hidden in turbid media

Michielsen, K.; Raedt, H. De; Przeslawski, J.; Garcia, N.

Published in:
Physics Reports

DOI:
10.1016/S0370-1573(98)00023-4

Publication date:
1998

ELSEVIER

Physics Reports 304 (1998) 89–144

PHYSICS REPORTS

Computer simulation of time-resolved optical imaging of objects hidden in turbid media

K. Michielsen[a], H. De Raedt[a,*], J. Przeslawski[b], N. Garcia[b]

[a] *Institute for Theoretical Physics and Materials Science Centre, University of Groningen, Nijenborgh 4, NL-9747 AG Groningen, The Netherlands. h.a.de.raedt@phys.rug.nl*

[b] *Laboratorio de Física de Sistemas Pequeños y Nanotecnología, Consejo Superior de Investigaciones Científicas, Serrano 144, Madrid E-28006, Spain. nikolas.garcia@fsp.csic.es*

Received January 1998; editor: M.L. Klein

Contents

* Corresponding author.

PII S0370-1573(98)00023-4

COMPUTER SIMULATION OF TIME-RESOLVED OPTICAL IMAGING OF OBJECTS HIDDEN IN TURBID MEDIA

K. MICHIELSEN[a], H. DE RAEDT[a], J. PRZESLAWSKI[b], N. GARCIA[b]

[a] Institute for Theoretical Physics and Materials Science Centre, University of Groningen, Nijenborgh 4, NL-9747 AG Groningen, The Netherlands. h.a.de.raedt@phys.rug.nl
[b] Laboratorio de Física de Sistemas Pequeños y Nanotecnología, Consejo Superior de Investigaciones Científicas, Serrano 144, Madrid E-28006, Spain. nikolas.garcia@fsp.csic.es

ELSEVIER

AMSTERDAM – LAUSANNE – NEW YORK – OXFORD – SHANNON – TOKYO

Abstract

We review research on time-resolved optical imaging of objects hidden in strongly scattering media, with emphasis on the application to breast cancer detection. A method is presented to simulate the propagation of light in turbid media. Based on a numerical algorithm to solve the time-dependent diffusion equation, the method takes into account spatial variations of the reduced scattering and absorption factors of the medium due to the presence of objects as well as random fluctuations of these factors. It is shown that the simulation method reproduces, without fitting, experimental results on tissue-like phantoms. Using experimental and simulation results, an assessment is made of the reliability for extracting the reduced scattering and absorption coefficients of the medium from time-resolved reflection and transillumination data. The simulation technique is employed to study the conditions for locating mm-sized objects immersed in a turbid medium, by direct, time-resolved imaging. We discuss a simple method to enhance the imaging power of the time-resolved technique. The mathematical justification of the method, as well as some applications to simple problems, is given. The simulation technique is employed to demonstrate the effectiveness of the data processing technique. Results of time-resolved reflection experiments and simulations are presented, showing that the use of the latter allow us to locate 1 mm diameter objects under conditions which would prevent detection otherwise. Our results demonstrate that the combination of simulation and the appropriate processing of the diffusive part of the time-resolved reflected or transmitted light intensity may substantially increase the potential of the time-resolved near-infrared diffusive light imaging technique as a diagnostic tool for breast cancer detection.

PACS: 87.59. − e; 42.30. − d

Keywords: Time-resolved imaging; Diffusion equation; Breast cancer

1. Introduction

Imaging through scattering media is a challenging problem and has motivated extensive scientific research. The fields of application vary widely, ranging from atmospheric science and oceanics to medicine. One potential application, breast-tissue imaging, has been drawing special attention. Breast cancer is the most common cancer in women and one of the leading causes of death in women. In many cases the cancer can be cured when it is small and localized in the breast. Hence, non-invasive diagnostic methods for detection of breast cancer at an early stage are of great importance. A successful screening method should be able to distinguish small tumors from surrounding healthy tissue before metastasis occurs [1]. The ultimate goal is to image and characterize millimeter-sized objects in 40–100 mm-thick human tissue [2]. The female breast is also prone to benign diseases. Therefore it is also very important to discriminate between benign and malignant lesions.

Recent developments in breast imaging and their present clinical importance is reviewed in Ref. [3]. The most common imaging method at this moment, X-ray mammography, is not very sensitive to differences between normal fibrotic tissue and cancer, making it less suitable for imaging young dense breasts which usually are fibrotic [4,5]. Moreover both X-ray and radioisotope imaging techniques expose the body to potentially harmful, ionizing radiation and increase the risk of contracting cancer. Therefore, one would like to avoid using these techniques for extensive routine screening. Ultrasound lacks the resolution to detect objects with linear dimension smaller than a few millimeters and, like X-ray mammography, cannot distinguish between benign and malignant tumors [2,6]. Magnetic resonance imaging of the breast [7] is a very powerful technique with submillimeter resolution and the ability to detect specific chemicals but its high operating costs [6,8] make it less suited as a routine screening modality [2,5,8]. Several clinical experiments have been performed to study the (dis)advantages of each of the above-mentioned methods [9–13].

The need for diagnostic imaging equipment that is non-invasive, safe, compact and capable of monitoring tissue chemistry in vivo, together with the advent of picosecond pulse lasers in the near-infrared wavelength regime and fast optical detectors able to resolve such pulses, has increased the interest in optical techniques as a tool for early breast cancer detection [3,14–28].

Already in the Victorian age doctors conducted the first experiments in mammography using candle light [2]. In the mid-1800s, British physicians used tissue transillumination to detect scrotal cancer by holding a lamp behind the testes and observing the shadows resulting from the presence of tumors. Ewen [29] first investigated light transmission through the breast in the late 1920s by exploring various light sources and by visual observation of the transmitted light. Cutler improved this technique by using a special tungsten lamp as a light source [29]. The instrumentation used had problems in providing enough light intensity for the human eye to discern variations in the tissue. Although various attempts [4,30–32] were made to improve the instrumentation, the sensitivity of the human eye or photographic material appears to be insufficient to differentiate the minute variations in light intensities corresponding to healthy and cancerous tissue. Initial attempts to image the breast using continuous-wave near-infrared light intensity measurements demonstrated very poor spatial resolution and indicated that this breast transillumination methods had no utility as a screening method [33]. According to a more recent study [34] conventional light-scanning equipment does not add any value to physical examination and

mammography in breast cancer diagnosis. Diagnostic equipment [35,36] based on continuous wave illumination and modified X-ray backprojection tomographic algorithms [35–37] has been developed. Time-resolved transillumination with short laser pulses has also been studied for the extraction of tissue parameters and tumor detection [21,38]. An alternative is to modulate the intensity of the light source at frequencies between some ten to several hundred megahertz and to measure the demodulation and phase shift of the transmitted light [39]. Recently, by the use of frequency-domain techniques, optical mammography was evaluated in a clinical study [40]. Within approximately 3 min transillumination images of a compressed mamma were obtained by scanning. Current time-resolved techniques require much longer times to record images [1,38,41].

At present, none of the techniques described above are in a clinically usable stage because most of them do not (yet) provide a reliable distinction factor between normal and cancerous tissue.

1.1. Breast tissue imaging: Physical basis

For diagnostic optical imaging the wavelengths of interest are in the range 650–1300 nm, i.e. the so-called therapeutic window: Near-infrared light is not as strongly absorbed by human tissue than visible light [4,42] and so will have higher transmission and less likelihood of causing burns. Near-infrared transillumination can be used to look at the structure and function of biological systems [43,44] and is now used for various applications including the monitoring of blood oxygenation in tissue [45], muscle oxygenation [46,47] and physiology [48], brain oxygenation in new-born infants [2,49–52] and adults [53,54], and the flow of blood and specific chemicals, such as oxyhaemoglobin or glucose, in arteries close to the surface of the skin. The latter provides a noninvasive way for diabetics to monitor their blood glucose levels [2,55–57]. In contrast to optical mammography these applications may have less stringent technical requirements because either the tissue does not scatter very much, such as the brains of newborn babies [2], or the tissue is only a few millimeters thick.

Breast imaging with red and near-infrared light relies on the differences in the optical properties of breast tissue and cancerous tissue. Tumors can be regarded as optical inhomogeneities in the sense that they have other absorption and scattering factors than the surrounding healthy tissue. In cancerous tissue the incident light is strongly absorbed due to the higher blood content in the neovascular zone surrounding most malignant tumors [58,59]. The absorption of light in tissues is due to chromophores such as the heme pigment of hemoglobin, myoglobin, and bilirubin, the cytochrome pigments of the respiratory chain in the mitochondria, and melanin pigment [60,61]. The light scattering in tissues is due to discontinuities in refractive index on the microscopic level, such as the aqueous-lipid membrane interfaces surrounding and within each cell or the collagen fibrils within the extracellular matrix [60,61].

Light propagation in breast tissue, which is a strong scattering medium, may be described by the time-dependent diffusion equation (see below) involving two optical properties: The absorption factor μ_a and the reduced scattering factor μ_s'. For breast tissue there appears to be a large variation in the values for the reduced scattering and absorption factor. For various in vitro breast tissue samples the reduced scattering factor $\mu_s' = 0.7\text{–}1.4\,\mathrm{mm}^{-1}$ and the absorption factor $\mu_a = 0.02\text{–}0.07\,\mathrm{mm}^{-1}$, for wavelengths near 800 nm [62,63]. In vitro measurements on breast tissue for wavelengths of 653 nm suggest that $\mu_s' \approx 0.4\,\mathrm{mm}^{-1}$ and $\mu_a < 0.02\,\mathrm{mm}^{-1}$ [64]. In vivo measurements

at 800 nm on six volunteers suggested for $\mu_s' = 0.72$–$1.22\,\mathrm{mm}^{-1}$ and for $\mu_a = 0.0017$–$0.0032\,\mathrm{mm}^{-1}$ [38]. A smaller study on two volunteers of 30 and 58 years old, yielded values of $\mu_s' = 1.13$ and $0.76\,\mathrm{mm}^{-1}$ and $\mu_a = 0.0068$ and $0.0028\,\mathrm{mm}^{-1}$, respectively at a wavelength of 753 nm [65]. In vivo experiments on one volunteer having a rather large abdomen and back tumor show that tumor and normal tissue optical properties and physiological parameters differ substantially within the studied individual [66]. The absorption factors of tumor tissue are 2–3 times larger than the absorption factor of normal tissue and this at all studied wavelengths [66]. The scattering changes are less significant (the reduced scattering factors of tumor tissue are somewhat smaller than the reduced scattering factors of normal tissue), but exhibit consistent wavelength-dependent behavior.

In time-resolved optical imaging experiments on breast phantoms one generally assumes that the reduced scattering factor of the breast tissue is of the order of $1\,\mathrm{mm}^{-1}$, whereas the absorption factor of the breast tissue is of the order of $0.01\,\mathrm{mm}^{-1}$, at a wavelength of 800 nm [24,67,68].

1.2. Light propagation in turbid media

The dilemma encountered with optical imaging of human breasts is that although the wavelength of the light can be chosen such as to minimize the absorption it is impossible to avoid the blurring of the images due to strong scattering by the tissue. In contrast to X-ray mammography in which the incident X-rays are usually scattered only once, most near-infrared light travelling through a few centimeters of tissue has been scattered several thousand times before it reaches the detector [62,64].

Light entering a strongly scattering medium (e.g. the woman breast) that contains one or more small objects (with reduced scattering and/or absorption coefficients different from that of the surrounding medium, e.g. malignant tumors) can arrive at a detector by two different routes:

(1) By ballistic transport, in which the light travels without scattering through the sample to yield a projection of the object(s). This light arrives first at the detector, within a time interval $[0, \tau_1]$ where $\tau_1 \approx l/v$, l is the distance between the source and the detector and v is the velocity of light in the medium. For $l = 6$ cm and $v = 220$ km/s, $\tau_1 \approx 300$ ps. The unscattered light (ballistic component) can be selected by means of a very fast (ps) time gate. A large variety of time-gating techniques are developed based on the degree of polarization [69–72] coherent detection [73–75] and selection of the length of the photon paths [1,15,18,38,76–80]. A systematic study of the time-gating technique has shown that it is highly sensitive with respect to spatial variations in the absorption or reduced scattering factors [38], in particular under conditions that are similar to those of biological systems of interest [38]. Recent experiments have shown that the spatial resolution of the time-gating technique can also be obtained with the absorption method [81]. However, any technique based on the detection of unscattered light only for image formation is subject to intrinsic physical limitations. As the signal at the detector contains only an exponentially small fraction of the number of photons in the light pulse emitted by the source, the signal-to-noise ratio is low. In addition, the intensity of these photons decreases exponentially with l, effectively limiting the tissue sample size. For applications to optical breast imaging, the intensity of these photons seems to be too low to be of practical use (there obviously is a limitation on the amount of power of the incident light pulse) [38].

(2) By diffusion, in which the light is scattered many times before it reaches the detector. In this regime the strong scattering by the medium blurs the variations in the transmitted or reflected light

that result from the local (small) variations of the absorption and diffusion factor induced by the objects immersed in the medium. Only if the diffusion factors of the object and the medium differ considerably, direct detection (i.e. without image processing) is possible [82]. Diffusive light imaging can be performed in the frequency domain [39,83–86] or in the time domain [23–25,38,87]. In the former case a continuous intensity-modulated light source is used to generate diffusive monochromatic light-intensity waves in the medium. In many respects these waves behave like damped propagating waves [83–97]. Inverse scattering techniques in combination with perturbation schemes have been employed to compute spatial variations in the absorption factor and the diffusion coefficient (and hence the location of the objects) from the measured phase and amplitude of these waves at various source and detector positions [83,98]. In the time domain, short light pulses are used to excite a spectrum of light-intensity waves, the frequency-range being determined by the scattering and absorption factors of the medium. This approach requires the use of a detection system with a time resolution that is sufficiently high to cover the relevant range of frequencies. In theory the time and frequency-domain data are intimately related through Fourier transformation. However, usually the former contains more information because frequency-domain measurements are carried out for at most a few selected modulation frequencies and this information is not sufficient to determine the time-dependent response of the medium to a light pulse. For this reason the emphasis of this paper is on simulations and experiments performed in the time-domain. In practice, the differences between frequency and time-domain methods are mainly technical, and the choice is a trade off between sensitivity, time resolution, complexity and cost.

1.3. Outline

The organization of the paper is as follows. Section 2 introduces the model, i.e. the time-dependent diffusion equation (TDDE), and describes the algorithm that we employ to solve the TDDE. In Section 3 the simulation results for tissue-like phantoms are compared to experimental data, establishing the validity of the TDDE model and the simulation approach. A discussion of the limitations of the direct imaging approach is given in Section 4. In Section 5 we assess the quality of the estimates of optical properties of the tissue, as obtained from the analysis of the time-resolved transillumination and reflection data. In Section 6 we give the theoretical justification of the time-resolved image processing method that facilitates the detection of mm-sized objects. Sections 7 and 8 are devoted to the assessment of the effectiveness of the image processing method. Section 9 summarizes our results.

2. Model

Most of the light entering a turbid medium (possibly containing one or more small objects with reduced scattering and/or absorption factors different from those of the medium) is scattered many times before it reaches the detector. For weakly absorbing media the propagation of the light is, to a good approximation, described by the time-dependent diffusion equation [39,99,100] (TDDE)

$$\partial I(\boldsymbol{r},t)/\partial t = \nabla\cdot D(\boldsymbol{r})\nabla I(\boldsymbol{r},t) - v\mu_{\mathrm{a}}(\boldsymbol{r})I(\boldsymbol{r},t) + S(\boldsymbol{r},t)\ , \tag{1}$$

where $I(\boldsymbol{r},t)$ is the intensity of light at a point $\boldsymbol{r}$ and at time t,

$$D(\boldsymbol{r}) = v/3[\mu_s'(\boldsymbol{r}) + \mu_a(\boldsymbol{r})] \,, \tag{2}$$

is the diffusion coefficient, $\mu_s'(\boldsymbol{r})$ is the reduced scattering factor, $\mu_a(\boldsymbol{r})$ denotes the absorption factor, and v is the velocity of light in the medium in the absence of objects. The light source is represented by $S(\boldsymbol{r},t)$. The presence of objects in the medium is reflected by spatial variations in the absorption factor and/or the reduced scattering factor (and hence also in the diffusion coefficient). In general, both the absorption and the reduced scattering factor of the medium will fluctuate randomly around their spatial averages, denoted $\bar{\mu}_a$ and $\bar{\mu}_s'$, respectively. For weakly absorbing media, $\bar{\mu}_a \ll \bar{\mu}_s'$.

For purposes of notation it is convenient to write the intensity distribution as a "vector" $|I(t)\rangle$, i.e. $I(\boldsymbol{r},t) = \langle \boldsymbol{r}|I(t)\rangle$ where $\langle .|.\rangle$ denotes the inner product of two vectors. The intensity at a point $\boldsymbol{r}$ and time t is given by $\langle \boldsymbol{r}|e^{-tH}|s\rangle$, where $|s\rangle$ is the intensity distribution at time $t = 0$. Obviously, since we are dealing with intensities, $\langle \boldsymbol{r}|e^{-tH}|s\rangle \geq 0$ for any $\boldsymbol{r}$ and any intensity distribution s.

The formal solution of Eq. (1) reads

$$|I(t)\rangle = e^{-tH}\left[|I(0)\rangle + \int_0^t dt'\, e^{t'H}|S(t')\rangle\right], \tag{3}$$

with the time evolution of the light intensity governed by the "Hamiltonian"

$$H = -\nabla\cdot D(\boldsymbol{r})\nabla + V(\boldsymbol{r}) \,, \tag{4a}$$

and where, for later convenience, we have introduced the "potential'

$$V(\boldsymbol{r}) = v\mu_a(\boldsymbol{r}) \,. \tag{4b}$$

According to Eq. (3) the time evolution of the light intensity at time $t + \tau$ is related to the light intensity at time t through

$$|I(t+\tau)\rangle = e^{-\tau H}\left[|I(t)\rangle + \int_0^\tau d\tau'\, e^{\tau' H}|S(t+\tau')\rangle\right], \tag{5}$$

where τ denotes the time step. From Eq. (5) it follows that all we need to solve the TDDE (1) is an algorithm to compute $\exp(-\tau H)A(\boldsymbol{r})$ for arbitrary $A(\boldsymbol{r})$.

Denoting the one-sided Fourier transform of $|A(t)\rangle$ by $|A_\omega\rangle = \int_0^\infty dt\, e^{-i\omega t}|A(t)\rangle$, Eq. (1) can be written as

$$|I(0)\rangle + i\omega|I_\omega\rangle = -H|I_\omega\rangle + |S_\omega\rangle \,, \tag{6a}$$

or

$$|I_\omega\rangle = (H + i\omega)^{-1}(|S_\omega\rangle - |I(0)\rangle) \,, \tag{6b}$$

showing that $|I_\omega\rangle$ is the solution of a time-independent diffusion equation, with a complex, frequency-dependent "absorption" coefficient $v\mu_a(\boldsymbol{r}) + i\omega$. Frequency-domain experiments provide direct information about $|I_\omega\rangle$, for ω corresponding to the frequency of the amplitude modulation of the light source intensity [101–103]. The intensity $|I(t)\rangle$ can be retrieved from I_ω by solving Eq. (6) for several ω and performing the inverse Fourier transform. However, in numerical work it is more efficient to solve Eq. (1) directly in the time domain. On the other hand, if only the solution of

Eq. (6) for a few selected frequencies is desired, solving Eq. (6) for these frequencies may be the numerical method of choice.

For practical applications the TDDE (1) and the formal solutions (3) and (5) have to be supplemented by boundary conditions that mimic those of the actual experimental set-up. For the applications we have in mind these boundary conditions take a non-trivial form: Usually, the surface of the medium (e.g. a breast) has an irregular shape and is partially absorbing and partially reflecting. Furthermore, the source and detectors are not in direct contact with the medium as the light enters and leaves the sample through the skin (surface). Except for the shape of the sample, incorporating all these elements into the boundary conditions is rather difficult and it is therefore expedient to assume that the surface is reflecting and/or absorbing. Comparison of simulation and experimental data should tell us if this is a reasonable assumption or not.

2.1. Algorithm

We have developed an algorithm to compute $\exp(-\tau H)A(\boldsymbol{r})$ [104], based on the fractal decomposition of matrix exponentials proposed by Suzuki [105]. It is accurate to second order in the spatial mesh size δ and to fourth order in the temporal mesh size τ. Conceptually the algorithm is closely related to the one that we developed for the time-dependent Schrödinger equation [106]. The first step in setting up a numerical method to solve the TDDE (1) is to discretize the derivatives with respect to the spatial coordinates. The simplest approximation scheme having satisfactory properties is [107]

$$K_x I(\boldsymbol{r},t) \equiv -\frac{\partial}{\partial x}\left(D(\boldsymbol{r})\frac{\partial}{\partial x}I(\boldsymbol{r},t)\right)\Big|_{\boldsymbol{r}=(i\delta,j\delta,k\delta)} \approx -\frac{D_{i+1,j,k}+D_{i,j,k}}{2\delta^2}I_{i+1,j,k} + \frac{D_{i+1,j,k}+2D_{i,j,k}+D_{i-1,j,k}}{2\delta^2}I_{i,j,k} - \frac{D_{i-1,j,k}+D_{i,j,k}}{2\delta^2}I_{i-1,j,k}\,, \tag{7}$$

where $I_{i,j,k} = I(\boldsymbol{r}=(i\delta,j\delta,k\delta))$ and $D_{i,j,k} = D(\boldsymbol{r}=(i\delta,j\delta,k\delta))$. For the derivatives with respect to y and z we use expressions similar to Eq. (7).

Proceeding as in the case of the time-dependent Schrödinger equation, the time-step operator $\mathrm{e}^{-\tau H}$ is approximated by a product of matrix exponentials. An approximation correct to second order in the time step τ is given by [108,109]

$$\mathrm{e}^{-\tau H} \approx \mathrm{e}^{-\tau K_z/2}\mathrm{e}^{-\tau K_y/2}\mathrm{e}^{-\tau K_x/2}\mathrm{e}^{-\tau V}\mathrm{e}^{-\tau K_x/2}\mathrm{e}^{-\tau K_y/2}\mathrm{e}^{-\tau K_z/2}\,. \tag{8}$$

Instead of using fast-fourier-transform techniques [110] to compute the quantities such as $\mathrm{e}^{-\tau K_x/2}A(\boldsymbol{r})$, we replace $\mathrm{e}^{-\tau K_x/2}$ by a first-order product-formula approximation and obtain [111]

$$\mathrm{e}^{-\tau K_x/2} \approx X(\tau/2) = \prod_{j,k}\left[\prod_{i\in\mathscr{E}}\frac{1}{2}\begin{pmatrix}1+\mathrm{e}^{-\tau a_{i,j,k}} & 1-\mathrm{e}^{-\tau a_{i,j,k}}\\ 1-\mathrm{e}^{-\tau a_{i,j,k}} & 1+\mathrm{e}^{-\tau a_{i,j,k}}\end{pmatrix}^{(i,i+1)}\right] \times\left[\prod_{i\in\mathscr{O}}\frac{1}{2}\begin{pmatrix}1+\mathrm{e}^{-\tau a_{i,j,k}} & 1-\mathrm{e}^{-\tau a_{i,j,k}}\\ 1-\mathrm{e}^{-\tau a_{i,j,k}} & 1+\mathrm{e}^{-\tau a_{i,j,k}}\end{pmatrix}^{(i,i+1)}\right], \tag{9}$$

where the triples (i,j,k) appearing in Eq. (9) represent a point on the lattice, $\mathscr{E}$ and $\mathscr{O}$ are the sets of even and odd numbers, respectively, and $a_{i,j,k} = \delta^{-2}(D_{i,j,k} + D_{i+1,j,k})/2$. The superscripts $(i, i+1)$ labeling the two-by-two matrices indicate that this matrix operates on the vector $(I_{i,j,k}, I_{i+1,j,k})$ only. In Eq. (8) we replace $e^{-\tau K_y/2}$ and $e^{-\tau K_z/2}$ by similar approximations, $Y(\tau/2)$ and $Z(\tau/2)$, respectively. The resulting product formula remains correct to order τ^2. It is also of interest to note that all the matrix elements of both $e^{-\tau K_x/2}$ and $X(\tau/2)$ are positive so that approximation (9) has the desirable feature that it will never lead to negative light intensities.

For $V(\boldsymbol{r}) \geq 0$ (the case of interest) the explicit, second-order algorithm defined by

$$e^{-\tau H} \approx S_2(\tau) = Z(\tau/2)Y(\tau/2)X(\tau/2)e^{-\tau V}X(\tau/2)Y(\tau/2)Z(\tau/2) \tag{10}$$

is unconditionally stable. Indeed, if $\|M\|$ denotes the eigenvalue of the matrix M of largest absolute value, we have

$$\|Z(\tau/2)Y(\tau/2)X(\tau/2)e^{-\tau V}X(\tau/2)Y(\tau/2)Z(\tau/2)\| \leq 1 \,, \tag{11}$$

which is the condition expressing numerical stability of the scheme [107].

The accuracy of the second-order algorithm may be insufficient if we want to solve the TDDE for long times. In practice, this is only a minor complication because the second-order algorithm can be reused to build an algorithm that is correct to fourth-order in the time step. According to Suzuki's fractal decomposition [105],

$$S_4(\tau) = S_2(p\tau)S_2(p\tau)S_2((1-4p)\tau)S_2(p\tau)S_2(p\tau) \tag{12}$$

will be an approximation to the time-step operator that is correct to fourth-order in τ provided $p = (4 - 4^{1/3})^{-1}$. In our simulations we have used both (10) and (12) and obtained quantitatively similar results.

The contribution from the source $S(\boldsymbol{r}, t)$ is computed using the standard Simpson rule [112]

$$e^{-\tau H}\int_0^\tau d\tau'\, e^{\tau' H}|S(t+\tau')\rangle \approx \frac{\tau}{6}(e^{-\tau H}|S(t)\rangle + 4e^{-\tau H/2}|S(t+\tfrac{\tau}{2})\rangle + |S(t+\tau)\rangle) \,, \tag{13}$$

which is correct to fourth-order in τ.

From the structure of Eq. (9) and $S_2(\tau)$ it is clear that the propagation of light over a time step τ has been reduced to elementary operations: Repeated multiplications of two elements of a vector by the corresponding two elements of another vector (in the case of $e^{-\tau V}$), or of matrix-vector multiplications involving two-by-two matrices only. The resulting algorithm is fast, stable and flexible. For practical applications to the tumor detection problem it is important that the software can deal with irregularly shaped samples. As the Suzuki-product-formula-based algorithm presented above operates on numbers labeled by real-space indices only, it is as easy to solve the TDDE for a particular shape as it is to solve the TDDE for a rectangular box.

2.2. Simulation software

Our current version of the software solves Eq. (1) in two and three dimensions subject to perfectly reflecting and/or perfectly absorbing boundary conditions. The intensity of light transmitted by the sample is collected by detectors located at $\boldsymbol{r} = (L_x, y, z)$, where L_x denotes the size of the simulation box in the direction of the incident light [113]. The reflected light intensity is recorded

at $\boldsymbol{r} = (0, y, z)$. The light source is placed at $x = 0$ [i.e. $S(\boldsymbol{r}, t) = 0$ unless $\boldsymbol{r} = (0, y, z)$]. We have carried out simulations using sources of variable size, including the cases of a point source [$S(\boldsymbol{r}, t) = S_0(t)\delta(x)\delta(y - y_0)\delta(z - z_0)$] and uniform illumination [$S(\boldsymbol{r}, t) = S_0(t)\delta(x)$]. At $t = 0$ the source starts to illuminate the system, until $t = t_p$ when it is turned off. Detection of the light intensity starts at t_d ($t_d > t_p$). Our simulation software allows the detectors to record the instantaneous or the time-integrated light intensity.

Our software generates real-time images when run on a PC or data files suitable for processing by IBM's Data Explorer. The pictures are then collected into digital video's (Autodesk Animator .FLC format, typically less than 1 Mb/video) suitable for playback on PC's and X-window systems. These video's give a good impression of how the light intensity diffuses through the medium. Included in these video's are the (time-dependent) intensities recorded by the detectors. The digital video's also serve as an archive for the simulation results.

For a representative two-dimensional (2D) sample of 71 mm × 71 mm, using a mesh size of $\delta = 1$ mm ($L_x = L_y = 71$), it takes about 1 min on a Pentium Pro 200 MHz system to carry out 1000 time steps, including data analysis and visualization. On a Pentium II 266 MHz system it takes about 2.8 s to carry out the same calculation but without data analysis and visualization. Calculation of the time evolution of the light intensity for a three-dimensional (3D) grid of $63 \times 63 \times 63 = 250047$ points and 1000 time steps takes 390 s on the same machine. The number of (floating point) operations required to solve the TDDE by the algorithm based on the fractal decomposition of matrix exponentials [104] scales linearly with the dimensionality of the system, the number of time steps and the total number of grid points. Clearly the CPU times obtained for the (representative) 2D and 3D simulations do not seem to reflect this scaling behavior: On the basis of the CPU time for the 3D system we would expect the 2D simulation to take $2 \times 390 \times 71 \times 71/(3 \times 63 \times 63 \times 63) \approx 5.2$ s, almost a factor two more than actually measured. This extra speed-up of a factor two is due to the fact that the 2D problem fits in the cache memory of the Pentium II processor.

Calculation of the time evolution of the light intensity for a 3D grid of $63 \times 63 \times 63 = 250\,047$ points and 1480 time steps takes 6 minutes on a Cray C98 (single processor), 42 minutes on a SGI Power Challenger (single processor), and 65 minutes on an IBM RS/6000 model 43P workstation, including data analysis and visualization processing.

For exploratory purposes it is advantageous to simulate 2D systems: simulation and visualization only takes a few minutes. Then, for selected cases, we simulate the corresponding 3D system. On a qualitative level there seems to be little difference between the results obtained from 2D or 3D simulations. In fact, we never encountered a 3D simulation that forced us to change a conclusion drawn from 2D simulation data.

As the effect of particular implementations, compilers and computer systems on the performance of specific simulation algorithms can be substantial, it is difficult to compare different approaches on a quantitative basis but it may be of interest to compare, on a conceptual level, our approach with others. Techniques which have been developed to calculate light propagation in turbid media can be classified into stochastic methods, such as the Monte Carlo (MC) simulations [114–123] and random walk models [124,125], or deterministic methods which are based on the solutions of the diffusion equation.

MC simulations trace a large number of individual paths of photons propagating through a scattering medium. The scattering events are determined by a probability function that matches

the scattering coefficient. At each scattering event part of the photons are absorbed. The amount of absorption is determined by the absorption coefficient. The scattering angle is given by the scattering phase function. A MC algorithm has the advantages of being conceptually simple and of being flexible with respect to geometry, phase functions and boundary conditions. A disadvantage of MC simulations is the large amount of computer time needed to obtain statistically good quality data.

In general, the numerical methods based on the solution of the diffusion equation are much faster than the MC methods to describe the light propagation in tissue, if the scattering and absorption mechanisms allow the use of the diffusion approximation.

The diffusion equation, including its time-dependent form, can be solved analytically for a homogeneous medium and rather simple geometries [88,126]. More flexible than analytical methods are numerical methods, such as the finite element method (FEM) [127–132], the finite difference method (FDM) [24], the method of exact enumeration [133] and our method [104], described above. The basic idea of the FEM is that a model that satisfies the time-dependent diffusion equation is divided into elements, and an approximate solution to the equation is calculated over each element. The solution for the whole model can be derived from the algebraic solutions for each element. The mean time of flight can be calculated directly from the first moment of the time-dependent light intensity [129]. In the FDM the diffusion equation is converted into a finite difference equation for finite steps of the spatial variables and the temporal variable. The method of exact enumeration is an iterative method that accounts for the spatial and temporal distribution of photons after a discrete pulse is applied to a scattering medium. The method is equivalent to performing MC calculations for movement on a lattice, but by use of the method of exact enumeration, all random-walk configurations are taken into account properly even when only a few photons would reach a site as realizations of MC experiments. The algorithm we use is identical to the FDM as far as the treatment of the spatial variables is concerned.

3. Comparison with experiment

We have tested our software and the validity of the TDDE model by comparing simulation data [104,134] with the experimental results of Ref. [38], concerning a range of optical parameters which from the point of view of breast imaging range from realistic to unrealistic. We have simulated exactly the same systems as those studied in Ref. [38], i.e. systems of size $40\,\text{mm} \times 127\,\text{mm}$, with a spatial mesh size $\delta = 1\,\text{mm}$, a time step $\tau = 1\,\text{ps}$, $t_\text{p} = 7\,\text{ps}$, $t_\text{d} = 350\,\text{ps}$ and the speed of light in the medium $v = 0.222\,\text{mm/ps}$ [135]. We verified (by reducing the mesh size and time step) that the numerical results are, for all practical purposes, exact. The simulation itself is carried out in a manner identical to the procedure used in the time-gating technique [38].

The sample is illuminated uniformly by the pulsed light source. This corresponds to the experimental situation in which the phantom is located on an x–y stage and is moved in the horizontal plane under computer control. The detector accumulates the light intensity over the interval $t_\text{d} < t < t + \Delta t$ where Δt denotes the time gate. In Fig. 1 we depict our simulation results (dashed curves) and the experimental data (solid curves) which are taken from Fig. 12a of Ref. [38]. The experimental light intensities are normalized to the continuous-wave case. For each of Figs. 1–5 we have multiplied the simulation data of each figure by a factor, determined visually, so

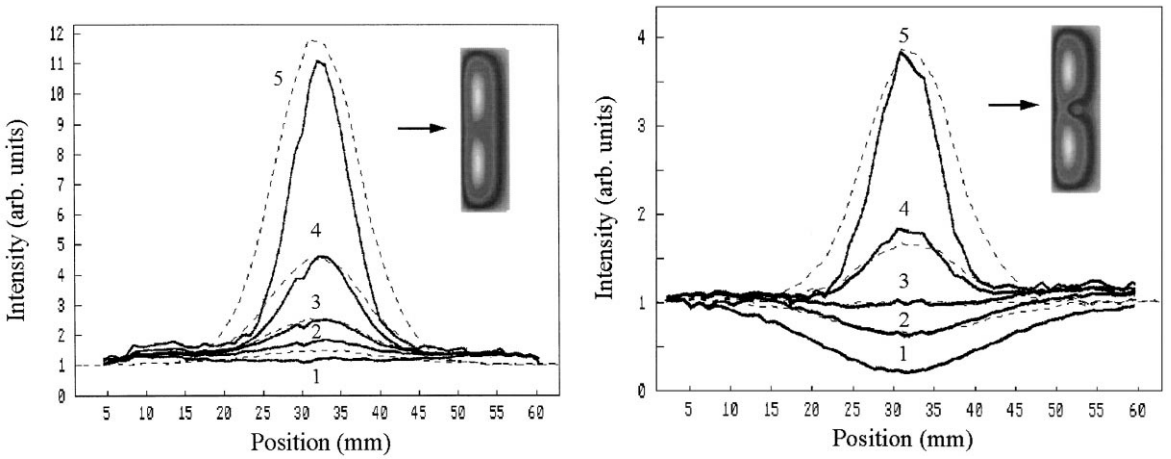

Fig. 1. Comparison of experimental [38] (solid curves) and computer simulation (dashed curves) results for the time-resolved transilluminated diffusive light intensity. In experiment and simulation the turbid medium has a reduced scattering factor $\mu_s' = 0.9\,\mathrm{mm}^{-1}$ and an absorption factor $\mu_a < 0.001\,\mathrm{mm}^{-1}$; the absorption factor of the 8 mm diameter tube is $\mu_a = 0.014\,\mathrm{mm}^{-1}$ [38]. The reduced scattering factor inside the object is $\mu_s' = 0$. The tube is located in the center of the sample. As in Ref. [38] we only show the centerpart of the detected light intensity. The experimental intensities are normalized to the continuous-wave case. We have multiplied the simulation data by a factor, determined visually, so that the scale of the experimental and the simulation data is roughly the same. No attempt to make a best fit was made. As in Fig. 12a of Ref. [38]: 1, continuous-wave case (experimental data only); 2, $\Delta t = 960$ ps; 3, $\Delta t = 480$ ps; 4, $\Delta t = 240$ ps; 5, $\Delta t = 30$ ps. The inset shows the light distribution inside the sample for $\Delta t = 960$ ps; the arrow indicates the direction of the incident light. See also Fig. 12a of Ref. [38].

Fig. 2. Same as Fig. 1 except that the absorption factor of the 8 mm diameter tube is $\mu_a = 0.13\,\mathrm{mm}^{-1}$ [38]. See also Fig. 12b of Ref. [38].

that the scale of the experimental and the simulation data is roughly the same. No attempt to make a best fit was made. The medium contains a plastic tube (8 mm diameter) filled with diluted ink, positioned in the centre of the sample. As in Ref. [38] we only show the centerpart of the detected light intensity. In the simulation both the absorption and the reduced scattering factors are allowed to fluctuate randomly within 10% of their values specified in Ref. [38]. Our numerical results are in remarkably good agreement with the experimental data. The inset shows the distribution of light inside the sample at $\Delta t = 960$ ps. The object is clearly visible.

Increasing the absorption factor of the diluted ink by a factor of 9 (Fig. 12b of Ref. [38]) yields the results shown in Fig. 2. Again the overall agreement with the experimental [38] data is excellent. Simulation and experimental [38] data for a medium containing bead pairs are shown in Fig. 3. The agreement between experiment and theory is remarkable. As in the previous case no attempt has been made to make a best fit. Fig. 4 displays the results for a system containing a plastic tube filled with ink-tinted milk with the same reduced scattering factor as the medium but with a different absorption factor. Clearly, the simulation data display all the features observed in experiment. In particular, the full-width at half-maximum (FWHM) agrees well with the experimental value.

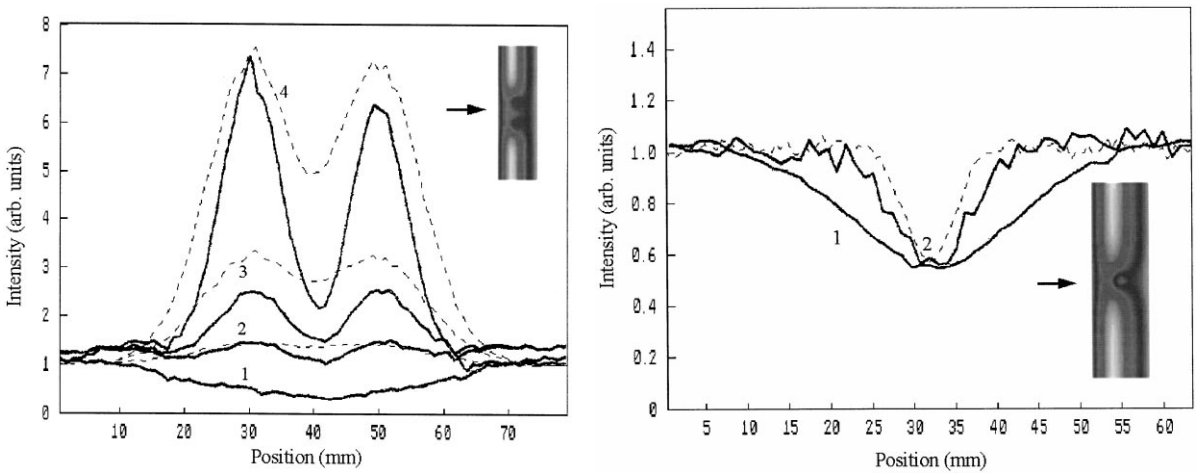

Fig. 3. Same as Fig. 1 except that instead of one there are two 10 mm diameter objects, separated by 20 mm, with an absorption factor $\mu_a = 0.029\,\mathrm{mm}^{-1}$ [38]. See also Fig. 13a of Ref. [38].

Fig. 4. Same as Fig. 1 except that the turbid medium has a reduced scattering factor $\mu_s' = 0.8\,\mathrm{mm}^{-1}$ and that the absorption and reduced scattering factors of the 8 mm diameter tube are $\mu_a = 0.1\,\mathrm{mm}^{-1}$ and $\mu_s' = 0.8\,\mathrm{mm}^{-1}$, respectively [38]. See also Fig. 15 of Ref. [38]: 1, continuous-wave (experimental data only); 2, $\Delta t = 30$ ps.

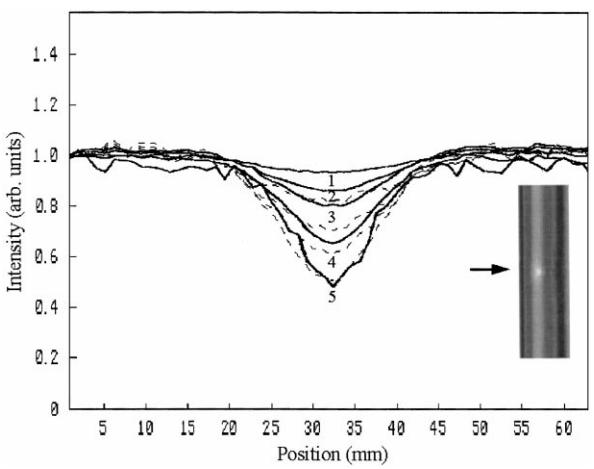

Fig. 5. Same as Fig. 1 except that the turbid medium has a reduced scattering factor $\mu_s' = 0.8\,\mathrm{mm}^{-1}$ and an absorption factor $\mu_a = 0.0005\,\mathrm{mm}^{-1}$ and that the absorption and the reduced scattering factors of the 8 mm diameter tube are $\mu_a = 0.0005\,\mathrm{mm}^{-1}$ and $\mu_s' = 2.6\,\mathrm{mm}^{-1}$, respectively [38]. See also Fig. 14 of Ref. [38].

Our simulation results indicate that the time-resolved transilluminated intensity is highly sensitive to the choice of absorption and reduced scattering factors. This is illustrated in Fig. 5 where we show the experimental [38] and simulation results for the same sample as the one used for Fig. 4 except that instead of a difference in the absorption factor of the medium and the object,

only the reduced scattering factors differ. Clearly, qualitatively similar signals can be obtained for different choices of absorption-reduced scattering factors of the object. Therefore, to determine the properties of an object the effect of the scattering and the absorption factors have to be taken into account simultaneously, in agreement with experiment [38]. The above simulation results and others (not shown) demonstrate that our simulation software reproduces all the features observed in the experiments on the tissue-like phantoms reported in Ref. [38].

4. Direct imaging

Our simulation software reproduces, without fitting, the data obtained from time-resolved transillumination measurements on turbid media containing relatively large ($\pm$ 8 mm diameter) objects. Hence, it can be used to determine the conditions under which it is possible to detect a hidden object by direct (i.e. without further processing of the measured intensities) imaging. For instance, it is of interest to know the effect of changing the size of the sample and/or the object(s).

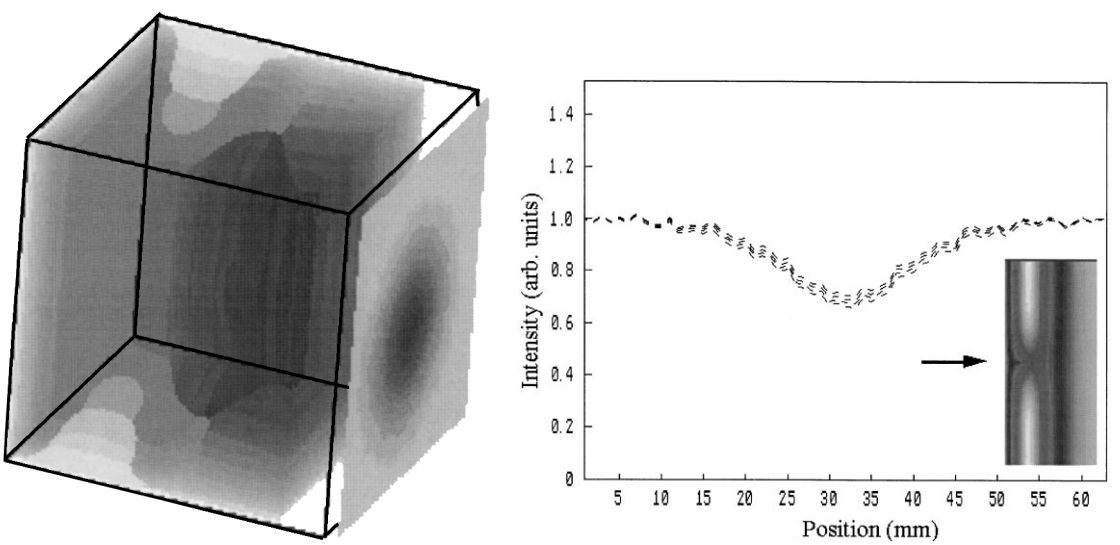

Fig. 6. Simulation of a time-resolved transillumination experiment on a turbid medium with a reduced scattering factor $\mu_s' = 1.1\,\mathrm{mm}^{-1}$ and an absorption factor $\mu_a < 0.001\,\mathrm{mm}^{-1}$ containing a 4 mm radius object with absorption and reduced scattering factors $\mu_a = 0.11\,\mathrm{mm}^{-1}$ and $\mu_s' = 1.1\,\mathrm{mm}^{-1}$, respectively. The dimensions of the sample are $63\,\mathrm{mm} \times 63\,\mathrm{mm} \times 63\,\mathrm{mm}$. The object is located in the middle of the sample. The transmitted intensity for $\Delta t = 1.7$ ns is projected onto the rightmost plane of the sample.

Fig. 7. Simulation of a time-resolved reflection experiment on a turbid medium with a reduced scattering factor $\mu_s' = 1.1\,\mathrm{mm}^{-1}$ and an absorption factor $\mu_a = 0.011\,\mathrm{mm}^{-1}$ containing a 1 mm-radius object with absorption and reduced scattering factors $\mu_a = 0.11\,\mathrm{mm}^{-1}$ and $\mu_s' = 1.1\,\mathrm{mm}^{-1}$, respectively. The dimensions of the sample are $63\,\mathrm{mm} \times 127\,\mathrm{mm}$. The object is located at (10, 64) mm. Curves bottom to top: $\Delta t = 30$ ps, $\Delta t = 240$ ps, $\Delta t = 480$ ps, $\Delta t = 960$ ps. The inset shows the light distribution inside the sample for $\Delta t = 960$ ps; the arrow indicates the direction of the incident light. Random noise ($\pm$ 10%) has been added to the absorption and scattering factor of the medium.

In Fig. 6 we show a result of a simulation for a sample of size $63\,\text{mm} \times 63\,\text{mm} \times 63\,\text{mm}$, containing a sphere of 4 mm radius, positioned right at the middle of the sample. Although not as sharp as in the case of a 40 mm thick sample, the time-resolved transmitted intensity, projected onto the right most plane of the sample, contains a clear image of the object.

In some source–detector arrangements transillumination of breasts would require compressing the breast tissue. This in turn makes the interpretation of the images more difficult as compression may have an effect on the scattering and absorption factors. Therefore, it may be advantageous to measure the reflected instead of the transmitted light, raising the interesting question to which extent a small object can be detected by performing a time-resolved reflection experiment. In Fig. 7 we show the result of a simulation that gives an indication of the limits of this technique. A 1 mm-radius object is placed 10 mm away from the plane where the light pulse enters the sample. The sample is 63 mm thick and 127 mm wide. In the turbid medium $\mu_s' = 1.1\,\text{mm}^{-1}$ and $\mu_a = 0.011\,\text{mm}^{-1}$. The object has $\mu_s' = 1.1\,\text{mm}^{-1}$ and $\mu_a = 0.11\,\text{mm}^{-1}$. From our simulations (see below) it follows that the blurring of the signal due to the random fluctuations can be reduced by increasing the time t_d at which the detectors start to record the reflected photons. The results shown in Fig. 7 were obtained for $t_d = 1000\,\text{ps}$; other parameters such as the time gate Δt are identical to those in Figs. 1–5. As in Figs. 1–5 we only show the centerpart of the detected light intensity. We conclude that although the object is small (it has a 1 mm radius), it leaves a clear trace in the time-resolved reflected intensity. There seems to be no direct relation between the FWHM and the size of the object. The fingerprint of this small object in the reflected signal disappears if the object is more than 15 mm away from the entrance plane. In this case, where the object is located rather near to the entrance plane of the light, the time-gating method does not give a significant advantage in detecting the object. For both the transillumination and reflection method, using point sources instead of uniform illumination is much less favorable for the direct imaging of the objects hidden in the medium (see below).

5. Determination of tissue optical properties

The non-invasive determination of the optical absorption and scattering properties of tissues is of great importance in both therapeutic and diagnostic applications of light in medicine, such as for example in photodynamic therapy [136], in laser surgery [137] and in monitoring changes in blood oxygenation and tissue metabolism [52]. Methods for measuring the optical properties of tissues include the pulsed photothermal radiometry method [138–140], the acoustical method [141], the time-resolved reflectance method [126], the frequency-domain reflectance method [89] and the spatially resolved steady-state diffuse reflectance method [142–145]. For a review see [146,147].

Time-resolved transillumination and reflection experiments have the possibility of measuring the optical properties of biological tissue in vivo, noninvasively. Noninvasive measurements imply that the optical properties of tissue must be deduced from measurements of the light emerging from the tissue. This requires a theoretical model to describe the photon propagation through the tissue and/or to provide an analytical expression of the transmittance and/or reflectance curve, depending on the optical parameters. Fitting the theoretical curve to the experimental data gives an estimate of the optical parameters of the tissue. The accuracy of the results achieved with

time-resolved transmittance and/or reflectance techniques depends on how appropriate the model is for the description of the particular problem under study. Different ranges of optical parameters and experimental conditions may require different theoretical approaches [148].

Interpretation of the experimental data is generally based on the radiative transport theory [99]. Various models and approximations of the radiative transport equation are used to relate the measured light intensities to the optical parameters of the sample. Apart from the Kubelka–Munk theory [149] and the diffusion theory [99,150,151], there are the inverse adding-doubling method [152], which takes into account anisotropic scattering, and the Monte Carlo approach [114,121,122,153,154] to model light propagation in tissue. Closed-form expressions for the time-resolved reflectance and transmittance curves have been obtained by using a discrete lattice random walk model [124,155] and diffusion theory [126,156,157].

The object of this section is to explore in detail how the measured intensity profiles obtained from time-resolved transillumination and reflectance experiments can be related to the optical coefficients of the tissue under investigation. The reflectance and transmittance curves are obtained by simulating time-resolved experiments on tissue phantoms of known absorption and reduced scattering factors and by performing time-resolved experiments on various solutions of intralipid.

5.1. Experimental setup

The experimental setup for time-resolved reflectance imaging is depicted in Fig. 8. The setup for time-resolved transillumination imaging is very similar. The laser system consists of a mode-locked Tsunami Ti : Sapphire laser (power: 1 W, wavelength: 800 nm, repetition frequency: 82 MHz and

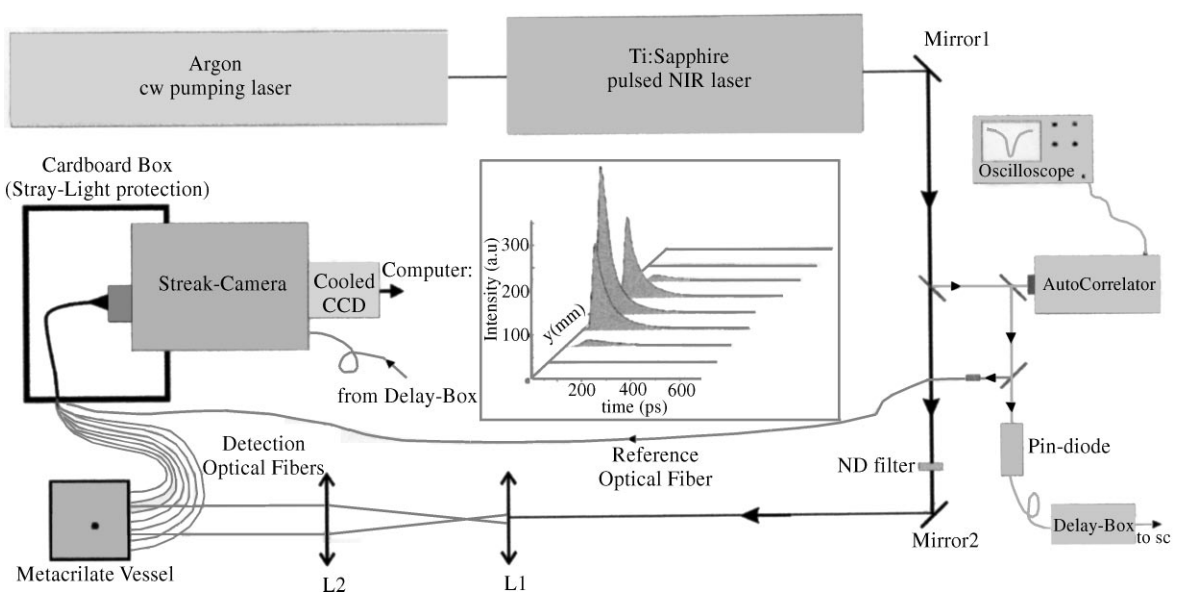

Fig. 8. Setup for the time-resolved reflectance experiment. Inset: Scetch of time-resolved reflectance curves as obtained from the various detection fibers.

pulse width: 0.06 ps) which is pumped with a BeamLok Ar ion-laser. The pulsed beam is splitted in two beams: a probe beam to illuminate the tissue phantom and a beam which on its turn is splitted in three beams, namely a beam for triggering a 2 ps resolution synchroscan streak camera (Hamamatsu C5680), a reference beam for setting an absolute time scale and a beam to visualize the pulse shape through an autocorrelator. The probe beam is attenuated by a factor of 10^3 with a neutral density filter, expanded and collimated to a diameter of 2 mm using two lenses (L_1 and L_2) in Keplerian configuration in combination with a small pinhole and is finally directed to the phantom. The phantom consists of a methacrylate vessel filled with various solutions of commercial intralipid-10%. For the time-resolved reflectance experiments the vessel has dimensions 70 mm × 70 mm × 70 mm. In the case of the time-resolved transillumination experiments the vessel has dimensions 30 mm × 70 mm × 70 mm or 10 mm × 70 mm × 70 mm. In all cases the vessel is filled with intralipid to a height of 55 mm.

Light from the probe beam is scattered many times in the phantom before it reaches the detection side of the phantom. The detection side of the vessel is the front (back) surface of the vessel for reflection (transillumination) experiments. An array of nine optical fibers (96 μm core diameter and 0.29 numerical aperture) is glued into the detection side (to avoid direct reflections from the methacrylate) at a height of $z = 25$ mm as shown in Fig. 8. The distance between the fibers in the y-direction is 5 mm (light propagates in the x-direction). The free end of the fibers, together with the reference beam, are set right in the input slit of the streak camera (SC). The slit dimension is adjusted to 125 μm × 6 mm (the photocathode of the streaktube has dimensions 100 μm × 8 mm) and coincides with the focal plane of the input optics of the SC. The detected light is temporally resolved in a single streak image. The SC working in synchroscan mode allows the integration of the signal over a large number of consecutive pulses. The intensity profiles (see Fig. 8) for each position (i.e. each fiber) are easily obtained from the individual streak image "traces".

Background subtraction is applied to the images to reduce camera dark-current noise. The effect of the non-uniform response of each channel in the SC, and the possible difference in sensitivity between the fibers is corrected for by dividing the streak-image by a shading image obtained by illumination through the fibers with uniform and constant light. The position of the beam, the sample and the detectors are kept fixed during the measurements.

5.2. Estimation of the reduced scattering and absorption factor

In the light diffusion model the turbid medium is characterized by its reduced scattering and absorption factor. The question then arises whether these factors can be determined from time-resolved measurements. Pioneering work in this direction has shown that under certain conditions the answer to this question is affirmative [126].

Assuming that at $t = 0$ the light intensity in the medium $|I(0)\rangle = 0$, the distribution of light at $t = t_p$, i.e. the time at which the source is turned off, is given by

$$|I(t_p)\rangle = \int_0^{t_p} dt\, e^{-tH}|S\rangle \approx t_p e^{-t_p H/2}|S\rangle\,, \tag{14}$$

where we have assumed that the intensity of the source is constant (i.e. $S_0(t) = S_0$) during the pulse time t_p and that t_p is small enough such that to a good approximation the integral in Eq. (14) can be

evaluated by using the trapezium rule. From formal solution (3) it then follows that for $t \geq t_p$ the light intensity is given by

$$|I(t)\rangle \approx t_p e^{-(t-t_p/2)H}|S\rangle, \quad t \geq t_p \,. \tag{15}$$

The next step is to assume that the medium is uniform, i.e. it can be described by a constant diffusion coefficient $\hat{D}_0 = v/3(\hat{\mu}_s' + \hat{\mu}_a)$ and a constant absorption factor $\hat{V}_0 = v\hat{\mu}_a$. Expression (15) then simplifies to

$$|I(t)\rangle \approx t_p e^{-(t-t_p/2)\hat{V}_0} e^{(t-t_p/2)\hat{D}_0\nabla^2}|S\rangle, \quad t \geq t_p \,. \tag{16}$$

Further evaluation of $e^{(t-t_p/2)\hat{D}_0\nabla^2}|S\rangle$ requires a choice of the boundary conditions on $|I(t)\rangle$. The desire to obtain for Eq. (16) an analytical expression suitable for fitting purposes severely limits this choice: No boundaries (free-space), a semi-infinite medium with Dirichlet boundary conditions per direction (e.g. $I((0,y,z),t) = 0$), Dirichlet boundary conditions on both sides (e.g. $I((0,y,z),t) = I((L_x,y,z),t) = 0$), and any combination of any of these. We have systematically tested the various possibilities and found that adopting Dirichlet boundary conditions consistently gave superior fits, in concert with the results of Ref. [126]. In view of this we will in this paper not present results for boundary conditions other than the latter.

In the case of Dirichlet boundary conditions (16) reads

$$I(\boldsymbol{r},t) \approx t_p e^{-(t-t_p/2)\hat{V}_0} \int d\boldsymbol{r}'\, K(x,x',(t-t_p/2)\hat{D}_0,L_x) K(y,y',(t-t_p/2)\hat{D}_0,L_y)$$
$$\times K(z,z',(t-t_p/2)\hat{D}_0,L_z) S(\boldsymbol{r}'), \quad t \geq t_p \,, \tag{17}$$

where

$$K(u,u',\tau,L) = (4\pi\tau)^{-1/2} \sum_{m=-\infty}^{+\infty} (e^{-(u-u'+2mL)^2/4\tau} - e^{-(u+u'+2mL)^2/4\tau}) \,, \tag{18}$$

is the propagator for one-dimensional diffusion on a line segment of length L. In practice, $\sum_{m=-\infty}^{+\infty}$ can be replaced by $\sum_{m=-m_0}^{+m_0}$ where m_0 is the integer nearest to $1 + (-\tau \ln \varepsilon)^{1/2}/L$, ε denoting the machine precision.

Following Ref. [126] we assume that the source is positioned not at the boundary but inside the medium, at a distance $x_0 = 1/\mu_s'$ from the boundary. In the case of a point source the remaining integral in Eq. (17) becomes trivial and Eq. (17) reduces to

$$I(\boldsymbol{r},t) \approx S_0 t_p e^{-(t-t_p/2)\hat{V}_0} K(x,x_0,(t-t_p/2)\hat{D}_0,L_x)$$
$$\times K(y,0,(t-t_p/2)\hat{D}_0,L_y) K(z,0,(t-t_p/2)\hat{D}_0,L_z), \quad t \geq t_p \,, \tag{19}$$

where we have chosen for the light pulse to be incident along the x-axis. Clearly, Eq. (19) is sufficiently simple for fitting purposes. For particular choices of m_0, Eq. (19) leads to the formulae given in Ref. [126]. Improvement of the theoretical description of time-resolved optical experiments, especially at early times, may be achieved by matching the temporal position of the theoretical expression (19) and the experimental data by means of an extra parameter, the time-shift

t_s, introduced in Eq. (19) [148]. This yields

$$I(\boldsymbol{r},t) \approx S_0 t_p \, e^{-(t+t_s-t_p/2)\hat{V}_0} K(x,x_0,(t+t_s-t_p/2)\hat{D}_0,L_x) K(y,0,(t+t_s-t_p/2)\hat{D}_0,L_y) \times K(z,0,(t+t_s-t_p/2)\hat{D}_0,L_z), \quad t \geq t_p \,, \tag{20}$$

where t_s, $\hat{D}_0$ and $\hat{V}_0$ are fitting parameters.

5.3. Transillumination

We are now in the position to assess the reliability of the procedure of extracting $\hat{D}_0$ and $\hat{V}_0$ (and therefore also $\hat{\mu}_s'$ and $\hat{\mu}_a$) from experimental or simulation data. Table 1 contains the values of μ_s' and μ_a used as input for the simulation with those ($\hat{\mu}_s'$ and $\hat{\mu}_a$, respectively) obtained by fitting Eq. (20) to the simulation data of the transmitted intensity. Because we are dealing with simulation data we know that $t_s = 0$. From Table 1 it is clear that in all cases the fitting procedure works very well, independent of the source type and detector position.

Table 1
Comparison between the reduced scattering (μ_s') and the absorption (μ_a) factor and the corresponding estimates $\hat{\mu}_s'$ and $\hat{\mu}_a$ obtained by fitting the simulated transmitted intensity to expression (20) with $t_s = 0$. The dimensions of the sample are 71 mm × 71 mm. The light velocity $v = 0.22$ mm/ps. $U(d,t_p)$: Uniform illumination by a beam of diameter d (in mm), centered around (0, 36 mm), during a time t_p (in ps). $G(d,t_p)$: Gaussian light beam of width d, centered around (0, 36 mm), during a time t_p (in ps). R denotes the distance between the source and the detector

μ_a (mm^{-1})	μ_s' (mm^{-1})	Source	R (mm)	$\hat{\mu}_a$ (mm^{-1})	$\hat{\mu}_s'$ (mm^{-1})
0.030	0.50	U(1,100)	71.0	0.030	0.49
0.030	0.50	U(1,100)	71.7	0.030	0.49
0.030	0.50	U(1,100)	72.6	0.030	0.49
0.030	0.50	U(1,100)	73.8	0.029	0.48
0.030	0.50	G(2,100)	71.0	0.030	0.49
0.030	0.50	G(2,100)	71.7	0.030	0.49
0.030	0.50	G(2,100)	72.6	0.030	0.49
0.030	0.50	G(2,100)	73.8	0.029	0.48
0.040	0.11	U(1,6)	71.0	0.039	0.12
0.040	0.11	U(1,6)	71.7	0.038	0.12
0.040	0.11	U(1,6)	72.6	0.038	0.12
0.040	0.11	U(1,6)	73.8	0.038	0.13
0.040	0.20	G(5,6)	71.0	0.040	0.20
0.040	0.20	G(5,6)	71.7	0.040	0.20
0.040	0.20	G(5,6)	72.6	0.039	0.20
0.040	0.20	G(5,6)	73.8	0.038	0.20
0.040	0.30	G(5,6)	71.0	0.040	0.29
0.040	0.30	G(5,6)	71.7	0.040	0.29
0.040	0.30	G(5,6)	72.6	0.039	0.29
0.040	0.30	G(5,6)	73.8	0.039	0.29
0.040	0.30	G(5,100)	71.0	0.040	0.30
0.040	0.30	G(5,100)	71.7	0.040	0.30
0.040	0.30	G(5,100)	72.6	0.040	0.30
0.040	0.30	G(5,100)	73.8	0.039	0.30

In Tables 2 and 3 we show the results of fitting the simulation data for a particular set of model parameters used in the experiments of Ref. [38]. Also in this case there is good agreement between the values used as input to the simulations and the values obtained by fitting to Eq. (20), except for the case of uniform illumination over one whole side of the sample. This might have been expected because Eq. (20) has been obtained by assuming a point source.

A representative example of a fit is depicted in Fig. 9. The two sets of curves correspond to the first and fourth entry of Table 3. It is clear that there is excellent agreement.

Tables 4 and 5 show the results of fitting experimental data of the transmitted intensity for various intralipid solutions of 30 and 10 mm thick, respectively. The intralipid concentrations are measured with respect to pure intralipid and not to the commercially available intralipid-10% product, which is a 10% solution of pure intralipid. Our 1% solution corresponds to the commercial product when diluted 10 times. The values for $\hat{\mu}_a$ and $\hat{\mu}'_s$, measured at a wavelength of $\lambda = 800\,\text{nm}$, lie well within the range of values previously found in other studies: $\mu'_s = 0.935\,\text{mm}^{-1} \times \text{conc}$ and $\mu_a = 0.95 \times 10^{-3}\,\text{mm}^{-1} \times \text{conc}$ at $\lambda = 630\,\text{nm}$; [158] $\mu'_s = 1.119\,\text{mm}^{-1} \times \text{conc}$ and $\mu_a = 0.57 \times 10^{-2}\,\text{mm}^{-1} \times \text{conc}$ at $\lambda = 633\,\text{nm}$; [159] $\mu'_s = 1.104\,\text{mm}^{-1} \times \text{conc}$ and $\mu_a = 0.15 \times 10^{-2}\,\text{mm}^{-1} \times \text{conc}$ at $\lambda = 632.8\,\text{nm}$; [160] $\mu'_s = 0.681\,\text{mm}^{-1} \times \text{conc}$ and $\mu_a = 0.48 \times 10^{-1}\,\text{mm}^{-1} \times \text{conc}$ at $\lambda = 1064\,\text{nm}$; [160] $\mu'_s = 1.44\,\text{mm}^{-1} \times \text{conc}$ and $\mu_a = 0.027 \times 10^{-2}\,\text{mm}^{-1} \times \text{conc}$ at $\lambda = 632.8\,\text{nm}$; [161] $\mu'_s = 1.224\,\text{mm}^{-1} \times \text{conc}$ and $\mu_a = 0.12\,\text{mm}^{-1} \times \text{conc}$ at $\lambda = 633\,\text{nm}$;

Table 2
Comparison between the scattering (μ'_s) and the absorption (μ_a) factor and the corresponding estimates $\hat{\mu}'_s$ and $\hat{\mu}_a$ obtained by fitting the simulated transmitted intensity to expression (20) with $t_s = 0$. The dimensions of the sample are $L_x = 40\,\text{mm}$ and $L_y = 127\,\text{mm}$. The light velocity $v = 0.22\,\text{mm/ps}$. $U(d, t_p)$: Uniform illumination by a beam of diameter d (in mm), centered around $(0, 63)\,\text{mm}$, during a time t_p (in ps). R denotes the distance between the source and the detector

μ_a (mm^{-1})	μ'_s (mm^{-1})	Source	R (mm)	$\hat{\mu}_a$ (mm^{-1})	$\hat{\mu}'_s$ (mm^{-1})
0.010	0.90	U(1,10)	40.0	0.010	0.86
0.010	0.90	U(1,10)	41.2	0.010	0.86
0.010	0.90	U(1,10)	42.7	0.010	0.86
0.010	0.90	U(1,10)	44.7	0.010	0.86
0.010	0.90	U(1000,10)	40.0	0.010	0.94
0.010	0.90	U(1000,10)	41.2	0.010	0.90
0.010	0.90	U(1000,10)	42.7	0.010	0.84
0.010	0.90	U(1000,10)	44.7	0.010	0.77

Table 3
Same as Table 2, except that the dimensions of the sample are $L_x = 40\,\text{mm}$, $L_y = L_z = 63\,\text{mm}$. The centre of the illuminating beam is at $(0, 31, 31)\,\text{mm}$

μ_a (mm^{-1})	μ'_s (mm^{-1})	Source	R (mm)	$\hat{\mu}_a$ (mm^{-1})	$\hat{\mu}'_s$ (mm^{-1})
0.010	0.90	U(1,10)	40.0	0.010	0.86
0.010	0.90	U(1,10)	41.2	0.010	0.86
0.010	0.90	U(1,10)	42.7	0.010	0.87
0.010	0.90	U(1,10)	44.7	0.010	0.89

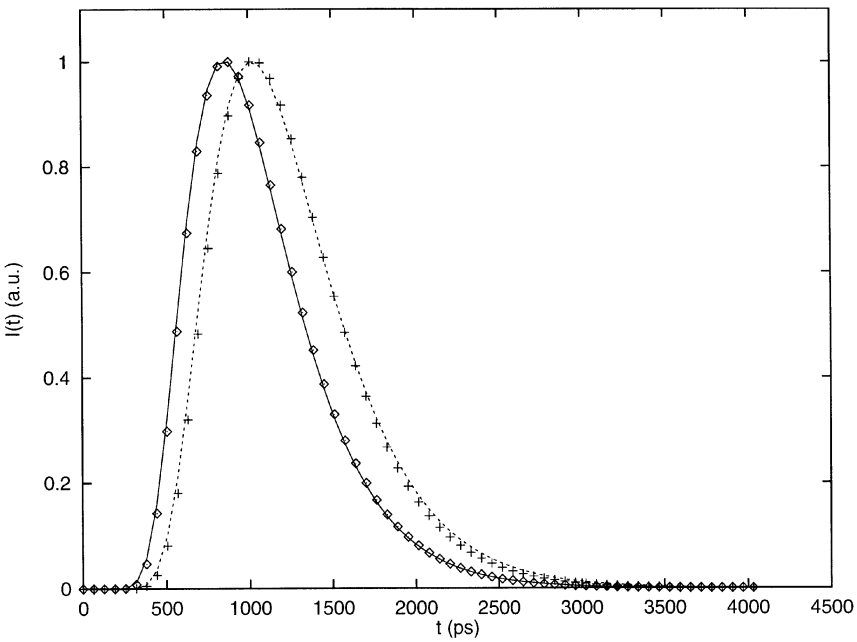

Fig. 9. Fit of transillumination intensity data to expression (20) with $t_s = 0$. The dimensions of the sample are $40\,\text{mm} \times 63\,\text{mm} \times 63\,\text{mm}$. Solid curve: Simulation data for $R = 40\,\text{mm}$, $\mu_s' = 0.9\,\text{mm}^{-1}$, and $\mu_a = 0.01\,\text{mm}^{-1}$. Diamonds: Data obtained from Eq. (20) using $R = 40\,\text{mm}$, $\hat{\mu}_s' = 0.86\,\text{mm}^{-1}$ and $\hat{\mu}_a = 0.01\,\text{mm}^{-1}$. Dashed curve: Simulation data for $R = 44.7\,\text{mm}$, $\mu_s' = 0.9\,\text{mm}^{-1}$, and $\mu_a = 0.01\,\text{mm}^{-1}$. Crosses: Data obtained from Eq. (20) using $R = 44.7\,\text{mm}$, $\hat{\mu}_s' = 0.89\,\text{mm}^{-1}$ and $\hat{\mu}_a = 0.01\,\text{mm}^{-1}$. All curves are normalized to their maximum.

Table 4
Estimates for the reduced scattering ($\hat{\mu}_s'$), the absorption ($\hat{\mu}_a$) factor and the time-shift (t_s) obtained by fitting the transmitted intensity for various solutions of intralipid to expression (20). The dimensions of the sample are $L_x = 30\,\text{mm}$, $L_y = 70\,\text{mm}$ and $L_z = 55\,\text{mm}$. The light velocity $v = 0.22\,\text{mm/ps}$. The source emits a Gaussian light distribution of width 2 mm, centered around (0, 36, 25) mm during a time of 0.06 ps. R denotes the distance between the source and the detector

Concentration (%)	R (mm)	$\hat{\mu}_a$ (mm^{-1})	$\hat{\mu}_s'$ (mm^{-1})	t_s (ps)
0.5	30.0	0.0008	0.60	35
0.5	30.4	0.0008	0.60	35
0.5	31.6	0.0012	0.60	35
0.5	33.5	0.0016	0.60	30
1.0	30.0	0.0025	1.16	175
1.0	30.4	0.0025	1.16	175
1.0	31.6	0.0029	1.18	175
1.0	33.5	0.0035	1.19	175

[23] $\mu_s' = 1.128\,\text{mm}^{-1} \times \text{conc}$ and $\mu_a = 0.12\,\text{mm}^{-1} \times \text{conc}$ at $\lambda = 780\,\text{nm}$; [23] $\mu_s' = 1.4\,\text{mm}^{-1} \times$ conc and $\mu_a = 0.5\,\text{mm}^{-4} \times \text{conc}$ at $\lambda = 633\,\text{nm}$; [67] $\mu_s' = 0.888\,\text{mm}^{-1} \times \text{conc}$ at $\lambda = 632.8\,\text{nm}$ [162]. The abbreviation conc denotes the concentration of intralipid in percent.

Differences in these results may at least in part be attributed to a difference in the composition of intralipid-10% [159,160]. Moreover, the absorption factor of intralipid seems difficult to determine accurately [163].

Fig. 10 depicts a typical example of a fit of experimental transillumination curves to theoretical expression (20). The two sets of curves correspond to the second and fourth entry of Table 4.

Table 5
Same as Table 4, except that the dimensions of the sample are $L_x = 10\,\text{mm}$, $L_y = 70\,\text{mm}$ and $L_z = 55\,\text{mm}$

Concentration (%)	R (mm)	$\hat{\mu}_a$ (mm^{-1})	$\hat{\mu}'_s$ (mm^{-1})	t_s (ps)
1.0	10.0	0.0005	1.34	0
1.0	11.2	0.0005	1.34	2
1.0	14.1	0.0006	1.30	5
1.0	18.0	0.0006	1.24	8
2.0	10.0	0.0010	2.20	0
2.0	11.2	0.0015	2.20	6
2.0	14.1	0.0026	2.14	10
2.0	18.0	0.0024	1.90	20

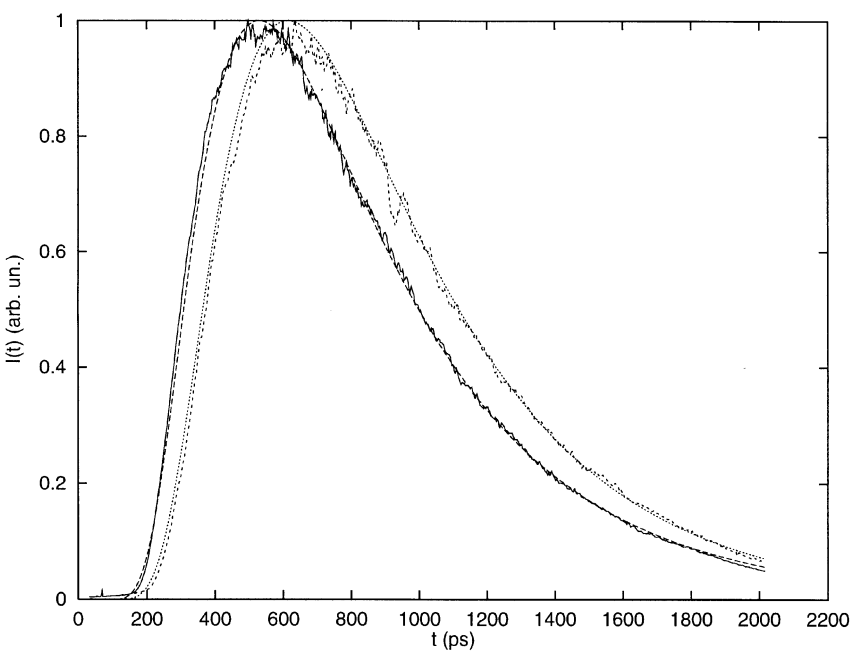

Fig. 10. Fit of transillumination intensity data to expression (20). The dimensions of the sample are $30\,\text{mm} \times 70\,\text{mm} \times 55\,\text{mm}$. Solid curve: Experimental data for a 0.5% intralipid solution and $R = 30.4\,\text{mm}$. Long-dashed curve: Data obtained from (20) using $R = 30.4\,\text{mm}$, $\hat{\mu}'_s = 0.6\,\text{mm}^{-1}$, $\hat{\mu}_a = 0.0008\,\text{mm}^{-1}$ and $t_s = 35\,\text{ps}$. Short-dashed curve: Experimental data for a 0.5% intralipid solution and $R = 33.5\,\text{mm}$. Dotted curve: Data obtained from (20) using $R = 33.5\,\text{mm}$, $\hat{\mu}'_s = 0.6\,\text{mm}^{-1}$ and $\hat{\mu}_a = 0.0016\,\text{mm}^{-1}$. All curves are normalized to their maximum.

Table 6
Comparison between the reduced scattering (μ_s') and the absorption (μ_a) factor and the corresponding estimates $\hat{\mu}_s'$ and $\hat{\mu}_a$ obtained by fitting the simulated reflected intensity to expression (20) with $t_s = 0$. The dimensions of the sample are 71 mm × 71 mm. The light velocity $v = 0.22$ mm/ps. $U(d, t_p)$: Uniform illumination by a beam of diameter d (in mm), centered around (0, 36 mm), during a time t_p (in ps). $G(d, t_p)$: Gaussian light beam of width d, centered around (0, 36 mm), during a time t_p (in ps). R denotes the distance between the source and the detector. A "x" indicates that the fitting procedure failed to produce reasonable (i.e. positive) estimates

μ_a (mm^{-1})	μ_s' (mm^{-1})	Source	R (mm)	$\hat{\mu}_a$ (mm^{-1})	$\hat{\mu}_s'$ (mm^{-1})
0.005	0.90	U(1,10)	10	0.005	0.88
0.005	0.90	U(1,10)	15	0.005	0.88
0.005	0.90	U(1,10)	20	0.005	0.88
0.005	0.90	G(5,100)	10	x	x
0.005	0.90	G(5,100)	15	x	x
0.005	0.90	G(5,100)	20	x	x
0.010	0.60	U(1,6)	10	0.010	0.59
0.010	0.60	U(1,6)	15	0.010	0.59
0.010	0.60	U(1,6)	20	0.010	0.59
0.010	0.60	U(2,6)	10	0.010	0.56
0.010	0.60	U(2,6)	15	0.010	0.57
0.010	0.60	U(2,6)	20	0.010	0.58
0.010	0.60	U(1,100)	10	x	x
0.010	0.60	U(1,100)	15	x	x
0.010	0.60	U(1,100)	20	x	x
0.010	0.60	G(0.5,6)	10	0.010	0.57
0.010	0.60	G(0.5,6)	15	0.010	0.58
0.010	0.60	G(0.5,6)	20	0.010	0.59
0.010	0.60	G(2,6)	10	0.010	0.52
0.010	0.60	G(2,6)	15	0.010	0.55
0.010	0.60	G(2,6)	20	0.010	0.57
0.010	0.60	G(5,6)	10	x	x
0.010	0.60	G(5,6)	15	x	x
0.010	0.60	G(5,6)	20	x	x
0.040	0.11	U(1,6)	10	0.040	0.11
0.040	0.11	U(1,6)	15	0.040	0.11
0.040	0.11	U(1,6)	20	0.040	0.12
0.040	0.60	U(1,6)	10	0.040	0.57
0.040	0.60	U(1,6)	15	0.040	0.57
0.040	0.60	U(1,6)	20	0.040	0.58

5.4. Reflection

We have seen that the values of μ_s' and μ_a can be estimated rather accurately from fitting Eq. (20) to the transillumination data. This unfortunately is not always the case when fitting to reflection data. In Table 6 we show a collection of fits to simulation data of the reflected intensity. The crosses in the fifth and sixth column indicate that it was impossible to let Eq. (20) resemble the simulation data. In general the fitting procedure fails if the light pulse is too long ($t_p > 10$ ps) or if the illumination area is too large ($d > 5$ mm). This could be expected on the basis of the

Table 7
Comparison between the reduced scattering (μ_s') and the absorption (μ_a) factor and the corresponding estimates $\hat{\mu}_s'$ and $\hat{\mu}_a$ obtained by fitting the simulated reflected intensity to expression (20) with $t_s = 0$. The dimensions of the sample are $L_x = 40$ mm and $L_y = 127$ mm. The light velocity $v = 0.22$ mm/ps. $U(d, t_p)$: Uniform illumination by a beam of diameter d (in mm), centered around (0, 63) mm, during a time t_p (in ps). R denotes the distance between the source and the detector. A "x" indicates that the fitting procedure failed to produce reasonable (i.e. positive) estimates

μ_a (mm^{-1})	μ_s' (mm^{-1})	Source	R (mm)	$\hat{\mu}_a$ (mm^{-1})	$\hat{\mu}_s'$ (mm^{-1})
0.010	0.90	U(1,10)	10	0.010	0.87
0.010	0.90	U(1,10)	15	0.010	0.87
0.010	0.90	U(1,10)	20	0.010	0.87
0.010	0.90	U(1000,10)	10	x	x
0.010	0.90	U(1000,10)	15	x	x
0.010	0.90	U(1000,10)	20	x	x

Table 8
Same as Table 7, except that the dimensions of the sample are $L_x = 40$ mm, $L_y = L_z = 63$ mm and the beam centre is at (0, 31, 31) mm

μ_a (mm^{-1})	μ_s' (mm^{-1})	Source	R (mm)	$\hat{\mu}_a$ (mm^{-1})	$\hat{\mu}_s'$ (mm^{-1})
0.010	0.90	U(1,10)	10	0.010	0.88
0.010	0.90	U(1,10)	15	0.010	0.88
0.010	0.90	U(1,10)	20	0.010	0.88

assumptions made in deriving Eq. (20), but it is of interest to note that, in contrast to the case of transillumination, the pulse time t_p affects the quality of the fit. In Tables 7 and 8 we show the results of fitting the simulation data for a particular set of model parameters used in the experiments of Ref. [38]. There is good agreement between the values used as input to the simulations and the values obtained by fitting to Eq. (20) again except, for uniform illumination over the whole sample. A typical example of a fit to reflection data is shown in Fig. 11. The two sets of data used correspond to the first and third entries of Table 8. It is clear that Eq. (20) fits the data very well.

Fig. 12 depicts a fit of an experimental reflection curve for a 1% intralipid solution to the curve obtained from Eq. (20). The source–detector distance (or R) is 7 mm. For higher R values the experimental data becomes rather noisy and fitting becomes more difficult. For the particular case shown in Fig. 5, $\hat{\mu}_a = 0.01\,\text{mm}^{-1}$ and $\hat{\mu}_s = 1.16\,\text{mm}^{-1}$.

In summary, in the regime where the diffusion equation can be used to model light transport through a turbid medium, the reduced scattering and absorption factor can be extracted from measured data by fitting a simple expression, derived from diffusion theory, to the data. In contrast to simulation data, for experimental data there is an additional ambiguity due to the uncertainty in defining time zero, which has to be accounted for by introducing a third fitting parameter. Evidently this has a negative impact on the reliability of the whole procedure of extracting the reduced scattering and absorption factors. Reliable estimates of both factors can be obtained from

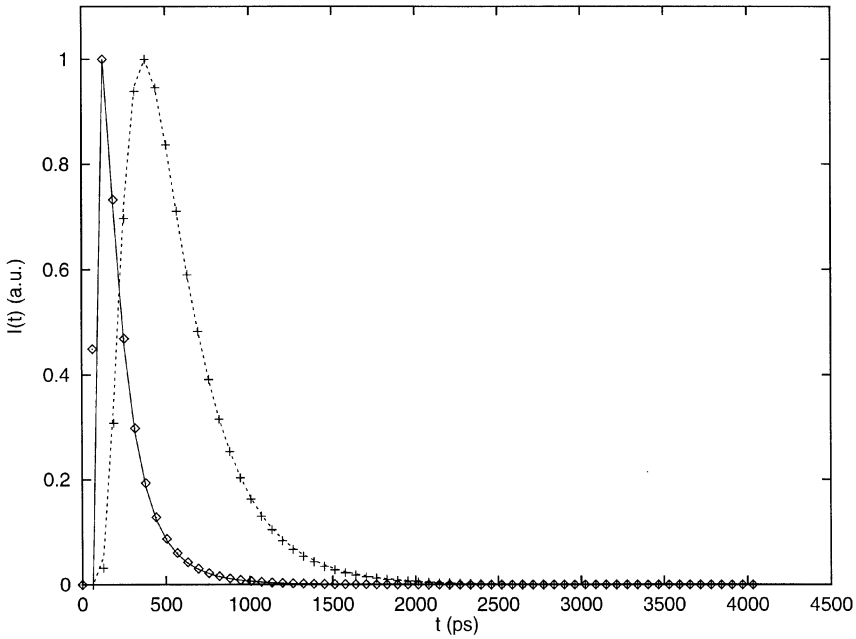

Fig. 11. Fit of reflected intensity data to expression (20) with $t_s = 0$. The dimensions of the sample are $40\,\text{mm} \times 63\,\text{mm} \times 63\,\text{mm}$. Solid curve: Simulation data for $R = 10\,\text{mm}$, $\mu_s' = 0.9\,\text{mm}^{-1}$, and $\mu_a = 0.01\,\text{mm}^{-1}$. Diamonds: Data obtained from Eq. (20) using $R = 10\,\text{mm}$, $\hat{\mu}_s' = 0.88\,\text{mm}^{-1}$ and $\hat{\mu}_a = 0.01\,\text{mm}^{-1}$. Dashed curve: Simulation data for $R = 20\,\text{mm}$, $\mu_s' = 0.9\,\text{mm}^{-1}$, and $\mu_a = 0.01\,\text{mm}^{-1}$. Crosses: Data obtained from Eq. (20) using $R = 20\,\text{mm}$, $\hat{\mu}_s' = 0.88\,\text{mm}^{-1}$ and $\hat{\mu}_a = 0.01\,\text{mm}^{-1}$. All curves are normalized to their maximum.

transillumination data, irrespective of the pulse time, the detector positions and the width of the beam (excluding illumination over a whole side of the sample). In general, the estimates obtained from reflection measurements are less reliable.

6. Data processing method: Theory

Usually, the quality of the images rendered by an imaging technique can be substantially enhanced by the use of appropriate data processing. An obvious approach is to compare the data with other data obtained from a reference, or model, system. In the case at hand we know that the immense scattering of light is responsible for the blurring of the images of the objects. The variations of both the reduced scattering and absorption factor due to the objects are relatively small. Therefore, as a starting point, it is reasonable to take as a reference model a system with a constant diffusion coefficient D_0 and a constant absorption factor V_0. We call this model $H_0 = -D_0\nabla^2 + V_0$. We will prove some rigorous bounds on the ratio of the intensity distributions of models H_0 and $H_1 = H_0 + V$ with $V = V(\boldsymbol{r}) - V_0$. These bounds give the maximum enhancement of the image quality one can obtain by using model H_0 and also provide a clue as to the information that is contained in this ratio. In the next section we will use the simulation

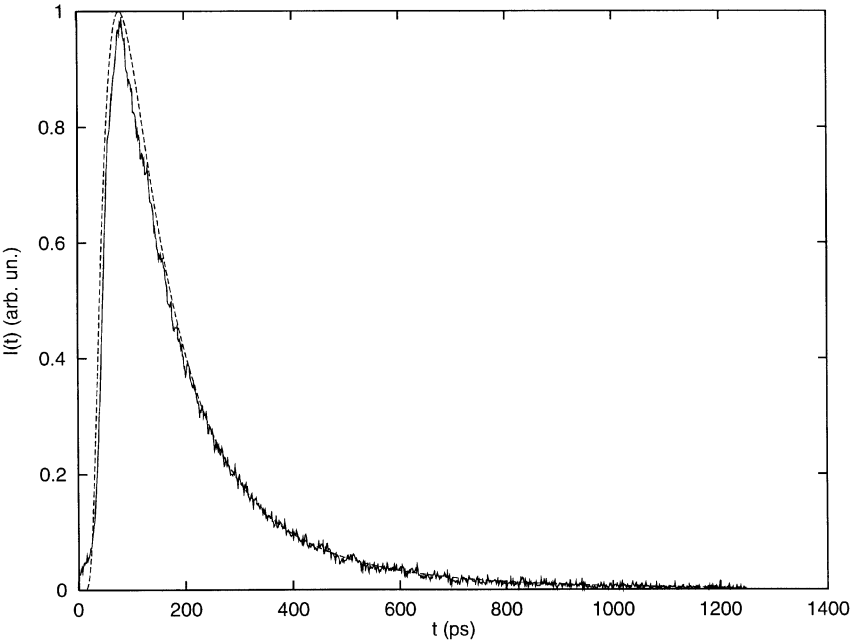

Fig. 12. Fit of reflected intensity data to expression (20). The dimensions of the sample are 70 mm × 70 mm × 55 mm. Solid curve: Experimental data for a 1% intralipid solution and $R = 7$ mm. Dashed curve: Data obtained from Eq. (20) using $R = 7$ mm, $\hat{\mu}_s' = 1.16\,\mathrm{mm}^{-1}$, $\hat{\mu}_a = 0.01\,\mathrm{mm}^{-1}$ and $t_s = -115$ ps. Both curves are normalized to their maximum.

technique to demonstrate that this image processing method can be very effective. In this section we will, for the sake of simplicity, restrict ourselves to the case where $D(\boldsymbol{r}) = D_0$. The effect of a non-uniform $D(\boldsymbol{r})$ will be studied in the next section.

A first step in proving these bounds is to generalize the exact inequalities [164]

$$\langle \boldsymbol{r}|e^{-t(H_0+V)}|\boldsymbol{r}'\rangle \geq \langle \boldsymbol{r}|e^{-tH_0}|\boldsymbol{r}'\rangle \exp\left[-t\int_0^1 dx \frac{\langle \boldsymbol{r}|e^{-txH_0}Ve^{-t(1-x)H_0}|\boldsymbol{r}'\rangle}{\langle \boldsymbol{r}|e^{-tH_0}|\boldsymbol{r}'\rangle}\right] \tag{21}$$

and

$$\langle \boldsymbol{r}|e^{-t(H_0+V)}|\boldsymbol{r}'\rangle \leq \langle \boldsymbol{r}|e^{-tH_0}|\boldsymbol{r}'\rangle \exp\left[\int_0^1 dx \ln \frac{\langle \boldsymbol{r}|e^{-txH_0}e^{-tV}e^{-t(1-x)H_0}|\boldsymbol{r}'\rangle}{\langle \boldsymbol{r}|e^{-tH_0}|\boldsymbol{r}'\rangle}\right], \tag{22}$$

and prove that $|\boldsymbol{r}'\rangle$ can be replaced by an arbitrary distribution of light intensity to be denoted by $|s\rangle$. The inequalities (21) and (22) hold if $\langle \boldsymbol{r}|e^{-tH_0}|\boldsymbol{r}'\rangle \geq 0$ for any $\boldsymbol{r}$ and $\boldsymbol{r}'$ and $V|\boldsymbol{r}\rangle = \langle \boldsymbol{r}|V|\boldsymbol{r}\rangle|\boldsymbol{r}\rangle = V(\boldsymbol{r})|\boldsymbol{r}\rangle$, conditions that are satisfied in the case of the TDDE. Making use of the fact that the light intensity is always positive, i.e. $s(\boldsymbol{r}) = \langle \boldsymbol{r}|s\rangle \geq 0$, and repeating the steps of the proof that led to Eqs. (21) and (22) we find

$$\langle \boldsymbol{r}|e^{-t(H_0+V)}|s\rangle \geq \langle \boldsymbol{r}|e^{-tH_0}|s\rangle \exp\left[-t\int_0^1 dx \frac{\langle \boldsymbol{r}|e^{-txH_0}Ve^{-t(1-x)H_0}|s\rangle}{\langle \boldsymbol{r}|e^{-tH_0}|s\rangle}\right] \tag{23}$$

and

$$\langle \boldsymbol{r}|\mathrm{e}^{-t(H_0+V)}|s\rangle \leq \langle \boldsymbol{r}|\mathrm{e}^{-tH_0}|s\rangle \exp\left[\int_0^1 \mathrm{d}x \ln \frac{\langle \boldsymbol{r}|\,\mathrm{e}^{-txH_0}\mathrm{e}^{-tV}\mathrm{e}^{-t(1-x)H_0}|s\rangle}{\langle \boldsymbol{r}|\mathrm{e}^{-tH_0}|s\rangle}\right]. \tag{24}$$

The above inequalities suggest that if we generate a reference signal $I_0(\boldsymbol{r},s,t)=\langle \boldsymbol{r}|\mathrm{e}^{-tH_0}|s\rangle$, "measure" the intensity $I_1(\boldsymbol{r},s,t)=\langle \boldsymbol{r}|\mathrm{e}^{-tH_1}|s\rangle$ and form the ratio $I_0(\boldsymbol{r},s,t)/I_1(\boldsymbol{r},s,t)$ we will obtain information on the potential V. We now proceed to set rigorous bounds on this ratio.

6.1. Instantaneous light-intensity detection

From Eqs. (23) and (24) we obtain

$$t\int_0^1 \mathrm{d}x \frac{\langle \boldsymbol{r}|\mathrm{e}^{-txH_0}V\mathrm{e}^{-t(1-x)H_0}|s\rangle}{I_0(\boldsymbol{r},s,t)} \geq \ln\frac{I_0(\boldsymbol{r},s,t)}{I_1(\boldsymbol{r},s,t)} \geq -\int_0^1 \mathrm{d}x \ln \frac{\langle \boldsymbol{r}|\mathrm{e}^{-txH_0}\mathrm{e}^{-tV}\mathrm{e}^{-t(1-x)H_0}|s\rangle}{I_0(\boldsymbol{r},s,t)}, \tag{25}$$

or using $\ln x \leq x-1$ for $x>0$ to weaken the lower bound in Eq. (25)

$$\frac{t\int_0^1 \mathrm{d}x\langle \boldsymbol{r}|\mathrm{e}^{-txH_0}V\mathrm{e}^{-t(1-x)H_0}|s\rangle}{I_0(\boldsymbol{r},s,t)} \geq \ln\frac{I_0(\boldsymbol{r},s,t)}{I_1(\boldsymbol{r},s,t)} \geq \frac{\int_0^1 \mathrm{d}x\langle \boldsymbol{r}|\mathrm{e}^{-txH_0}(1-\mathrm{e}^{-tV})\mathrm{e}^{-t(1-x)H_0}|s\rangle}{I_0(\boldsymbol{r},s,t)}, \tag{26}$$

indicating that $\ln[I_0(\boldsymbol{r},s,t)/I_1(\boldsymbol{r},s,t)]$ contains information on V. From Eq. (26) it follows that to first order in V, inequalities (23) and (24) are equalities.

6.2. Integrated light-intensity detection

In practice, measuring the instantaneous light intensity is impossible: Due to the finite precision of the instruments one measures the intensity integrated over a time interval of finite length. In this section, we generalize the above inequalities to the case of time-integrated light-intensity detection. We will denote the time-integrated intensities by

$$\bar{I}_1(\boldsymbol{r},s,t_0,t_1)=\int_{t_0}^{t_1}\mathrm{d}t\, I_1(\boldsymbol{r},s,t) \tag{27a}$$

and

$$\bar{I}_0(\boldsymbol{r},s,t_0,t_1)=\int_{t_0}^{t_1}\mathrm{d}t\, I_0(\boldsymbol{r},s,t), \tag{27b}$$

respectively. To obtain the time-integrated version of the bounds (26) we proceed as follows. Integration of Eq. (23) with respect to t yields

$$\frac{\bar{I}_1(\boldsymbol{r},s,t_0,t_1)}{I_0(\boldsymbol{r},s,t_0,t_1)} \geq \frac{\int_{t_0}^{t_1}\mathrm{d}t\, I_0(\boldsymbol{r},s,t)\exp[-t\int_0^1 \mathrm{d}x\langle \boldsymbol{r}|\mathrm{e}^{-txH_0}V\mathrm{e}^{-t(1-x)H_0}|s\rangle/I_0(\boldsymbol{r},s,t)]}{\int_{t_0}^{t_1}\mathrm{d}t\, I_0(\boldsymbol{r},s,t)}. \tag{28}$$

Application of Jensen's inequality [165] $\int_X \mathrm{d}x\, g(x)|f(x)| \geq \exp[\int_X \mathrm{d}x\, g(x)\ln|f(x)|]$ with $\int_X \mathrm{d}x\, g(x) = 1$ to the r.h.s. of Eq. (28) yields

$$\frac{\int_0^1 \mathrm{d}x \int_{t_0}^{t_1} \mathrm{d}t\, t\langle \boldsymbol{r}|\mathrm{e}^{-txH_0} V \mathrm{e}^{-t(1-x)H_0}|s\rangle}{\int_{t_0}^{t_1} \mathrm{d}t\, I_0(\boldsymbol{r},s,t)} \geq \ln \frac{\bar{I}_0(\boldsymbol{r},s,t_0,t_1)}{\bar{I}_1(\boldsymbol{r},s,t_0,t_1)}\,. \tag{29}$$

Introducing the symbol

$$K(x,t) = \frac{\langle \boldsymbol{r}|\mathrm{e}^{-txH_0}\mathrm{e}^{-tV}\mathrm{e}^{-t(1-x)H_0}|s\rangle}{\langle \boldsymbol{r}|\mathrm{e}^{-tH_0}|s\rangle} \tag{30}$$

and integrating Eq. (24) from t_0 to t_1 yields

$$\frac{\bar{I}_1(\boldsymbol{r},s,t_0,t_1)}{\bar{I}_0(\boldsymbol{r},s,t_0,t_1)} \leq \frac{\int_{t_0}^{t_1} \mathrm{d}t\, I_0(\boldsymbol{r},s,t) \exp[\int_0^1 \mathrm{d}x \ln K(x,t)]}{\int_{t_0}^{t_1} \mathrm{d}t\, I_0(\boldsymbol{r},s,t)}\,. \tag{31}$$

The upper bound in (31) can be brought in a more convenient, albeit weaker, form by invoking a generalization of Hölders inequality [165]

$$\int_Y \mathrm{d}y\, h(y) \exp\left[\int_X \mathrm{d}x\, g(x)\ln|f(x,y)|\right] \leq \exp\left\{\int_X \mathrm{d}x\, g(x)\ln\left[\int_Y \mathrm{d}y\, h(y)|f(x,y)|\right]\right\}, \tag{32}$$

valid for $h(y) \geq 0$, $g(x) \geq 0$ and $\int_X g(x)\,\mathrm{d}x = 1$. We obtain

$$\ln \frac{\bar{I}_1(\boldsymbol{r},s,t_0,t_1)}{\bar{I}_0(\boldsymbol{r},s,t_0,t_1)} \leq \int_0^1 \mathrm{d}x \ln \frac{\int_{t_0}^{t_1} \mathrm{d}t\, I_0(\boldsymbol{r},s,t) K(x,t)}{\int_{t_0}^{t_1} \mathrm{d}t\, I_0(\boldsymbol{r},s,t)}\,, \tag{33}$$

or, again using $\ln x \leq x - 1$ for $x > 0$,

$$\ln \frac{\bar{I}_0(\boldsymbol{r},s,t_0,t_1)}{\bar{I}_0(\boldsymbol{r},s,t_0,t_1)} \geq \frac{\int_0^1 \mathrm{d}x \int_{t_0}^{t_1} \mathrm{d}t\, \langle \boldsymbol{r}|\mathrm{e}^{-txH_0}(1-\mathrm{e}^{-tV})\mathrm{e}^{-t(1-x)H_0}|s\rangle}{\int_{t_0}^{t_1} \mathrm{d}t\, I_0(\boldsymbol{r},s,t)}\,. \tag{34}$$

Combining Eqs. (29) and (34) gives

$$\begin{aligned}\frac{\int_0^1 \mathrm{d}x \int_{t_0}^{t_1} \mathrm{d}t\;\; t\langle \boldsymbol{r}|\mathrm{e}^{-txH_0} V \mathrm{e}^{-t(1-x)H_0}|s\rangle}{\int_{t_0}^{t_1} \mathrm{d}t\, I_0(\boldsymbol{r},s,t)} &\geq \ln \frac{\bar{I}_0(\boldsymbol{r},s,t_0,t_1)}{\bar{I}_1(\boldsymbol{r},s,t_0,t_1)} \\ &\geq \frac{\int_0^1 \mathrm{d}x \int_{t_0}^{t_1} \mathrm{d}t\, \langle \boldsymbol{r}|\mathrm{e}^{-txH_0}(1-\mathrm{e}^{-tV})\mathrm{e}^{-t(1-x)H_0}|s\rangle}{\int_{t_0}^{t_1} \mathrm{d}t\, I_0(\boldsymbol{r},s,t)}\,.\end{aligned} \tag{35}$$

The similarity between Eq. (35) and the bounds (26) on the ratio of the instantaneous intensities is striking: Each quantity has simply been replaced by its time-integrated value.

6.3. Bounds on the difference

Weaker bounds, not on the ratio but on the difference of the intensities, can be obtained as follows. Rewriting the upper bound in Eq. (35) as

$$\ln \frac{\bar{I}_1(\boldsymbol{r},s,t_0,t_1)}{\bar{I}_0(\boldsymbol{r},s,t_0,t_1)} \geq -\frac{\int_0^1 \mathrm{d}x \int_{t_0}^{t_1} \mathrm{d}t\, t\langle \boldsymbol{r}|\mathrm{e}^{-txH_0} V \mathrm{e}^{-t(1-x)H_0}|s\rangle}{\int_{t_0}^{t_1} \mathrm{d}t\, I_0(\boldsymbol{r},s,t)}\,, \tag{36}$$

and using $\ln x < x - 1$ for $x > 0$ we find

$$\bar{I}_1(\boldsymbol{r}, s, t_0, t_1) - \bar{I}_0(\boldsymbol{r}, s, t_0, t_1) \geq -\int_0^1 \mathrm{d}x \int_{t_0}^{t_1} \mathrm{d}t\, t \langle \boldsymbol{r}| \mathrm{e}^{-txH_0} V \mathrm{e}^{-t(1-x)H_0} |s\rangle \,. \tag{37}$$

An upper bound can be derived by starting from Eq. (24) and invoking Jensen's inequality once more. We obtain

$$\langle \boldsymbol{r}| \mathrm{e}^{-t(H_0+V)} |s\rangle \leq \int_0^1 \mathrm{d}x \langle \boldsymbol{r}| \mathrm{e}^{-txH_0} \mathrm{e}^{-tV} \mathrm{e}^{-t(1-x)H_0} |s\rangle \,, \tag{38}$$

or equivalently

$$\bar{I}_1(\boldsymbol{r}, s, t_0, t_1) - \bar{I}_0(\boldsymbol{r}, s, t_0, t_1) \leq -\int_0^1 \mathrm{d}x \langle \boldsymbol{r}| \mathrm{e}^{-txH_0} (1 - \mathrm{e}^{-tV}) \mathrm{e}^{-t(1-x)H_0} |s\rangle \,. \tag{39}$$

Combining Eqs. (37) and (39) yields

$$\begin{aligned} \int_0^1 \mathrm{d}x \int_{t_0}^{t_1} \mathrm{d}t \langle \boldsymbol{r}| \mathrm{e}^{-txH_0} (1 - \mathrm{e}^{-tV}) \mathrm{e}^{-t(1-x)H_0} |s\rangle &\leq \bar{I}_0(\boldsymbol{r}, s, t_0, t_1) - \bar{I}_1(\boldsymbol{r}, s, t_0, t_1) \\ &\leq \int_0^1 \mathrm{d}x \int_{t_0}^{t_1} \mathrm{d}t\, t \langle \boldsymbol{r}| \mathrm{e}^{-txH_0} V \mathrm{e}^{-t(1-x)H_0} |s\rangle \,. \end{aligned} \tag{40}$$

Comparing Eqs. (35) and (40) it is clear that the upper and lower bounds contain essentially the same information.

6.4. Illustrative examples

In this subsection we consider some simple cases for which the upper and lower bounds derived above can be worked out analytically. We only treat the case of instantaneous light detection and a point source, i.e. $|s\rangle = |\boldsymbol{r}'\rangle$ where $\boldsymbol{r}'$ denotes the position of the source.

As a starter consider the case of uniform absorption by the medium. With $H_1 = -D_0 \nabla^2 + V_1$ and $H_0 = -D_0 \nabla^2$, Eq. (22) reduces to

$$tV_1 \geq \ln \frac{I_0(\boldsymbol{r}, \boldsymbol{r}', t)}{I_1(\boldsymbol{r}, \boldsymbol{r}', t)} \geq tV_1 \geq 1 - \mathrm{e}^{-tV_1} \,, \tag{41}$$

as expected because $I_0(\boldsymbol{r}, \boldsymbol{r}', t)/I_1(\boldsymbol{r}, \boldsymbol{r}', t) = \mathrm{e}^{tV_1}$.

Next consider the case of a point absorber (i.e. $V(\boldsymbol{r}) = V_2 \delta(\boldsymbol{r} - \boldsymbol{r}_0)$ and $\mathrm{e}^{-tV(\boldsymbol{r})} = 1 + (\mathrm{e}^{-tV_2} - 1)\delta(\boldsymbol{r} - \boldsymbol{r}_0)$, $V_2 > 0$) embedded in an homogeneous infinite medium. In this case

$$\langle \boldsymbol{r}| \mathrm{e}^{-tH_0} |\boldsymbol{r}'\rangle = G_d(\boldsymbol{r} - \boldsymbol{r}', D_0 t) \,, \tag{42}$$

where

$$G_d(\boldsymbol{r}, x) = \left(\frac{1}{4\pi x}\right)^{d/2} \mathrm{e}^{-r^2/4x} \,, \tag{43}$$

describes the light diffusion in the infinite medium without the absorber. Here and in the following d denotes the dimension of the system. Straightforward algebra gives

$$\frac{\langle \boldsymbol{r}|\mathrm{e}^{-txH_0}V\mathrm{e}^{-t(1-x)H_0}|\boldsymbol{r}'\rangle}{\langle \boldsymbol{r}|\mathrm{e}^{-tH_0}|\boldsymbol{r}'\rangle} = V_2 G_d(\boldsymbol{r}_0-(1-x)\boldsymbol{r}-x\boldsymbol{r}',\, x(1-x)D_0t) \tag{44a}$$

and

$$\frac{\langle \boldsymbol{r}|\mathrm{e}^{-txH_0}\mathrm{e}^{-tV}\mathrm{e}^{-t(1-x)H_0}|\boldsymbol{r}'\rangle}{\langle \boldsymbol{r}|\mathrm{e}^{-tH_0}|\boldsymbol{r}'\rangle} = 1+(\mathrm{e}^{-tV_2}-1)G_d(\boldsymbol{r}_0-(1-x)\boldsymbol{r}-x\boldsymbol{r}',\, x(1-x)D_0t)\,. \tag{44b}$$

The inequalities (26) become

$$tV_2F(\boldsymbol{r}_0,\boldsymbol{r},\boldsymbol{r}',t) \geq \ln\frac{I_0(\boldsymbol{r},\boldsymbol{r}',t)}{I_1(\boldsymbol{r},\boldsymbol{r}',t)} \geq (1-\mathrm{e}^{-tV_2})F(\boldsymbol{r}_0,\boldsymbol{r},\boldsymbol{r}',t)\,, \tag{45}$$

where

$$F(\boldsymbol{r}_0,\boldsymbol{r},\boldsymbol{r}',t) = \int_0^1 \mathrm{d}x\, G_d(\boldsymbol{r}_0-(1-x)\boldsymbol{r}-x\boldsymbol{r}',\, x(1-x)D_0t)\,. \tag{46}$$

For P point objects, the inequalities corresponding to Eq. (45) read

$$t\sum_{p=1}^{P} V_2^{(p)}F(\boldsymbol{r}_0^{(p)},\boldsymbol{r},\boldsymbol{r}',t) \geq \ln\frac{I_0(\boldsymbol{r},\boldsymbol{r},t)}{I_1(\boldsymbol{r},\boldsymbol{r},t)} \geq \sum_{p=1}^{P}(1-\mathrm{e}^{-tV^{(p)}{}_2})F(\boldsymbol{r}_0^{(p)},\boldsymbol{r},\boldsymbol{r}',t)\,, \tag{47}$$

suggesting that the reflected signal is a superposition of intensities "emitted" by the P "point sources" located at $\boldsymbol{r}_0^{(p)}$.

The above example can be analysed in more detail by considering the case of backscattering. Then $\boldsymbol{r}=\boldsymbol{r}'$ and

$$tV_2\int_0^1 \mathrm{d}x\, G_d(\boldsymbol{r}_0-\boldsymbol{r},\, x(1-x)D_0t) \geq \frac{I_0(\boldsymbol{r},\boldsymbol{r},t)}{I_1(\boldsymbol{r},\boldsymbol{r},t)} \geq (1-\mathrm{e}^{-tV_2})\int_0^1 \mathrm{d}x\, G_d(\boldsymbol{r}_0-\boldsymbol{r},\, x(1-x)D_0t)\,, \tag{48}$$

showing that for a point object, $\ln[I_0(\boldsymbol{r},\boldsymbol{r},t)/I_1(\boldsymbol{r},\boldsymbol{r},t)]/(1-\mathrm{e}^{-tV_2})$ is larger than the light intensity resulting from a superposition of light pulses emitted by the point object and received by the detector. In this case there is a clear physical interpretation of the upper and lower bounds themselves. Our simulation results presented below, show that this interpretation is qualitatively correct, also for the more complicated case $\boldsymbol{r}\neq\boldsymbol{r}'$ and/or $|s\rangle \neq |\boldsymbol{r}'\rangle$.

From the t-dependence of bounds such as Eqs. (45) and (48), we may expect that they contain useful information about the absorber if tV_2 is sufficiently small (but $\tau_1 \ll t$ of course). In general, $\ln[I_0(\boldsymbol{r},\boldsymbol{r},t)/I_1(\boldsymbol{r},\boldsymbol{r},t)]$ or $\ln[\bar{I}_0(\boldsymbol{r},\boldsymbol{r},t_0,t_1)/\bar{I}_1(\boldsymbol{r},\boldsymbol{r},t_0,t_1)]$ will only show signatures of the object(s) if $\tau_1 \leq \tau_2 \leq t \leq \tau_3$ or $\tau_1 \leq \tau_2 \leq t_0 \leq t_1 \leq \tau_3$ respectively, where τ_2 and τ_3 have to be determined by (numerical) experiment. For the turbid media of interest, $V_2 \approx 24\,\mathrm{ns}^{-1}$ and $D_0 \approx 0.6\,\mathrm{cm}^2/\mathrm{ns}$. Putting for instance $t = 1.5\,\mathrm{ns}$ we find

$$36 \geq \left(\int_0^1 \mathrm{d}x\, G_d(\boldsymbol{r}_0-\boldsymbol{r},x(1-x)D_0t)\right)^{-1}\ln\frac{I_0(\boldsymbol{r},\boldsymbol{r},t)}{I_1(\boldsymbol{r},\boldsymbol{r},t)} \geq 1\,, \tag{49}$$

demonstrating that the presence of a small object can have a substantial effect on the processed signal.

7. Image processing technique: Simulation results

Application of the theory presented above is much more straightforward than the mathematics used might suggest. In practice, the procedure is as follows: Measure the intensity $\bar{I}(\boldsymbol{r}, s, t_0, t_1) = \int_{t_0}^{t_1} \mathrm{d}t \langle \boldsymbol{r}|\mathrm{e}^{-tH}|s\rangle$ and calculate or measure the reference signal $\bar{I}_0(\boldsymbol{r}, s, t_0, t_1)$ corresponding to a "test-model" H_0 for various detector-positions $\boldsymbol{r}$. The resulting ratio $\ln \bar{I}(\boldsymbol{r}, s, t_0, t_1)/\bar{I}_0(\boldsymbol{r}, s, t_0, t_1)$ (or difference $\bar{I}_0(\boldsymbol{r}, s, t_0, t_1) - \bar{I}(\boldsymbol{r}, s, t_0, t_1)$) should reveal whether there are hidden objects or not. The simulation results presented below demonstrate that this procedure works and in the next section we show that it also works in real experiment. We will use the term "processed" signal whenever we mean $\ln \bar{I}(\boldsymbol{r}, s, t_0, t_1)/\bar{I}_0(\boldsymbol{r}, s, t_0, t_1)$. In the remainder of this work we set $t_0 = t_\mathrm{d}$ and $t_1 = t_0 + \Delta t$ and we confine ourselves to presenting results obtained from intensities integrated over a finite interval (i.e. Δt).

Guided by the experiments on breast tissue (see the discussion in the introduction) in our simulations we will assume that the turbid medium is characterized by an absorption and reduced scattering factor $\mu_\mathrm{a} = 0.01\,\mathrm{mm}^{-1}$ and $\mu_\mathrm{s}' = 0.9\,\mathrm{mm}^{-1}$, respectively. For tumor tissue we will take $\mu_\mathrm{a} = 0.1\,\mathrm{mm}^{-1}$ and $\mu_\mathrm{s}' = 0.9\,\mathrm{mm}^{-1}$, unless explicitly mentioned otherwise.

Our simulations show that on a qualitative level, there is little difference between the results obtained from 2D or 3D models. Printed images obtained from 2D model simulations are more easy to interpret than their 3D counterpart. Therefore, in the discussion that follows we will mainly present results of 2D model simulations. For some selected cases we also show images obtained from 3D model simulations. Unless explicitly mentioned otherwise, the spatial mesh size $\delta = 1\,\mathrm{mm}$, the time step $\tau = 1\,\mathrm{ps}$, the source pulse time $t_\mathrm{p} = 10\,\mathrm{ps}$, the time at which the detectors start to record intensity $t_\mathrm{d} = t_0 = 500\,\mathrm{ps}$, and the 2D and 3D samples have dimensions $71\,\mathrm{mm} \times 71\,\mathrm{mm}$, and $63\,\mathrm{mm} \times 63\,\mathrm{mm} \times 63\,\mathrm{mm}$, respectively. The speed of light in the medium $v = 0.222\,\mathrm{mm/ps}$.

We will use the short-hand notation $\bar{I}_\mathrm{T}$ and $\bar{I}_\mathrm{R}$ for the transmitted and reflected intensity respectively, integrated over the corresponding detection area. All intensities given below are normalized with respect to the light intensity supplied by the source.

7.1. Effect of the source type and the time gate

In Fig. 13 we show results of a simulation for a sample containing an object of 2.5 mm radius, positioned at (36, 26) mm. The sample is illuminated by a source of diameter 1 mm centered around (0, 36) mm. In the sequel we will call such a small source a point source. Fig. 13a and c show the integrated intensity while Fig. 13b and d show the corresponding processed signal. For $\Delta t = 612\,\mathrm{ps}$ (Fig. 13a and b), it is clear that the object leaves no trace in the transmitted and reflected intensity whereas the processed data clearly indicate that there is an object inside the sample. For $\Delta t = 1836\,\mathrm{ps}$ (Fig. 13c and d) the transmitted intensity shows an asymmetry. Since the light source is positioned at (0, 36) mm this asymmetry indicates that there is an object immersed in the sample. In the reflected intensity, however, the object leaves no trace. In the processed reflected intensity the object is clearly visible. Note that the position of the maximum of the processed intensity changes

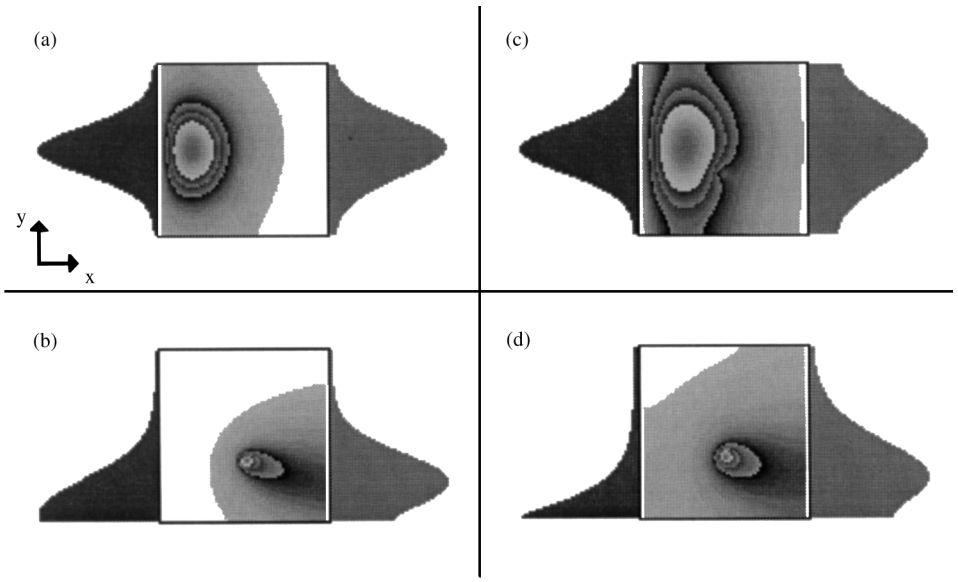

Fig. 13. Simulation of a time-resolved optical imaging experiment on a turbid medium with a reduced scattering factor $\mu_s' = 0.9\,\mathrm{mm}^{-1}$ and an absorption factor $\mu_a = 0.01\,\mathrm{mm}^{-1}$ containing a 2.5 mm radius object with absorption and reduced scattering factors $\mu_a = 0.1\,\mathrm{mm}^{-1}$ and $\mu_s' = 0.9\,\mathrm{mm}^{-1}$, respectively. The dimensions of the sample are $71\,\mathrm{mm} \times 71\,\mathrm{mm}$. The object is located at (36, 26) mm. The sample is illuminated by a source of diameter 1 mm centered around (0, 36) mm during a time $t_p = 10\,\mathrm{ps}$. (a) Time-integrated transmitted (right) and reflected (left) intensity for $\Delta t = 612\,\mathrm{ps}$. $\bar{I}_T \approx 0.6 \times 10^{-8}$ and $\bar{I}_R \approx 0.2 \times 10^{-2}$; (b) processed signal corresponding to (a); (c) same as (a) except that $\Delta t = 1836\,\mathrm{ps}$. $\bar{I}_T \approx 0.5 \times 10^{-6}$ and $\bar{I}_R \approx 0.3 \times 10^{-2}$; (d) processed signal corresponding to (c). The (processed) light intensities inside the sample are also shown.

with Δt (Fig. 13b and d). This effect is the largest for the processed reflected intensity. Qualitatively similar results are obtained by illuminating the sample with a light pulse of width $t_p = 100\,\mathrm{ps}$ or $t_p = 300\,\mathrm{ps}$ (results not shown).

Starting the recording of light intensity at a different point of time or changing Δt mainly affects the processed reflected intensity. An example is provided in Fig. 14 where we present simulation results for the same setup as the one of Fig. 13 except for the time t_0 at which the detection of light starts. Comparison of the results of Fig. 14a and b, corresponding to $t_0 = 1000\,\mathrm{ps}$ and $\Delta t = 612\,\mathrm{ps}$ ($t_1 = t_0 + \Delta t = 1612\,\mathrm{ps}$), with those of Fig. 13a and b where $t_0 = 500\,\mathrm{ps}$ and $\Delta t = 612\,\mathrm{ps}$ ($t_1 = 1112\,\mathrm{ps}$), shows that, Δt being the same, there are only minor differences in the processed reflected signal (the small changes in the background signal are due to the time integration and do not carry relevant information). Comparing the results shown in Fig. 14a and b with those of Fig. 14c and d where $t_0 = 500\,\mathrm{ps}$ and $\Delta t = 1112\,\mathrm{ps}$ ($t_1 = 1612\,\mathrm{ps}$) confirm that, the processed reflected intensity depends on t_0 and Δt, t_1 being the same. This is mainly due to the fact that for illumination by a point source, the maximum of the processed reflected intensity changes with Δt (see Fig. 13b and d). However, changing t_0 or Δt does not affect the detectability of the object.

Fig. 15a and b show simulation results for the same setup as the one used for Fig. 13c and d except that the light source is now positioned at (0, 16) mm. The transmitted and reflected

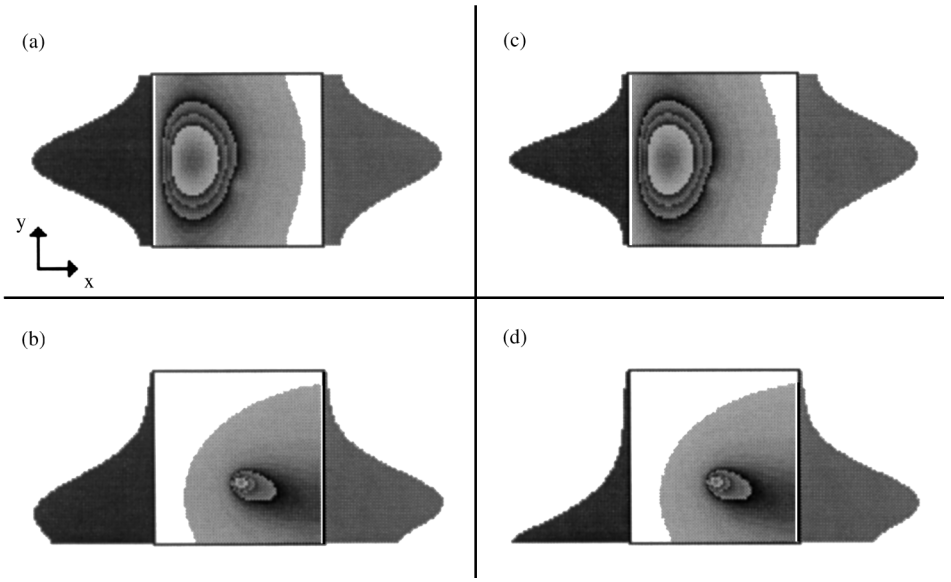

Fig. 14. Same as Fig. 13 except for the time t_0 at which the detection of light starts: (a) $t_0 = 1000$ ps and $\Delta t = 612$ ps. $\bar{I}_T \approx 0.1 \times 10^{-6}$ and $\bar{I}_R \approx 0.3 \times 10^{-3}$; (b) processed signal corresponding to (a); (c) same as (a) except that $t_0 = 500$ ps and $\Delta t = 1112$ ps. $\bar{I}_T \approx 0.1 \times 10^{-6}$ and $\bar{I}_R \approx 0.2 \times 10^{-2}$; (d) processed signal corresponding to (c). Medium: $(\mu_a, \mu_s') = (0.01, 0.9)\,\mathrm{mm}^{-1}$; object: $(\mu_a, \mu_s') = (0.1, 0.9)\,\mathrm{mm}^{-1}$.

intensities in Fig. 13c, d and Fig. 15a, b look completely different. As the image of the point source itself resembles the image of an object it is as good as impossible to conclude from the transmitted or reflected intensities whether or not there is an object inside the sample. The processed intensities however, correctly signal the presence of an object. From Fig. 13 and Fig. 15a, b, it follows that there is no obvious relationship between the position of the object and the maximum of the processed intensity.

Illumination of the sample by a source emitting a Gaussian light distribution of width 5 mm yields the results shown in Fig. 15c and d. These results can hardly be distinguished from those shown in Fig. 13c and d obtained by using a point source. Fig. 16 displays results for a system containing an object of 2.5 mm radius, positioned at (16, 26) mm. Fig. 16a and b show the time-integrated transmitted and reflected intensities for illumination by a point source while Fig. 16c and d show the intensities for uniform illumination of the whole left side of the sample. Using a point source yields no trace of the object in the reflected intensity and only a weak one in the transmitted intensity (Fig. 13a, c and Fig. 16a). In the processed signals, however, there is a clear signal of the object (Fig. 13b, d and Fig. 16b). Uniform illumination of the whole left side of the sample (Fig. 16c and d) yields a very weak signal of the object in the transmitted and reflected intensities and a clear signal in the processed intensities. The fingerprint of the object in the reflected intensity disappears completely if the object is more than 20 mm away from the entrance plane, while in the transmitted intensity the very weak signal is present, independent of the location of the object within the sample (results not shown). In the case of uniform illumination the position

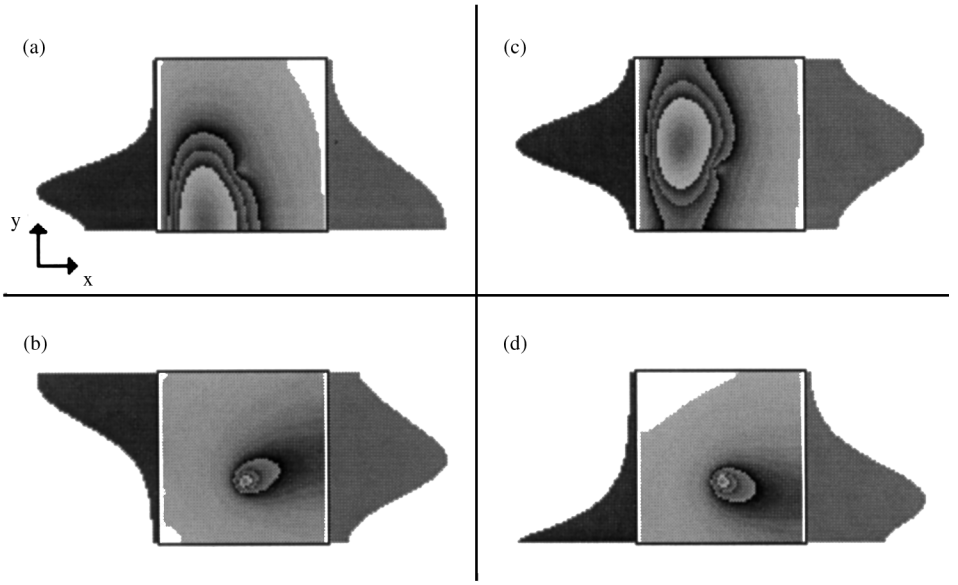

Fig. 15. Same as Fig. 13 except for the source illuminating the system. $\Delta t = 1836$ ps (a) Point source centered around (0,16) mm. $\bar{I}_T \approx 0.5 \times 10^{-6}$ and $\bar{I}_R \approx 0.3 \times 10^{-2}$; (b) processed signal corresponding to (a); (c) Source emitting a Gaussian light distribution of width 5 mm, centered around (0,36) mm. $\bar{I}_T \approx 0.5 \times 10^{-6}$ and $\bar{I}_R \approx 0.3 \times 10^{-2}$; (d) processed signal corresponding to (c). Medium: $(\mu_a, \mu_s') = (0.01, 0.09)\,\mathrm{mm}^{-1}$; object: $(\mu_a, \mu_s') = (0.1, 0.9)\,\mathrm{mm}^{-1}$.

of the maximum of the processed intensity does no longer change as a function of time (not shown) and corresponds to the y-coordinate of the position of the object. Uniform illumination of the other sides of the sample should therefore allow the determination of the position of the object. Uniform illumination during a time $t_p = 100$ ps or $t_p = 300$ ps (results not shown) yields qualitatively the same results as for $t_p = 10$ ps, just as in the case of illumination by a point source.

If the distance between the object and the illuminated side of the sample is approximately 10 mm or less, the time-integrated reflected intensity clearly shows a signature of the object provided the source is sufficiently large. This is illustrated in Fig. 17, which displays results for a system containing an object of 2.5 mm radius, positioned at (10, 26) mm. Fig. 17a–d show the time-integrated transmitted and reflected intensities for illumination of the sample by a source emitting circular light distributions of various size. Using a point source (Fig. 17a) yields no trace of the object in the reflected intensity and only a weak one in the transmitted intensity. Increasing the radius of the source improves the detectability of the object in the reflected and transmitted intensities, as shown in Fig. 17b and d. For a source of radius 30 mm (Fig. 17c) the ratio between the dip and maximum is approximately 0.6, which is nearly the same as for uniform illumination of the whole left side of the sample (Fig. 17d). As mentioned above, even with uniform illumination of the sample the fingerprint of the object in the reflected intensity disappears completely if the object is more than 20 mm away from the entrance plane (results not shown). Note that unlike Fig. 13c and d, Fig. 17 displays only the results of time-integrated intensities.

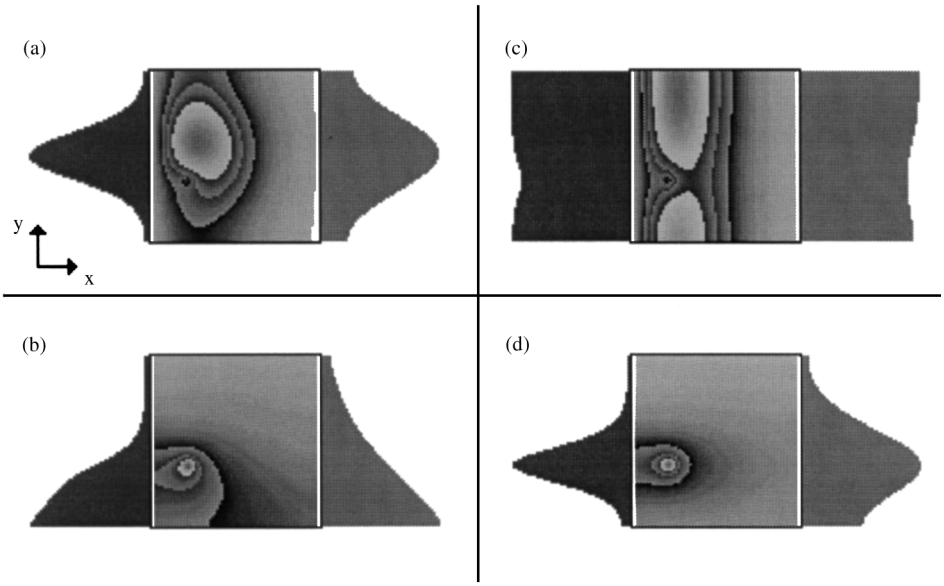

Fig. 16. Same as Fig. 13 except for the source illuminating the system and the position of the object $(16, 26)$ mm. $\Delta t = 1836$ ps. (a) Point source centered around (0.36) mm. $\bar{I}_T \approx 0.6 \times 10^{-6}$ and $\bar{I}_R \approx 0.2 \times 10^{-2}$; (b) processed signal corresponding to (a); (c) Uniform illumination of the left side of the sample. $\bar{I}_T \approx 0.6 \times 10^{-6}$ and $\bar{I}_R \approx 0.2 \times 10^{-2}$; (d) processed signal corresponding to (c). Medium: $(\mu_a, \mu_s') = (0.01, 0.9)\,\mathrm{mm}^{-1}$; object: $(\mu_a, \mu_s') = (0.1, 0.9)\,\mathrm{mm}^{-1}$.

7.2. Small objects

In Fig. 18 we present simulation results for a system containing an object of 0.5 mm radius. For comparison the setup is kept the same as the one used for Fig. 16. As seen from Fig. 18a, using a point source, it is no longer possible to detect the object in the transmitted intensity. Also for uniform illumination of the whole left side of the sample the fingerprint of the small object in the transmitted and reflected intensities (Fig. 18c) is much weaker than for an object of radius 2.5 mm (Fig. 16c). In the simulation the object always leaves a trace in the processed signals, independent of its location in the sample. Evidently, due to the signal-to-noise ratio, this will not necessarily be the case in experiment. From Figs. 16 and 18 it is clear that it is very difficult, not to say impossible, to infer the size of the object from the measured intensities.

7.3. System size and mesh size

Repeating the simulations for the same set-up as the one of Fig. 13 but reducing the mesh size by a factor two and the time step by a factor four gives the same results as the ones shown in Fig. 13. Reducing the diameter of the object, hidden in this sample, to 0.5 mm yields the results displayed in Fig. 19. In the processed transmitted intensity the object is still clearly visible.

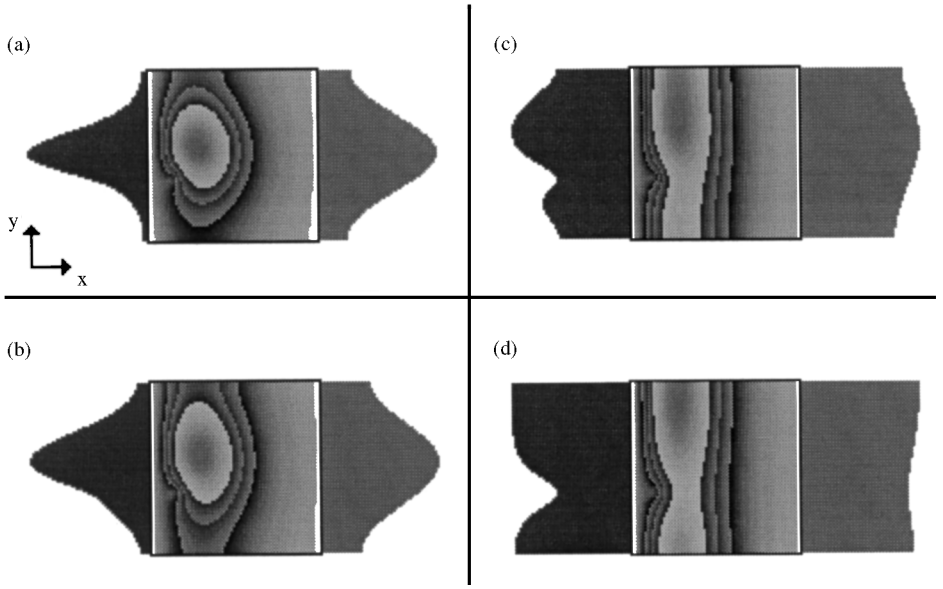

Fig. 17. Same as Fig. 13 except for the source illuminating the system and the position of the object (10, 26) mm. Only time-integrated transmitted (right) and reflected (left) intensities are shown for $\Delta t = 1836$ ps: (a) point source centered around (0, 36) mm. $\bar{I}_T \approx 0.6 \times 10^{-6}$ and $\bar{I}_R \approx 0.2 \times 10^{-2}$; (b) source emitting a circular light distribution of radius 15 mm, centered around (0, 36) mm. $\bar{I}_T \approx 0.5 \times 10^{-6}$ and $\bar{I}_R \approx 0.2 \times 10^{-2}$; (c) source emitting a circular light distribution of radius 30 mm, centered around (0.36) mm. $\bar{I}_T \approx 0.5 \times 10^{-6}$ and $\bar{I}_R \approx 0.2 \times 10^{-2}$; (d) uniform illumination of the left side of the sample. $\bar{I}_T \approx 0.6 \times 10^{-6}$ and $\bar{I}_R \approx 0.2 \times 10^{-2}$. Medium: $(\mu_a, \mu_s') = (0.01, 0.9)\,\mathrm{mm}^{-1}$; object: $(\mu_a, \mu_s') = (0.1, 0.9)\,\mathrm{mm}^{-1}$.

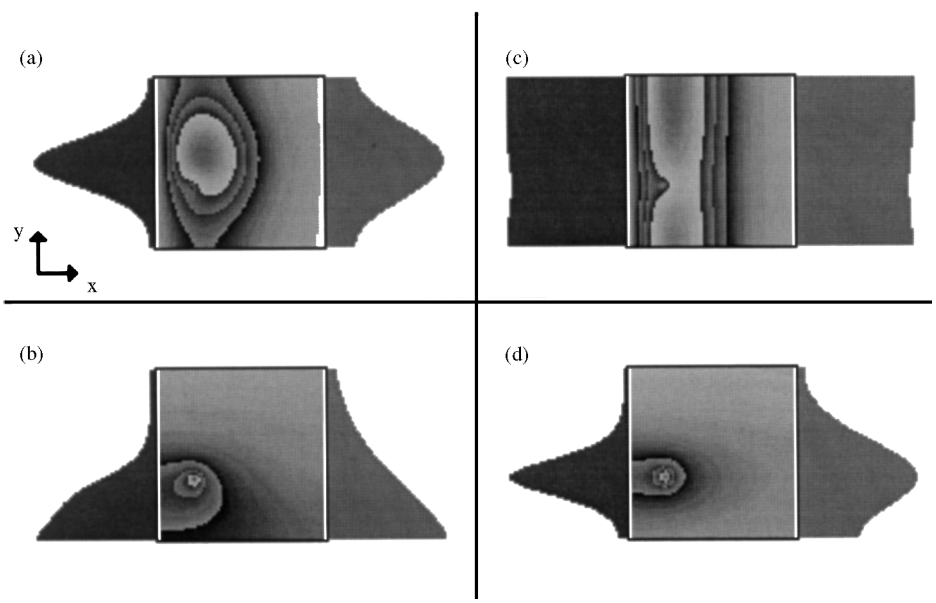

Fig. 18. Same as Fig. 16 except that the object has a radius of 0.5 mm. Medium: $(\mu_a, \mu_s') = (0.01, 0.9)\,\mathrm{mm}^{-1}$; object: $(\mu_a, \mu_s') = (0.1, 0.9)\,\mathrm{mm}^{-1}$.

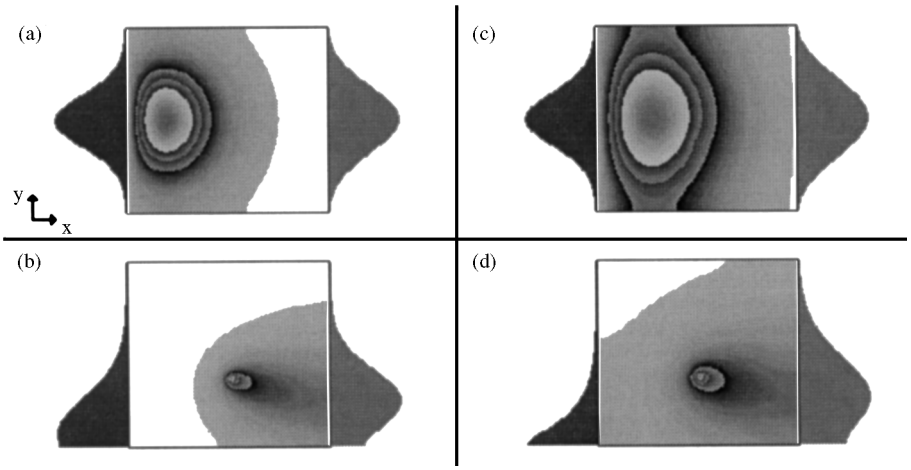

Fig. 19. Same as Fig. 13 except that the object has a radius of 0.25 mm. (a) $\Delta t = 614$ ps. $\bar{I}_T \approx 0.7 \times 10^{-8}$ and $\bar{I}_R \approx 0.3 \times 10^{-2}$; (b) processed signal corresponding to (a); (c) same as (a) except that $\Delta t = 1843$ ps. $\bar{I}_T \approx 0.8 \times 10^{-6}$ and $\bar{I}_R \approx 0.3 \times 10^{-2}$; (d) processed signal corresponding to (c). Medium: $(\mu_a, \mu_s') = (0.01, 0.9)\,\mathrm{mm}^{-1}$; object: $(\mu_a, \mu_s') = (0.1, 0.9)\,\mathrm{mm}^{-1}$.

7.4. $D(\boldsymbol{r})$ versus D_0

An interesting question for theoretical developments is to what extent the propagation of light is affected by replacing, in the TDDE, the diffusion coefficient $D(\boldsymbol{r})$ by its homogeneous counterpart $D_0 = v/3(\bar{\mu}_s' + \bar{\mu}_a)$. In Fig. 20 we present some results of a calculation in which we address that question. Usually, we compute the light intensity in the full model $H = -\nabla D(\boldsymbol{r})\nabla + V(\boldsymbol{r})$ and compare it to the light intensity in the approximate model $H_0 = -D_0\nabla^2 + V_0(\boldsymbol{r})$. The results are depicted in Fig. 20a and b for the same sample as in Fig. 13 except that the radius of the object is 0.5 mm. Comparing the light intensity of the full model H with the light intensity in the approximate model $H_0' = -D_0\nabla^2 + V(\boldsymbol{r})$ yields the results shown in Fig. 20 c and d. The processed intensities only show the effect of replacing $D(\boldsymbol{r})$ by D_0. We find that this approximation changes the processed intensities by no more than 2%. For most practical purposes, it will be safe to replace $D(\boldsymbol{r})$ by D_0, unless the reduced scattering factors of the medium and objects differ significantly.

7.5. More than one object

In Fig. 21 we show a result of a simulation for a sample containing two objects of 0.5 mm radius which are positioned 15 mm from each other. The sample is illuminated by a point source. The transmitted and reflected intensities (Fig. 21a and c) show no trace of the objects. For $\Delta t = 612$ ps the processed data give a weak indication that there are two objects hidden in the sample and that they are not positioned symmetrically with respect to the position of the light source. For $\Delta t = 1836$ ps (Fig. 21c and d) the reflected processed data signals two objects immersed in the system while the transmitted processed data suggests that there is only one object inside the

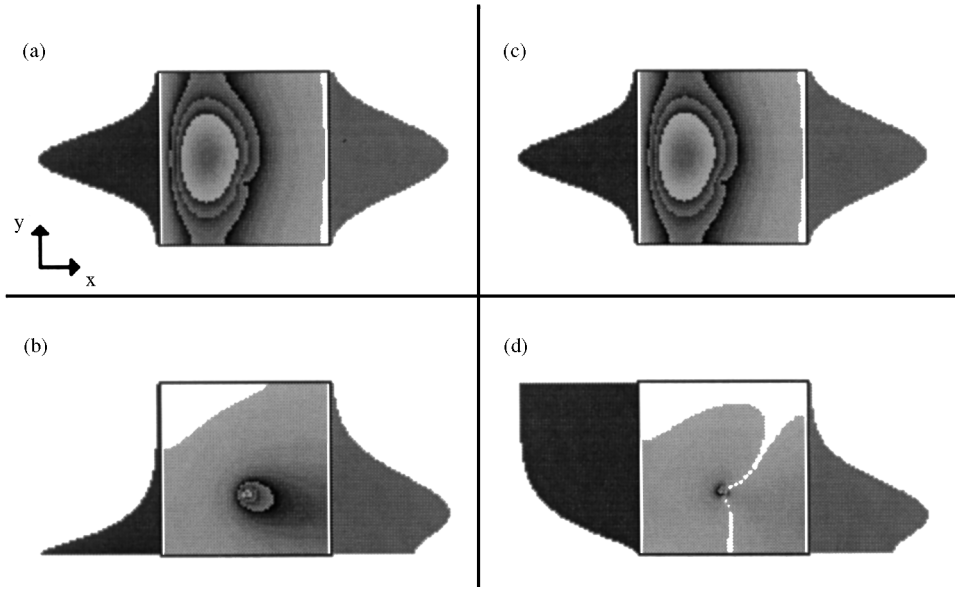

Fig. 20. Same as Fig. 13 except that the object has a radius of 0.5 mm. (a) $\Delta t = 1836$ ps. $\bar{I}_T \approx 0.6 \times 10^{-6}$ and $\bar{I}_R \approx 0.3 \times 10^{-2}$; (b) processed signal using reference model H_0 and corresponding to (a); (c) same as (a); (d) processed signal using reference model H_0' and corresponding to (c). Medium: $(\mu_a, \mu_s') = (0.01, 0.9)\,\mathrm{mm}^{-1}$; object: $(\mu_a, \mu_s') = (0.1, 0.9)\,\mathrm{mm}^{-1}$.

sample. Additional simulations (see Fig. 22) indicate that in reflection it is possible to resolve the two objects down to a separation distance of 2 mm by using the appropriate time gate. Note that, unlike Fig. 21c, Fig. 22c displays the results of the processed intensities.

Fig. 23 displays the results for the same setup as the one of Fig. 21 but instead of a point source, uniform illumination is been used. Although there is a weak signal in the transmitted intensity (see Fig. 23a and c) the two objects cannot be distinguished. In the reflected intensity the objects leave no trace. For $\Delta t = 767$ ps the two objects appear in both the processed transmitted and reflected intensities (see Fig. 23b). For larger Δt (e.g. Fig. 23d) the images of the objects merge and cannot be distinguished from an image of a single object. In general, we find that in order to resolve nearby objects it is expedient to employ a point source.

In Fig. 24 we depict the simulation results for the same setup as before (Fig. 21) except that the sample contains three objects of 0.5 mm radius. The transmitted and reflected intensities (Fig. 24a and c) show no sign of an object but the processed intensities (Fig. 24b and d) do. As can be seen from Fig. 24b and d it is very difficult to determine, from the maxima of the processed intensities, the number and positions of the objects: The processed transmitted and reflected intensity suggest the presence of two objects and one object respectively.

In Fig. 25 we show results of a simulation of a sample containing several 0.5 mm radius objects. The sample is uniformly illuminated on its left side. In Fig. 25a and b the three objects are located at exactly the same position as in Fig. 24c and d. In Fig. 25a there is a very weak trace of only two objects in the transmitted signal and no trace of objects in the reflected intensity. Previously, we

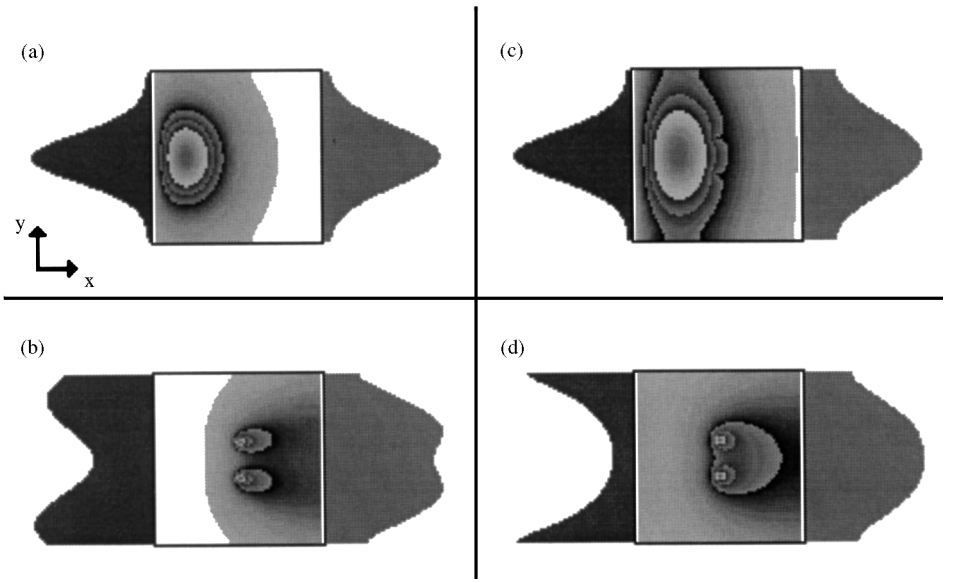

Fig. 21. Simulation of a time-resolved optical imaging experiment on a sample containing two 0.5 mm-radius objects located at (36, 43) mm and at (36, 28) mm. The sample is illuminated by a point source centered around (0, 36) mm. (a) $\Delta t = 612$ ps, $I_T \approx 0.6 \times 10^{-8}$ and $\bar{I}_R \approx 0.2 \times 10^{-2}$; (b) processed signal corresponding to (a); (c) same as (a) but $\Delta t = 1836$ ps, $\bar{I}_T \approx 0.5 \times 10^{-6}$ and $\bar{I}_R \approx 0.3 \times 10^{-2}$; (d) processed signal corresponding to (c). Medium: $(\mu_a, \mu_s') = (0.01, 0.9)\,\mathrm{mm}^{-1}$; object: $(\mu_a, \mu_s') = (0.1, 0.9)\,\mathrm{mm}^{-1}$.

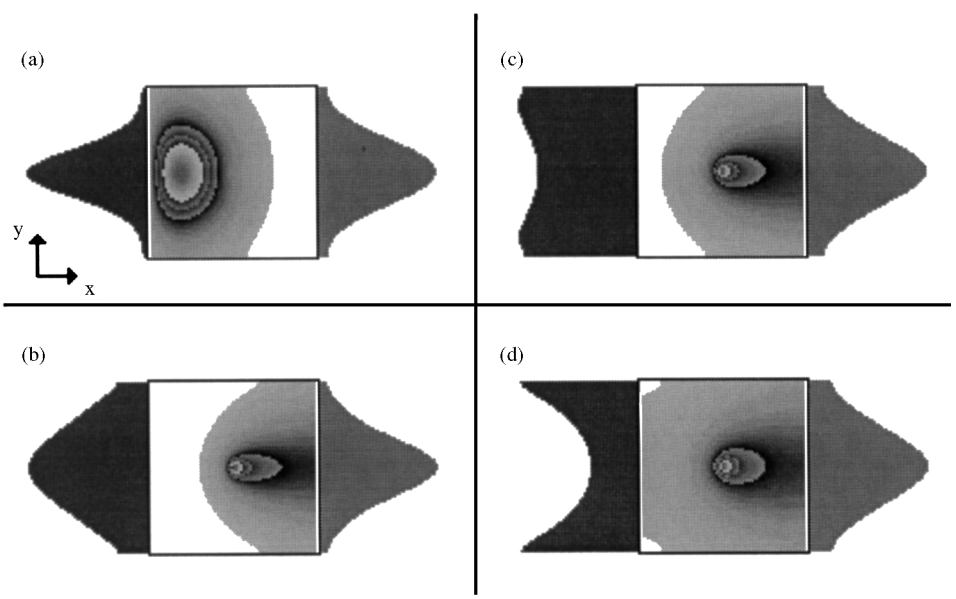

Fig. 22. Same as Fig. 21 except that the two objects are located at (36, 37) mm and at (36, 35) mm. (a) $\Delta t = 612$ ps, $I_T \approx 0.6 \times 10^{-8}$ and $\bar{I}_R \approx 0.2 \times 10^{-2}$; (b) processed signal corresponding to (a); (c) processed signal corresponding to (a) but for $\Delta t = 1224$ ps, $\bar{I}_T \approx 0.1 \times 10^{-6}$ and $\bar{I}_R \approx 0.2 \times 10^{-2}$; (d) same as (c) but $\Delta t = 1836$ ps, $\bar{I}_T \approx 0.5 \times 10^{-6}$ and $\bar{I}_R \approx 0.3 \times 10^{-2}$. The (processed) light intensities inside the sample are also shown. Medium: $(\mu_a, \mu_s') = (0.01, 0.9)\,\mathrm{mm}^{-1}$; object: $(\mu_a, \mu_s') = (0.1, 0.9)\,\mathrm{mm}^{-1}$.

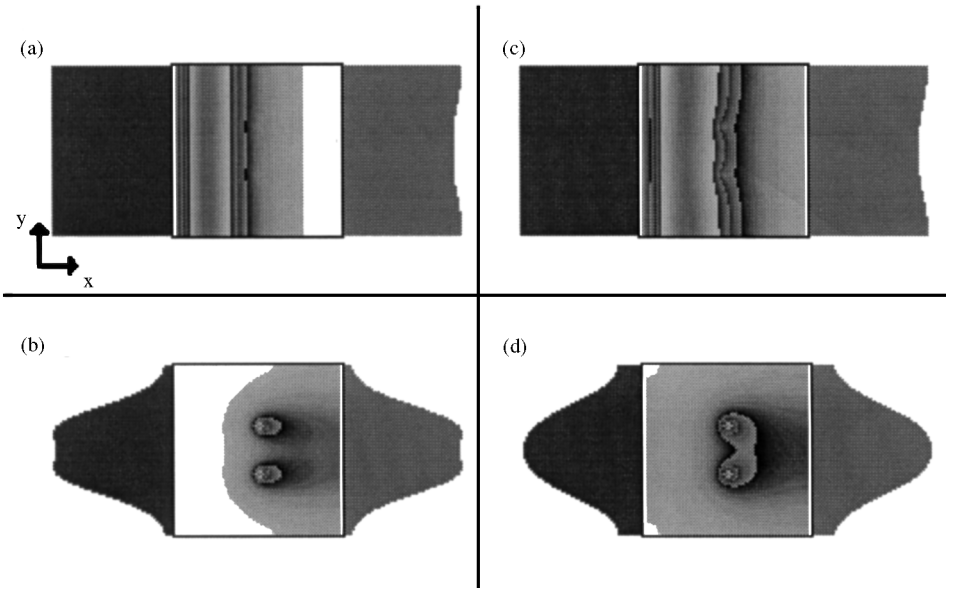

Fig. 23. Same as Fig. 21 except that the sample is illuminated uniformly on its whole left side. (a) $\Delta t = 693$ ps, $\bar{I}_T \approx 0.1 \times 10^{-7}$ and $\bar{I}_R \approx 0.2 \times 10^{-2}$; (b) processed signal corresponding to (a); (c) same as (a) except that $\Delta t = 1881$ ps. $\bar{I}_T \approx 0.6 \times 10^{-6}$ and $\bar{I}_R \approx 0.3 \times 10^{-2}$; (d) processed signal corresponding to (c). Medium: $(\mu_a, \mu_s') = (0.01, 0.9)\,\mathrm{mm}^{-1}$; object: $(\mu_a, \mu_s') = (0.1, 0.9)\,\mathrm{mm}^{-1}$.

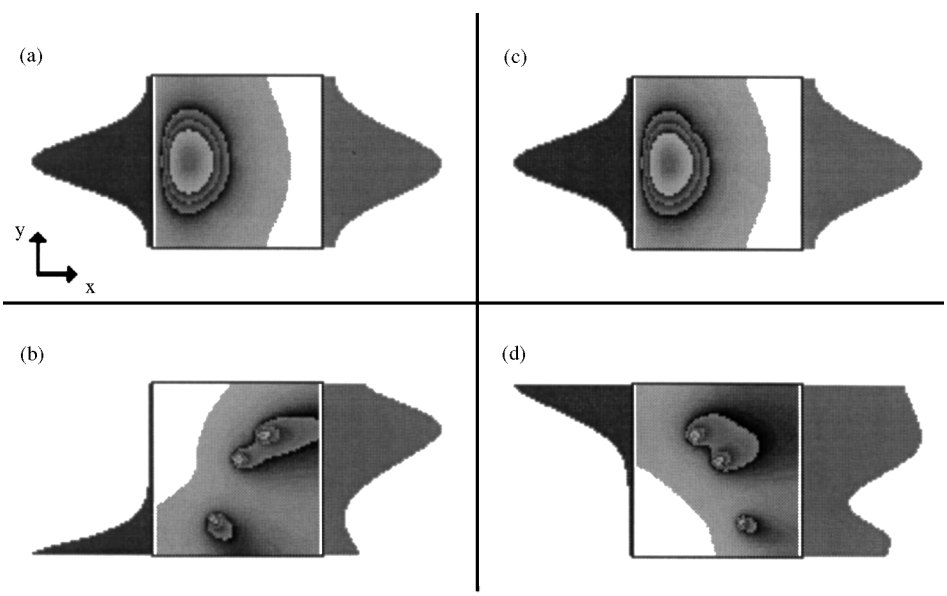

Fig. 24. Simulation of a sample containing three 0.5 mm radius objects located at (46, 50) mm, (36, 40) mm and (26, 15) mm. The sample is illuminated by a point source. (a) $\Delta t = 816$ ps, $\bar{I}_T \approx 0.3 \times 10^{-7}$ and $\bar{I}_R \approx 0.2 \times 10^{-2}$; (b) processed signal corresponding to (a); (c) same as (a) except that the objects are positioned at (26, 50) mm, (36, 40) mm and (46, 15) mm, $\bar{I}_T \approx 0.3 \times 10^{-7}$ and $\bar{I}_R \approx 0.2 \times 10^{-2}$; (d) processed signal corresponding to (c). Medium: $(\mu_a, \mu_s') = (0.01, 0.9)\,\mathrm{mm}^{-1}$; object: $(\mu_a, \mu_s') = (0.1, 0.9)\,\mathrm{mm}^{-1}$.

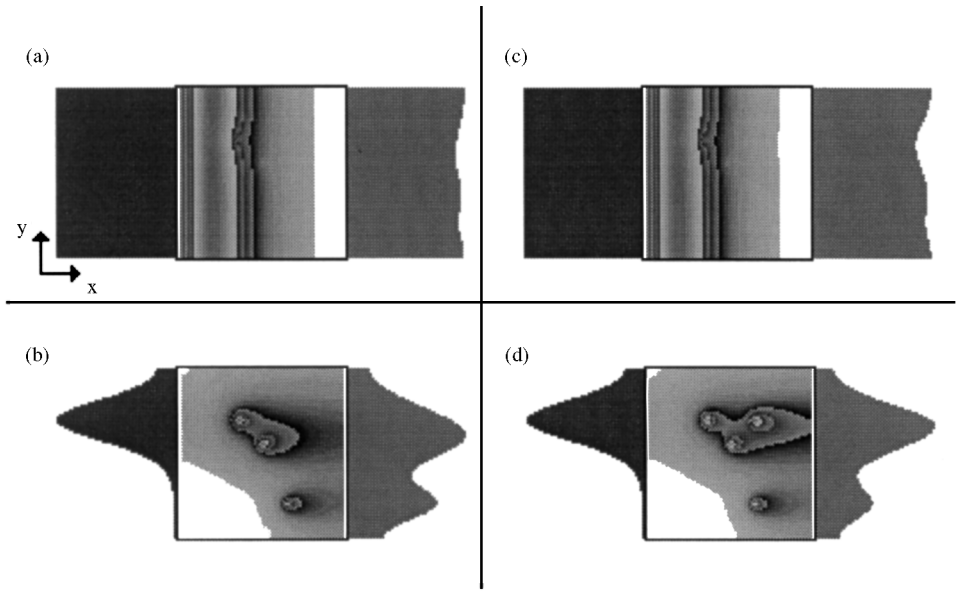

Fig. 25. Simulation of samples containing several 0.5 mm-radius objects. The sample is illuminated uniformly on its left side. (a) Three objects located at (26, 50) mm, (36, 40) mm and (46, 15) mm, $\Delta t = 816$ ps, $\bar{I}_T \approx 0.3 \times 10^{-7}$ and $\bar{I}_R \approx 0.2 \times 10^{-2}$; (b) processed signal corresponding to (a); (c) Four objects located at (26, 50) mm, (36, 40) mm, (46, 15) mm and (46, 50) mm, $\Delta t = 816$ ps, $\bar{I}_T \approx 0.3 \times 10^{-7}$ and $\bar{I}_R \approx 0.2 \times 10^{-2}$; (d) processed signal corresponding to (c). Medium: $(\mu_a, \mu_s') = (0.01, 0.9)\,\mathrm{mm}^{-1}$; object: $(\mu_a, \mu_s') = (0.1, 0.9)\,\mathrm{mm}^{-1}$.

have seen that using uniform illumination it should be possible to determine the y-coordinate of a single object. This is also the case here. From the processed transmitted and reflected intensities in Fig. 25b we may conclude that there are at least three objects in the sample: The position of the maximum in the processed reflected data corresponds to the y-coordinate of the position of the centre of the uppermost object, the maxima of the smallest peak in the processed transmitted data corresponds to the y-coordinates of the downmost objects and the maximum of the largest peak in the processed transmitted data corresponds to the two upper objects. However, depending on the positions of the objects, the method cannot resolve all objects. An example is shown in Fig. 25d: four objects are hidden in the sample but the processed reflected and transmitted intensities suggest the presence of three objects only.

7.6. Random fluctuations

For some categories of biological tissues, including human breasts, the hypothesis of an homogeneous medium containing evenly distributed light scatterers does not seem correct, indicating that the tissue heterogeneities have to be taken into account in order to model accurately the photon migration in biological media [61]. In this section we use our simulation technique to study the effect of random fluctuations in the absorption and reduced scattering factor of the medium. Unless mentioned otherwise the absorption and reduced scattering factor of the medium fluctuate randomly around their spatial averages by 2%.

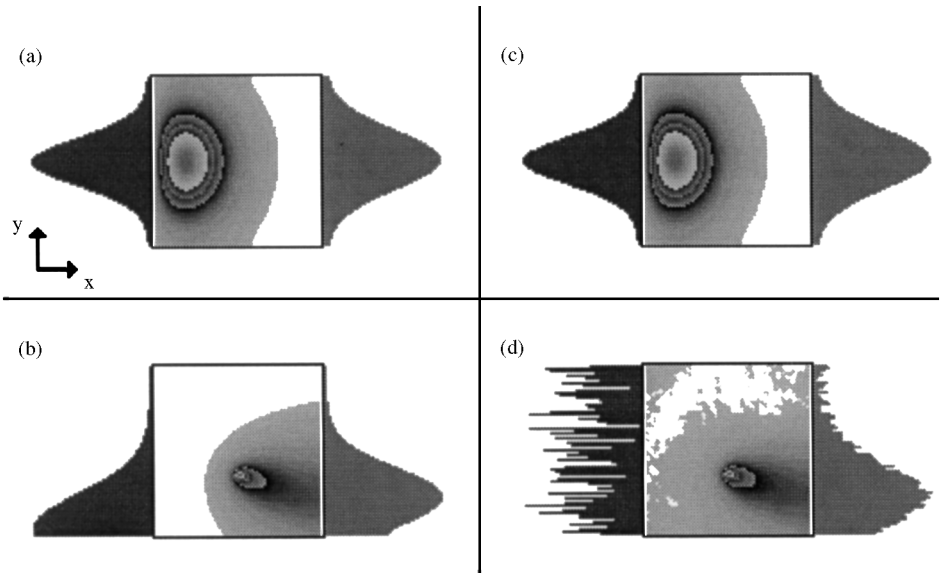

Fig. 26. Simulation of the same sample as in Fig. 20. (a) $\Delta t = 612\,\text{ps}$, $\bar{I}_T \approx 0.6 \times 10^{-8}$ and $\bar{I}_R \approx 0.2 \times 10^{-2}$; (b) processed signal corresponding to (a); (c) same as (a) except that the reduced scattering and absorption factor of the medium fluctuate randomly by at most 2%. $\bar{I}_T \approx 0.6 \times 10^{-8}$ and $\bar{I}_R \approx 0.2 \times 10^{-2}$; (d) processed signal corresponding to (c). Medium: $(\mu_a, \mu_s') = (0.01, 0.9)\,\text{mm}^{-1}$; object: $(\mu_a, \mu_s') = (0.1, 0.9)\,\text{mm}^{-1}$.

Fig. 26a and b show simulation results for the case that the medium is homogeneous, and Fig. 26c and d depict the results for the same sample with random fluctuations in the absorption and reduced scattering factor of the medium. The object of 0.5 mm radius leaves no trace in the transmitted and reflected intensity (Fig. 26a and c). The processed transmitted intensity indicates that there is an object inside the sample, in spite of the random fluctuations in the absorption and reduced scattering factor of the medium (Fig. 26b and d). In the processed reflected intensity the object is only visible if the medium is homogeneous. Increasing the gate time Δt does not help to make the object appear in the processed reflected signal. An example is shown in Fig. 27a and b for $\Delta t = 2610\,\text{ps}$. The processed signals do not change with time if the medium itself is not homogeneous.

Increasing t_0 can improve the signal-to-noise ratio intensity and can make it possible to find the 0.5 mm object, as illustrated in Fig. 27d for $t_0 = 2500\,\text{ps}$. The object cannot be detected in the processed reflected intensity if light detection starts at an earlier time. The optimal choice of t_0 depends on the size of the object and on the position of the object inside the sample, an example being provided in Fig. 28. Comparison of Fig. 28a and b and Fig. 16c and d demonstrates that except for the noise on the processed signals the results are qualitatively the same. Illuminating the same system with a point source (results not shown) yields qualitatively the same results as the ones displayed in Fig. 16a and b. In Fig. 28c and d we depict simulation results for the case where there is an object of 2.5 mm radius hidden inside the sample and the detection of light starts at $t_0 = 2000\,\text{ps}$. The object leaves a trace in the processed transmitted as well as in the processed reflected intensity. This trace disappears when the light detection is started at an earlier time. For

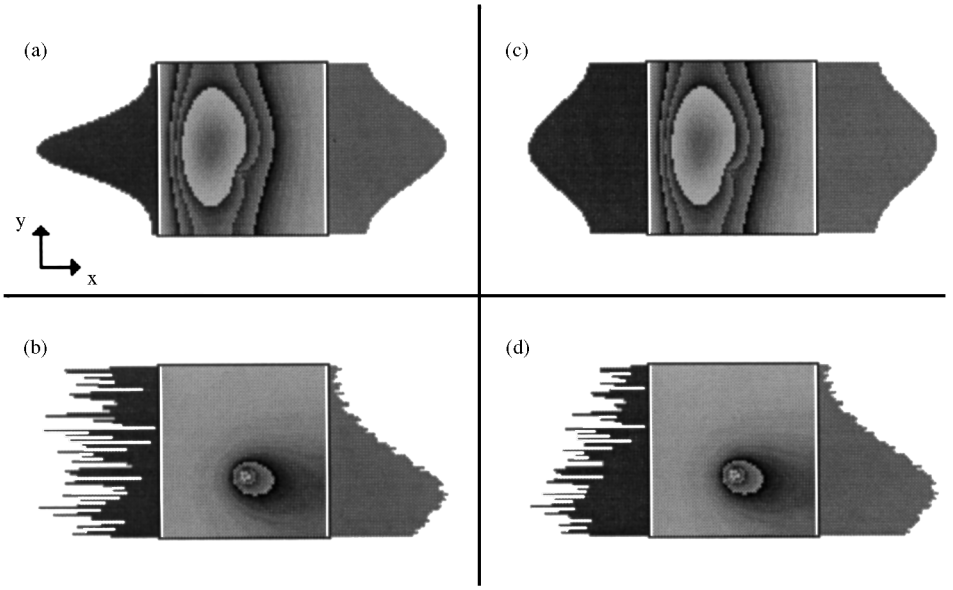

Fig. 27. Same as Fig. 26 except for the choice of t_0. (a) $t_0 = 500$ ps and $\Delta t = 2610$ ps. $\bar{I}_T \approx 0.9 \times 10^{-6}$ and $\bar{I}_R \approx 0.3 \times 10^{-2}$; (b) processed signal corresponding to (a); (c) same as (a) except that $t_0 = 2500$ ps and $\Delta t = 612$ ps. $\bar{I}_T \approx 0.3 \times 10^{-6}$ and $\bar{I}_R \approx 0.3 \times 10^{-5}$; (d) processed signal corresponding to (c). Medium: $(\mu_a, \mu_s') = (0.01, 0.9)\,\mathrm{mm}^{-1}$; object: $(\mu_a, \mu_s') = (0.1, 0.9)\,\mathrm{mm}^{-1}$.

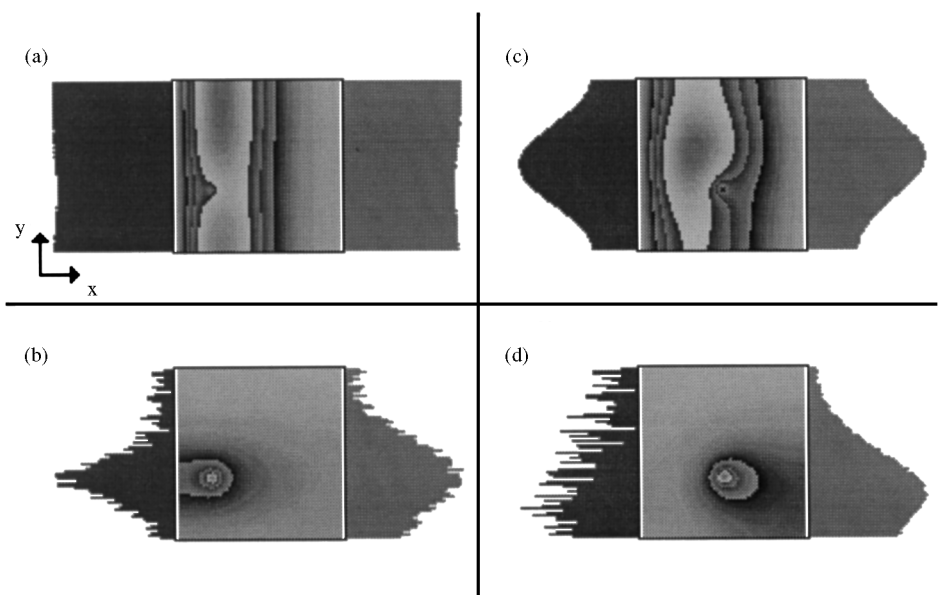

Fig. 28. Simulation of the same sample as in Fig. 16 (Fig. 28a and b) and Fig. 13 (Fig. 28c and d) except that the reduced scattering and absorption factor of the medium fluctuate randomly by at most 2%. (a) Uniform illumination of the left side of the sample, $\Delta t = 1836$ ps, $\bar{I}_T \approx 0.6 \times 10^{-6}$ and $\bar{I}_R \approx 0.2 \times 10^{-2}$; (b) processed signal corresponding to (a); (c) Point source centered around $(0, 36)$ mm, $\Delta t = 1836$ ps, $t_0 = 2000$ ps, $\bar{I}_T \approx 0.6 \times 10^{-6}$ and $\bar{I}_R \approx 0.2 \times 10^{-4}$; (d) processed signal corresponding to (c). Medium: $(\mu_a, \mu_s') = (0.01, 0.9)\,\mathrm{mm}^{-1}$; object: $(\mu_a, \mu_s') = (0.1, 0.9)\,\mathrm{mm}^{-1}$.

a fixed position of the object, the smaller the object, the larger t_0 has to be in order to detect the object in the processed reflected signal (see Fig. 27d and Fig. 28d). This is also the case for objects located deeper inside the medium, as shown in Fig. 28. The existence of an optimum delay time for visualizing an object embedded in a turbid medium has previously been discussed in Ref. [133].

7.7. 3D examples

In Fig. 29 we present results of a simulation for a sample of size $63\,\text{mm} \times 63\,\text{mm} \times 63\,\text{mm}$, containing a sphere of 2.5 mm radius, positioned at $(32, 30, 36)$ mm. The processed signals for illumination of the sample by a point source centered around $(0, 32, 32)$ mm and for uniform illumination of the sample on its whole left plane are shown in Fig. 29a, b and Fig. 29c, d respectively. Fig. 29a and c depict the results for $\Delta t = 245$ ps and Fig. 29b and d for $\Delta t = 949$ ps. The object is clearly visible in both the processed transmitted data and in the processed reflected

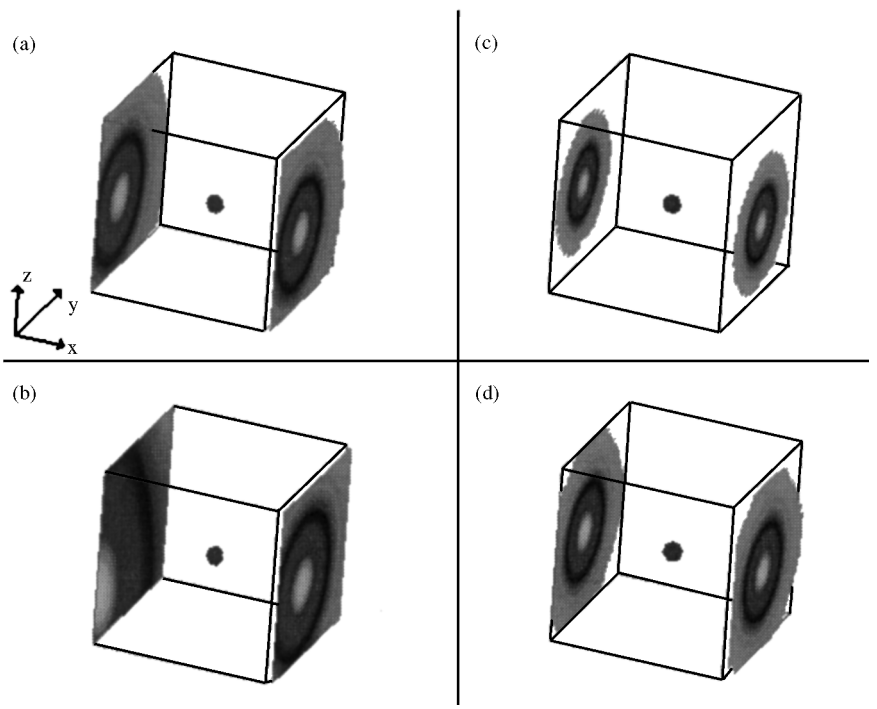

Fig. 29. Simulation of a time-resolved experiment on a turbid medium with a reduced scattering factor $\mu_s' = 0.9\,\text{mm}^{-1}$ and an absorption factor $\mu_a = 0.01\,\text{mm}^{-1}$ containing a 2.5 mm radius object with absorption and reduced scattering factors $\mu_a = 0.1\,\text{mm}^{-1}$ and $\mu_s' = 0.9\,\text{mm}^{-1}$, respectively. The dimensions of the sample are 63 mm × 63 mm × 63 mm and $t_0 = 500$ ps. The object is located at (32, 30, 36) mm. The sphere inside the sample denotes the position of the object. (a) Processed transmitted (right) and reflected (left) signal for $\Delta t = 245$ ps. The sample is illuminated by a source of diameter 1 mm centered around (0, 32, 32) mm during a time $t_p = 10$ ps. (b) Same as (a) except that $\Delta t = 949$ ps; (c) same as (a) except that the sample is uniformly illuminated on its whole left plane; (d) same as (c) except that $\Delta t = 949$ ps. Medium: $(\mu_a, \mu_s') = (0.01, 0.9)\,\text{mm}^{-1}$; object: $(\mu_a, \mu_s') = (0.1, 0.9)\,\text{mm}^{-1}$.

data. The position of the maximum of the processed intensity changes with Δt if a point source is used, just as in the 2D case.

Fig. 30 depicts simulation results for the same setup as the one used for Fig. 29. The sample is illuminated uniformly on its whole left plane. In Fig. 30a and b the sample contains a 2.5 mm diameter sphere, while in Fig. 30c and d the sample contains a 0.5 mm diameter sphere. Fig. 30a and b show the transmitted and reflected intensities and Fig. 30c and d show the corresponding processed signals. Only in the case of the 2.5 mm radius object there is a weak signal of the object in the transmitted intensity. In the processed signals, however, there is a clear signal of both the 2.5 mm radius object and the 0.5 mm object.

Fig. 31a and c display processed signals for the case that the medium is homogeneous, and Fig. 31b and d depict the processed signals for the same sample with random fluctuations in the absorption and reduced scattering factor of the medium. Fig. 31a and b show results for illumination of the sample by a point source and Fig. 31c and d show the results for uniform illumination of the sample on its whole left plane. In the processed reflected intensity the sphere of 0.5 mm is only visible if the medium is homogeneous. In the case of illumination of the sample by a point source the processed transmitted intensity indicates that there is an object hidden in the sample, in spite of the random fluctuations in the absorption and reduced scattering factor of the medium (Fig. 31a

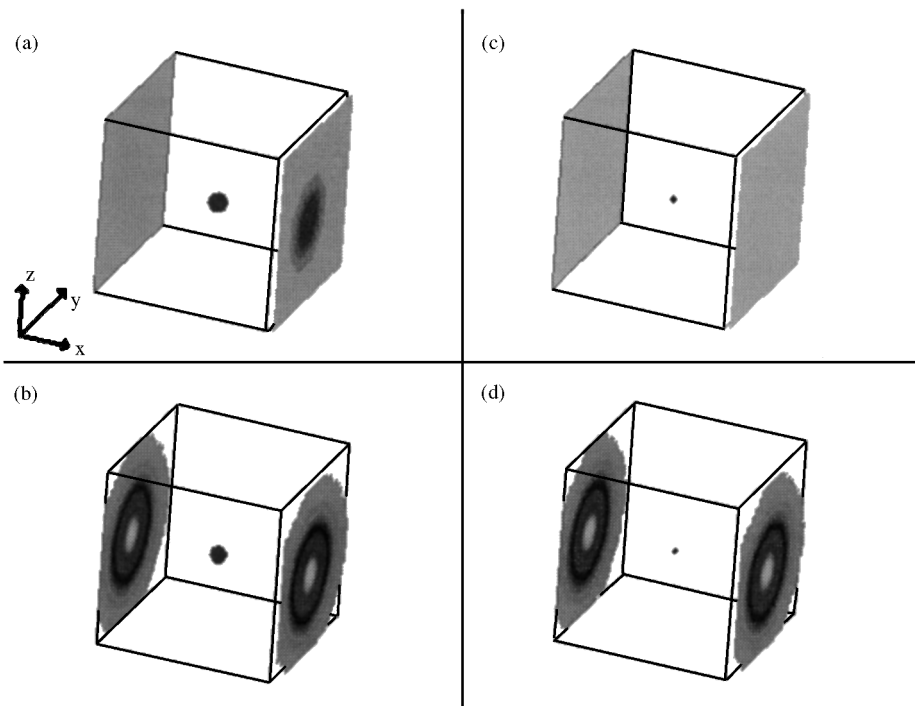

Fig. 30. Same as Fig. 29 except for the radius of the object. The sample is illuminated uniformly on its whole left plane. (a) Time-integrated transmitted (right) and reflected (left) intensity for $\Delta t = 857$ ps. The sample contains a 2.5 mm radius object. (b) processed signal corresponding to (a); (c) same as (a) except that the radius of the object is 0.5 mm; (d) processed signal corresponding to (c). Medium: $(\mu_a, \mu_s') = (0.01, 0.9)\,\mathrm{mm}^{-1}$; object: $(\mu_a, \mu_s') = (0.1, 0.9)\,\mathrm{mm}^{-1}$.

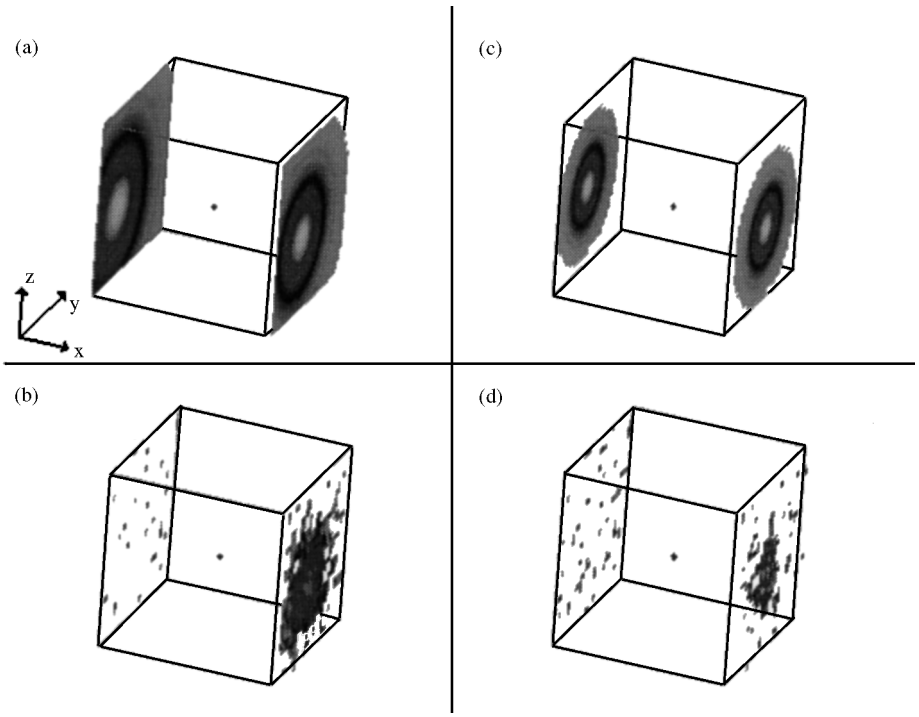

Fig. 31. Same as Fig. 29 except that the sample contains a 0.5 mm radius object. (a) Processed signal for $\Delta t = 444$ ps. The sample is illuminated by a source of diameter 1 mm centered around $(0, 32, 32)$ mm during a time $t_p = 10$ ps. (b) Same as (a) except that the reduced scattering and absorption factor of the medium fluctuate randomly by at most 1%; (c) same as (a) except that the sample is illuminated uniformly on its whole left plane; (d) same as (c) except that the reduced scattering and absorption factor of the medium fluctuate randomly by at most 1%. Medium: $(\mu_a, \mu_s') = (0.01, 0.9)\,\mathrm{mm}^{-1}$; object: $(\mu_a, \mu_s') = (0.1, 0.9)\,\mathrm{mm}^{-1}$.

and b). In the case of uniform illumination of the sample the sphere is only visible if the medium is homogeneous. Just as in 2D, increasing t_0 may improve the signal-to-noise ratio intensity (results not shown).

8. Image processing technique: Experimental results

As shown in the previous section the data processing method can be very useful to detect objects in turbid media. The fact that our simulation method reproduces experimental results suggests that the data processing technique might be useful in real experiments too. Hence, it is used to explore its usefulness in time-resolved reflection experiments on tissue-like phantoms [166]. The experimental setup is, apart from some small changes which will be discussed below, described in Section 5.2 and is depicted in Fig. 11. In this experiment the probe beam is expanded and collimated to a diameter of 2 cm using a set of two lenses in Keplerian configuration. Object detection in turbid media using the time-resolved reflectance curves is done in the following way:

First the measured reflectance curves are integrated numerically over a given time interval Δt, which is usually taken to be around 50 ps, for which the noise-to-signal ratio is good. The integrated intensities are then plotted as a function of the spatial coordinate y, resulting in a one-dimensional image. This image contains information on the inner structure of the sample.

The starting time t_0 of the integration window is set by scanning t_0 over the whole time range till the contrast in the processed signal is maximal. The optimal choice for t_0 is usually found to be in the tail of the reflectance curve ($t_0 > 200$–300 ps). In order to have a higher signal-to-noise ratio, the streak images are delayed in such a way that the maxima of the temporal intensity profiles fall out of the streak image and that larger measuring times can be used without having the streak camera saturated. Under these conditions the choice of Δt has little effect on the spatial profiles.

In the experiment we use a methacrylate vessel (70 mm × 70 mm × 70 mm) filled with a 10% of commercial intralipid-10% solution. At ($x = d$, $y = 25$ mm) we place a 1 mm diameter tube filled with blood. We vary d from 5 to 15 mm. To compare with the experimental results we performed

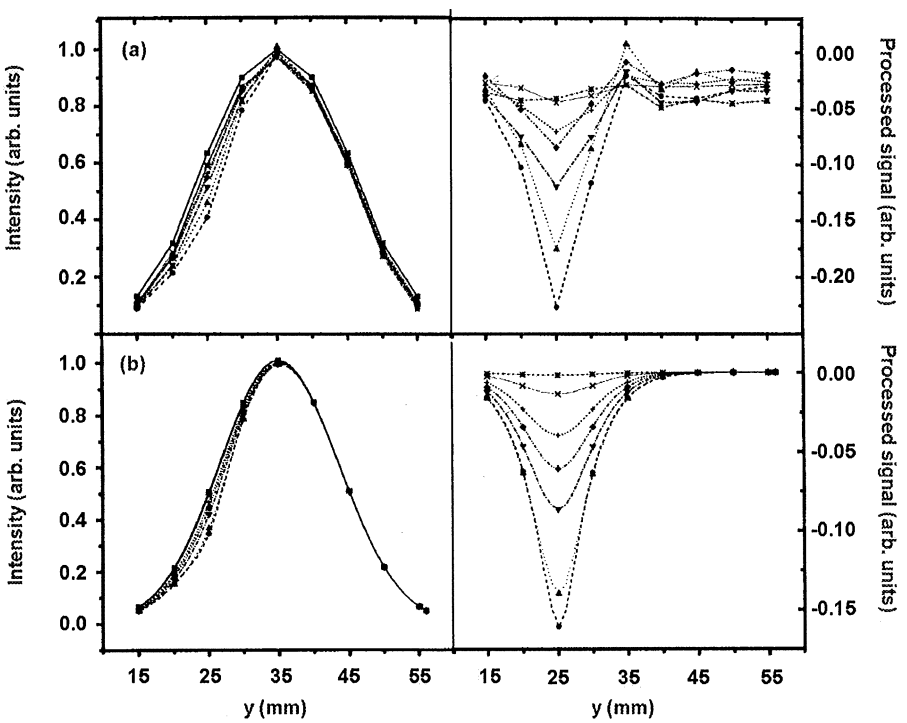

Fig. 32. Comparison of experimental and computer simulation results [166] for the time-resolved reflected light intensity. In the experiment and simulation the turbid medium has a reduced scattering factor $\mu_s' = 1\,\mathrm{mm}^{-1}$ and an absorption factor $\mu_a = 0.01\,\mathrm{mm}^{-1}$. The 1 mm diameter tube, located at ($x = d$, $y = 35$ mm), is filled with blood. In the simulations the tube has $\mu_a = 0.1\,\mathrm{mm}^{-1}$ and $\mu_s' = 1$. The sample is illuminated uniformly on the $x = 0$ plane. Circle: $d = 5$ mm; up triangle: $d = 6$ mm; down triangle: $d = 8$ mm; diamond: $d = 9$ mm, cross (+): $d = 10$ mm; cross (×): $d = 12$ mm; star: $d = 15$ mm; square: No object. (a) Experimental results for the reflected intensity (left) and the processed signal (right) for $t_d = 395$ ps and $\Delta t = 50$ ps; (b) same as (a) but for the simulation results. See also Figs. 3 and 5 of Ref. [166].

simulations for exactly the same system. The simulation is carried out in a manner identical to the procedure used in the time-resolved reflection technique, as described above. In Fig. 32 we show the experimental and simulation data, taken from Figs. 3 and 5 of Ref. [166]. Fig. 32a depicts the experimental data and Fig. 32b depicts the simulation data. The reflected intensities are shown on the left while the processed reflected intensities are shown on the right. In the processed intensities the tube is clearly distinguishable to depths of 15 mm from the illuminated surface. The simulation results are in excellent agreement with the experimental data.

9. Summary

We have described an algorithm that solves the time-dependent diffusion equation, taking into account spatial variations of the reduced scattering and absorption coefficient as well as random fluctuations in these quantities. The algorithm is unconditionally stable, accurate, efficient and unlike other stable algorithms, explicit. Futhermore, the algorithm can easily be modified to deal with samples of arbitrary shape.

On the basis of this algorithm a software package has been developed to simulate time-resolved optical imaging of objects immersed in strongly scattering media. Our simulation technique reproduces the experimental results on tissue-like phantoms, without the need of adjusting parameters, strongly suggesting that the time-dependent diffusion equation adequately describes the light propagation in these systems and that our software is working properly.

In the regime where the diffusion equation can be used to model the light transport in a turbid medium, the reduced scattering and the absorption factor can, in principle, be extracted from measured data by fitting to the measured data, simple expressions, derived from diffusion theory. We have used simulation data to assess the robustness of this approach and found that reliable estimates for both factors can be obtained from transillumination data, irrespective of the pulse time, the detector positions and the width of the beam (excluding illumination of a large area of the sample). In general, the estimates obtained from reflection measurements are less reliable.

Much of the current interest in time-resolved imaging with diffuse near-infrared light results from its potential to develop into a non-invasive and safe tool for breast cancer diagnosis. An important issue thereby is the size of the smallest object that can be detected. We have used our simulation approach to determine the conditions under which 1 mm diameter breast-cancer-like objects surrounded by a normal-tissue-like, strongly scattering, medium can be seen directly, i.e. without further processing of the measured intensities. Our findings are corroborated by experimental results on blood tubes immersed in intralipid solutions and suggest that without appropriate data processing the technique is of limited use.

As with many other imaging methods, the imaging power can be increased substantially by proper processing of the recorded data. For the case at hand this means that it is necessary to deal with the immense scattering, responsible for the blurring of the images of the object(s). In this paper we have described a simple procedure to enhance the image quality such that mm-sized objects can be located, under seemingly unfavourable conditions. We have given a mathematical justification of this procedure and have demonstrated that it works, not only in computer experiments but also in genuine experiments.

An essential feature of our data processing method is that it makes use of the diffusive part of the time-resolved light intensity only. We have presented a systematic study of the virtues and limitations of the data processing approach. An important finding is that for a particular source position, the position of the maxima in the recorded transmitted or reflected intensity can change with time, except for the rather ideal case of uniform illumination of one side of the sample. Several measurements for different source–detector arrangements are required to determine the actual position of an object. Furthermore, it seems very difficult to infer the size of the object from the measured intensities. In general, we found that proper processing of the diffuse time-resolved light intensity significantly enhances the signal-to-noise ratio, making it possible to detect the presence of mm-sized tumor-like objects in breast-like tissue.

For some categories of biological tissue, notably human breasts, it is unrealistic to assume that the sample can be modelled by a homogeneous strongly scattering medium. We have used our simulation method to study the effect of randomness in the absorption and reduced scattering factors of the medium on the detectability of the objects. We have found that the signal-to-noise ratio can be improved by increasing the delay between the time at which the source is turned off and the time at which the detectors start to record the light intensity.

A characteristic feature of the images obtained from time-resolved reflection or transillumination measurements of the diffuse light is that the information contained in these images is scrambled and therefore difficult to interpret correctly. As with other imaging techniques (such as e.g. high-resolution electron microscopy) that suffer from similar problems, it is expedient and sometimes also essential for the interpretation of the images to compare experimental results with model simulations. In this paper we have introduced a few theoretical concepts and then used these concepts to develop simulation and image processing algorithms specifically tuned to time-resolved imaging with diffuse light. Application of these ideas to actual experimental data has shown that this approach can be beneficial and suggests that further improvements to the imaging technique can be made by a more sophisticated processing of the measured time-resolved diffuse light intensity.

Acknowledgements

This work is supported by EEC and Spanish research contracts and by a supercomputer grant of the “Stichting Nationale Computer Faciliteiten (NCF)”.

References

[1] J.C. Hebden, D.J. Hall, M. Firbank, D.T. Delpy, Time-resolved optical imaging of a solid tissue-equivalent phantom, Appl. Opt. 34 (1995) 8038–8047.
[2] P. French, The light fantastic medical show, New Sci. 145 (1995) 25–29.
[3] M. Säbel, H. Aichinger, Recent developments in breast imaging, Phys. Med. Biol. 41 (1996) 315–368. *
[4] E. Carlsen, Transillumination light scanning, Diagn. Imaging 4 (60) (1982) 28–33.
[5] S. Nioka, M. Miwa, S. Orel, M. Shnall, M. Haida, S. Zhao, B. Chance, Optical imaging of human breast cancer, in: M.C. Hogan et al. (Eds.), Oxygen Transport to Tissue XVI, Plenum Press, New York, 1994, pp. 171–179.

[6] S.K. Gayen, R.R. Alfano, Emerging optical biomedical imaging techniques, Opt. Photonic News 7 (52) (1996) 16–22.
[7] J.C. Weinreb, G. Newstead, MR imaging of the breast, Radiology 196 (1995) 593–610.
[8] S.K. Wagner, Breast MRI: Limited specifity and high cost amper acceptance, Diagn. Imaging 18 (1996) 40–46.
[9] J. Christensen, S. Møller Nielsen, Ultrasonographic in vitro examination of nonpalbable breast masses, Act. Radiol. 36 (1995) 671–673.
[10] T.J. Rissanen, H.P. Mäkäräinen, M.A. Apaja-Sarkkinen, E.-L. Lindholm, Mammography and ultrasound in the diagnosis of contralateral breast cancer, Act. Radiol. 36 (1995) 358–366.
[11] C. Boetes, R.D.M. Mus, R. Holland, J.O. Barentsz, S.P. Strijk, T. Wobbes, J.H.C.L. Hendriks, S.H.J. Ruys, Breast tumors: Comparative accuracy of MR imaging relative to mammography, and US for demonstrating extent, Radiology 197 (1995) 743–747.
[12] P. Skaane, K. Engedal, A. Skjennald, Interobserver variation in the interpretation of breast imaging: Comparison of mammography, ultrasonography, and both combined in the interpretation of palpable noncalcified breast masses, Act. Radiol. 38 (1997) 497–502.
[13] B. Boné, Z. Péntek, L. Perbeck, B. Veress, Diagnostic accuracy of mammography and contrast-enhanced MR imaging in 238 histologically verified breast lesions, Act. Radiol. 38 (1997) 489–496.
[14] G.J. Müller, B. Chance, R.R. Alfano, S.R. Arridge, J. Beuthan, E. Gratton, M. Kaschke, B.R. Masters, S. Svanberg, P. van der Zee (Eds.), Medical Optical Tomography, in: Functional Imaging and Monitoring, SPIE Institute Series Vol. SI11, Society of Photo-Optical and Instrumentation Engineers, Bellingham, Washington, 1993.
[15] J.C. Hebden, R.A. Kruger, K.S. Wong, Time resolved imaging through a highly scattering medium, Appl. Opt. 30 (1991) 788–794.
[16] S. Andersson-Engels, R. Berg, A. Persson, S. Svanberg, Multispectral tissue characterization with time-resolved detection of diffusely scattered white light, Opt. Lett. 18 (1993) 1697–1699.
[17] O. Jarlman, R. Berg, S. Andersson-Engels, S. Svanberg, H. Pettersson, Time-resolved white light transillumination for optical imaging, Act. Radiol. 38 (1997) 185–189.
[18] D.A. Benaron, D.K. Stevenson, Optical time-of-flight and absorbance imaging of biologic media, Science 259 (1993) 1463–1466. **
[19] M.A. O'Leary, D.A. Boas, B. Chance, A.G, Yodh, Experimental images of heterogeneous turbid media by frequency-domain diffusing-photon tomography, Opt. Lett. 20 (1995) 426–428. *
[20] R. Berg, O. Jarlman, S. Svanberg, Medical transillumination imaging using short-pulse diode lasers, Appl. Opt. 32 (1993) 574–579. *
[21] B.B. Das, K.M. Yoo, R.R. Alfano, Ultrafast time-gated imaging in thick tissues: A step toward optical mammography, Opt. Lett. 18 (1993) 1092–1094.
[22] E.B. deHaller, C. Depeursinge, C.Y. Genton, Resolution of time-resolved breast transillumination: In vitro measurements compared with theoretical predictions, Opt. Eng. 34 (1995) 2084–2091. *
[23] D.G. Papaioannou, G.W. 'tHooft, J.J.M. Baselmans, M.J.C. van Gemert, Image quality in time-resolved transillumination of highly scattering media, Appl. Opt. 34 (1995) 6144–6157. *
[24] R. Berg, S. Andersson-Engels, O. Jarlman, S. Svanberg, Time-gated viewing studies on tissuelike phantoms, Appl. Opt. 35 (1996) 3432–3440.
[25] D. Grosenick, H. Wabnitz, H. Rinneberg, Time-resolved imaging of solid phantoms for optical mammography, Appl. Opt. 36 (1997) 221–231.
[26] C.L. Matson, N. Clark, L. McMackin, J.S. Fender, Three-dimensional tumor localization in thick tissue with the use of photon-density waves, Appl. Opt. 36 (1997) 214–220.
[27] A. Joblin, Tumor contrast in time-domain, near-infrared laser breast imaging, Appl. Opt. 36 (1997) 9050–9057.
[28] D.J. Hall, J.C. Hebden, D.T. Delpy, Imaging very-low-contrast objects in breastlike scattering media with a time-resolved method, Appl. Opt. 36 (1997) 7270–7276.
[29] M. Cutler, Transillumination as an aid in the diagnosis of breast lesions, Surg. Gynecol. Obstet. 48 (1929) 721–729.
[30] C. Gros, Y. Quennenville, Y. Hummel, Diaphanologie mammaire, J. Radiol. Electrol. 53 (1972) 297.
[31] B. Ohlsson, J. Gundersen, D. Nilsson, Diaphanography: A method for evaluation of the female breast, World J. Surg. 4 (1980) 701–707.
[32] D.J. Watmough, Transillumination of breast tissues: Factors governing optimal imaging of lesions, Radiology 147 (1983) 89–92.

[33] B. Monsees, J.M. Destouet, D. Gersell, Light scan evaluation of nonpalpable breast lesions, Radiology 163 (1987) 467–470.
[34] O. Jarlman, E. Lidbrink, G. Balldin, S.A. Larsson, Does transillumination lightscanning add any value to physical examination and mammography in diagnosis of breast cancer? Breast Dis. 9 (1996) 151–156.
[35] R.J. Grable, Optical tomography improves mammography, Laser Focus World 32 (1996) 113–118.
[36] S.B. Colak, D.G. Papaioannou, G.W.'t Hooft, M.B. van der Mark, H. Schomberg, J.C.J. Paasschens, J.B.M. Melissen, N.A.A.J. van Asten, Appl. Opt. 36 (1997) 180–213.
[37] S.A. Walker, S. Fantini, E. Gratton, Image reconstruction by back-projection from frequency-domain optical measurements in highly scattering media, Appl. Opt. 36 (1997) 170–179. *
[38] G. Mitic, J. Kölzer, J. Otto, E. Plies, G. Sölkner, W. Zinth, Time-gated transillumination of biological tissues and tissuelike phantoms, Appl. Opt. 33 (1994) 6699–6710. ***
[39] A. Yodh, B. Chance, Spectroscopy and imaging with diffusing light, Phys. Today 48 (1995) 34–40.
[40] S. Fantini, M.A. Franceschini, G. Gaida, E. Gratton, H. Jess, W.W. Mantulin, K.T. Moesta, P.M. Schlag, M. Kaschke, Frequency domain optical mammography: edge effect corrections, Med. Phys. 23 (1996) 149–157.
[41] S. Nioka, M. Miwa, S. Orel, M. Schnall, M. Haida, S. Zhao, B. Chance, Optical imaging of human breast cancer, Adv. Exp. Med. Biol. 361 (1994) 171–179.
[42] S. Ertefai, A.E. Profio, Spectral transmittance and contrast in breast diaphanography, Med. Phys. 12 (1985) 393–400.
[43] J. Alper, Transillumination: Looking right through you, Science 261 (1993) 560.
[44] G. Taubes, Play of light opens a new window into the body, Science 276 (1997) 1991–1993.
[45] H. Liu, D.A. Boas, Y. Zhang, A.G. Yodh, B. Chance, Determination of optical properties and blood oxygenation in tissue using continuous near-infrared light, Phys. Med. Biol. 40 (1995) 1983–1993. *
[46] N.B. Hampson, C.A. Piantadosi, Near-infrared monitoring of human skeletal muscle oxygenation during forearm ischaemia, J. Appl. Physiol. 64 (1988) 2449–2457.
[47] R.A. De Blasi, M. Cope, C.E. Elwell, F. Safoue, M. Ferrari, Noninvasive measurement of human forearm oxygen consumption by near infrared spectroscopy, Eur. J. Appl. Physiol. 67 (1993) 20–25.
[48] B. Chance, S. Nioka, J. Kent, K. McCully, M. Fountain, R. Greenfield, G. Holtom, Time-resolved spectroscopy of hemoglobin and myoglobin in resting and ischemic muscle, Anal. Biochem. 174 (1988) 698–707. *
[49] J.E. Brazy, D.V. Lewis, M.H. Mitnick, F.F. Jöbsis van der Vliet, Non-invasive monitoring of cerebral oxygenation in preterm infants: Preliminary observations, Paedeatrics 75 (1985) 217–225.
[50] J.S. Wyatt, M. Cope, D.T. Delpy, S. Wray, E.O. Reynolds, Quantitation of cerebral oxygenation and hemodynamics in sick newborn infants by near-infrared spectrophotometry, Lancet 2 (1986) 1063–1066.
[51] A.D. Edwards, J.S. Wyatt, C. Richardson, D.T. Delpy, M. Cope, E.O. Reynolds, Cotside measurement of cerebral blood flow in ill newborn infants by near-infrared spectroscopy, Lancet 2 (1988) 770–771.
[52] M. Cope, D.T. Delpy, System for long term measurement of cerebral blood and tissue oxygenation on newborn infants by near infrared transillumination, Med. Biol. Eng. Comput. 6 (1988) 289–294.
[53] M. Ferrari, E. Zanette, I. Giannini, G. Sideri, C. Fieschi, A. Carpi, Effect of carotid artery compression test on regional cerebral blood volume, haemoglobin oxygen saturation and cytochrome-c- oxidase redox level in cerebrovascular patients, Adv. Exp. Med. Biol. 200 (1986) 213–222.
[54] E. Okada, M. Firbank, M. Schweiger, S.R. Arridge, M. Cope, D.T. Delpy, Theoretical and experimental investigation of near-infrared light propagation in a model of the adult head, Appl. Opt. 36 (1997) 21–30.
[55] J.S. Maier, S.A. Walker, S. Fantini, M.A. Franceschini, E. Gratton, Possible correlation between blood glucose concentration and the reduced scattering coefficient of tissues in the near infrared, Opt. Lett. 19 (1994) 2062–2064.
[56] M. Kohl, M. Cope, M. Essenpreis, D. Böcker, Influence of glucose concentration on light scattering in tissue-simulating phantoms, Opt. Lett. 19 (1994) 2170–2172.
[57] M. Kohl, M. Essenpreis, M. Cope, The influence of glucose concentration upon the transport of light in tissue-simulating phantoms, Phys. Med. Biol. 40 (1995) 1267–1287.
[58] D.J. Watmough, Diaphanography: Mechanism responsible for the imaging, Act. Radiol. Oncol. 21 (1982) 11–15.
[59] A.E. Profio, G.A. Navarro, O.W. Sartorius, Scientific basis of breast diaphanography, Med. Phys. 16 (1989) 60–65.
[60] B.C. Wilson, S.L. Jacques, Optical reflectance and transmittance of tissues: Principles and applications, IEEE Quant. Electron. 26 (1990) 2186–2199.

[61] F. Bevilacqua, P. Marquet, O. Coquoz, C. Depeursinge, Role of tissue structure in photon migration through breast tissues, Appl. Opt. 36 (1997) 44–51.
[62] V.G. Peters, D.R. Wyman, M.S. Patterson, G.L. Frank, Optical properties of normal and diseased human breast tissues in the visible and near infrared, Phys. Med. Biol. 9 (1990) 1317–1334.
[63] H. Key, E.R. Davies, P.C. Jackson, P.N.T. Wells, Optical attenuation characteristics of breast tissues at visible and near-infrared wavelengths, Phys. Med. Biol. 36 (1991) 579–590.
[64] R. Marchesini, A. Bertoni, S. Andreola, E. Melloni, A.E. Sichirollo, Extinction and absorption coefficients and scattering phase functions of human tissues in vitro, Appl. Opt. 28 (1989) 2318–2324.
[65] K. Suzuki, Y. Yamashita, K. Ohta, B. Chance, Quantitative measurement of optical parameters in the breast using time-resolved spectroscopy, Invest. Radiol. 29 (1994) 410–414.
[66] J.B. Fishkin, O. Coquoz, E.R. Anderson, M. Brenner, B.J. Tromberg, Frequency-domain photon migration measurements of normal and malignant tissue optical properties in a human subject, Appl. Opt. 36 (1997) 10–20.
[67] A. Kienle, L. Lilge, M.S. Patterson, R. Hibst, R. Steiner, B.C. Wilson, Spatially resolved absolute diffuse reflectance measurements for noninvasive determination of the optical scattering and absorption coefficients of biological tissue, Appl. Opt. 35 (1996) 2304–2314.
[68] J.C. Hebden, S.R. Arridge, Imaging through scattering media by the use of an analytical model of perturbation amplitudes in the time domain, Appl. Opt. 35 (1996) 6788–6796. **
[69] J.M. Schmitt, A.H. Gandjbakhche, R.F. Bonner, Use of polarized light to discriminate short path photons in a multiply scattering medium, Appl. Opt. 31 (1992) 6535–6546.
[70] S.G. Demos, R.R. Alfano, Temporal gating in highly scattering media by the degree of optical polarization, Opt. Lett. 21 (1996) 161–163.
[71] O. Emile, F. Bretenaker, A. Le Floch, Rotating polarization imaging in turbid media, Opt. Lett. 21 (1996) 1706–1708.
[72] S.G. Demos, R.R. Alfano, Optical polarization imaging, Appl. Opt. 36 (1997) 150–155.
[73] E. Leith, C. Chen, H. Chen, Y. Chen, D. Dilworth, J. Lopez, J. Rudd, P.-C. Sun, J. Valdmanis, G. Vassler, Imaging through scattering media with holography, J. Opt. Soc. Am. A 9 (1992) 1148–1153.
[74] N.H. Abramson, K.G. Spears, Single pulse-in-flight recording by holography, Appl. Opt. 28 (1989) 1834–1841.
[75] A. Rebane, J. Feinberg, Time resolved holography, Nature 351 (1991) 378–380.
[76] L. Wang, P.P. Ho, C. Liu, G. Zhang, R.R. Alfano, Ballistic 2D imaging through scattering walls using an ultrafast optical Kerr gate, Science 253 (1991) 769–771.
[77] M.D. Duncan, R. Mahon, L.L. Tankersley, J. Reintjes, Time-gated imaging through scattering media using stimulated Raman amplification, Opt. Lett. 16 (1991) 1868–1870.
[78] S. Andersson-Engels, R. Berg, S. Svanberg, O. Jarlman, Time-resolved transillumination for medical diagnostics, Opt. Lett. 15 (1990) 1179–1181.
[79] R.R. Alfano, X. Liang, L. Wang, P.P. Ho, Time-resolved imaging of translucent droplets in highly scattering turbid media, Science 264 (1994) 1913–1915.
[80] J. Watson, P. Georges, T. Lépine, B. Alonzi, A. Brun, Imaging in diffuse media with ultrafast degenerate optical parametric amplification, Opt. Lett. 20 (1995) 231–233.
[81] D. Contini, H. Liszka, A. Sassaroli, G. Zaccanti, Imaging of highly turbid media by the absorption method, Appl. Opt. 35 (1996) 2315–2324.
[82] P.N. den Outer, Th.M. Nieuwenhuizen, A. Lagendijk, Location of objects in multiple-scattering media, J. Opt. Soc. Am. A 10 (1993) 1209–1218.
[83] M.A. O'Leary, D.A. Boas, B. Chance, A.G. Yodh, Refraction of diffuse photon density waves, Phys. Rev. Lett. 69 (1992) 2658–2661. **
[84] A. Knüttel, J.M. Schmitt, J.R. Knutson, Spatial localization of absorbing bodies by interfering diffuse photon-density waves, Appl. Opt. 32 (1993) 381–389.
[85] J.S. Reynolds, A. Przadka, S.P. Yeung, K.J. Webb, Optical diffusion imaging: a comparative numerical and experimental study, Appl. Opt. 35 (1996) 3671–3679.
[86] H. Jiang, K.D. Paulsen, U.L. Osterberg, B.W. Pogue, M.S. Patterson, Optical image reconstruction using frequency-domain data: Simulations and experiments, J. Opt. Soc. Am. A 13 (1996) 253–266.
[87] R. Cubeddu, A. Pifferi, P. Taroni, A. Torricelli, G. Valentini, Time-resolved imaging on a realistic tissue phantom: μ_s' and μ_a images versus time-integrated images, Appl. Opt. 35 (1996) 4533–4540.

[88] J.B. Fishkin, E. Gratton, Propagation of photon-density waves in strongly scattering media containing an absorbing semi-infinite plane bounded by a straight edge, J. Opt. Soc. Am. A 10 (1993) 127–140. **
[89] M.S. Patterson, J.D. Moulton, B.C. Wilson, K.W. Berndt, J.R. Lakowicz, Frequency-domain reflectance for the determination of the scattering and absorption properties of tissue, Appl. Opt. 30 (1991) 4474–4476. ***
[90] D.A. Boas, M.A. O'Leary, B. Chance, A.G. Yodh, Scattering and wavelength transduction of diffuse photon density waves, Phys. Rev. E 47 (1993) R2999–R3002.
[91] B.J. Tromberg, L.O. Svaasand, T.-T. Tsay, R.C. Haskell, Properties of photon density waves in multiple-scattering media, Appl. Opt. 32 (1993) 607–616.
[92] D.A. Boas, M.A. O'Leary, B. Chance, A.G. Yodh, Scattering of diffuse photon density waves by spherical inhomogeneities within turbid media: Analytic solution and applications, Proc. Natl. Acad. Sci. USA 91 (1994) 4887–4891.
[93] J.M. Schmitt, A. Knüttel, J.R. Knutson, Interference of diffusive light waves, J. Opt. Soc. Am. A 9 (1992) 1832–1843.
[94] B. Chance, K. Kang, L. He, J. Wang, E.M. Sevick, Highly sensitive object location in tissue models with linear in-phase and anti-phase multi-element optical arrays in one and two dimensions, Proc. Natl. Acad. Sci. USA 90 (1993) 3423–3427.
[95] H. Wabnitz, H. Rinneberg, Imaging in turbid media by photon density waves: spatial resolution and scaling relations, Appl. Opt. 36 (1997) 64–74.
[96] H. Jiang, K.D. Paulsen, U.L. Österberg, M.S. Patterson, Frequency-domain optical image reconstruction in turbid media: an experimental study of single-target detectability, Appl. Opt. 36 (1997) 52–63. *
[97] D.A. Boas, M.A. O'Leary, B. Chance, A.G. Yodh, Detection and characterization of optical inhomogeneities with diffuse photon density waves: a signal-to-noise analysis, Appl. Opt. 36 (1997) 75–92.
[98] X.D. Li, T. Durduran, A.G. Yodh, B. Chance, D.N. Pattanayak, Diffraction tomography for biochemical imaging with diffuse-photon density waves, Opt. Lett. 22 (1997) 573–575.
[99] A. Ishimaru, Wave Propagation and Scattering in Random Media, Academic Press, New York, 1978. ***
[100] H.C. van de Hulst, Multiple Light Scattering, Academic Press, New York, 1980. ***
[101] B. Chance, M. Maris, J. Sorge, M.S. Zhang, A phase modulation system for dual wavelength difference spectroscopy of haemoglobin deoxygenation in tissue, Proc. SPIE 1204 (1990) 481–491.
[102] J.R. Lakowicz, K. Berndt, Frequency domain measurement of photon migration in tissues, Chem. Phys. Lett. 166 (1990) 246–252.
[103] S.R. Arridge, M. Cope, D.T. Delpy, The theoretical basis for the determination of optical pathlengths in tissue: temporal and frequency analysis, Phys. Med. Biol. 37 (1992) 1531–1560.
[104] K. Michielsen, H. De Raedt, N. García, Computer simulation of time-gated transillumination and reflection of biological tissues and tissuelike phantoms, Med. Phys. 24 (1997) 1688–1695.
[105] M. Suzuki, General theory of fractal path integrals with applications to many-body theories and statistical physics, J. Math. Phys. 32 (1991) 400–407.
[106] H. De Raedt, K. Michielsen, Algorithm to solve the time-dependent Schrödinger equation for a charged particle in an inhomogeneous magnetic field: Application to the Aharonov-Bohm effect, Comput. Phys. 8 (1994) 600–607.
[107] G.D. Smith, Numerical Solution of Partial Differential Equations, Clarendon, Oxford, 1985.
[108] H. De Raedt, B. De Raedt, Applications of the generalized Trotter formula, Phys. Rev. A 28 (1983) 3575–3580.
[109] M. Suzuki, Decomposition formulas of exponential operators and Lie exponentials with some applications to quantum mechanics and statistical physics, J. Math. Phys. 26 (1985) 601–612. **
[110] W.A. Press, B.P. Flannery, S.A. Teukolsky, W.T. Vetterling, Numerical Recipes, Cambridge University Press, Cambridge, 1986.
[111] H. De Raedt, Product formula algorithms for solving the time-dependent Schrödinger equation, Comp. Phys. Rep. 7 (1987) 1–72.
[112] M. Abramowitz, I.A. Stegun (Eds.), Handbook of Mathematical Functions, National Bureau of Standards, Washington, DC, 1964.
[113] For the present purpose we employ rectangular boxes but the algorithm that we use can be modified to handle volumes of arbitrary shape.
[114] B.C. Wilson, G. Adam, A Monte Carlo model for the absorption and flux distribution of light in tissue, Med. Phys. 10 (1983) 824–830.

[115] P. van der Zee, D.T. Delpy, Simulation of the point spread function for light in tissue by a Monte Carlo technique, Adv. Exp. Med. Biol. 215 (1987) 179–191.
[116] S.L. Jacques, Time-resolved reflectance spectroscopy in turbid tissues, IEEE Trans. Biom. Eng. 36 (1989) 1155–1161.
[117] S.T. Flock, M.S. Patterson, B.C. Wilson, D.R. Wyman, Monte Carlo modeling of light propagation in highly scattering tissues. I. Model predictions and comparison with diffusion theory, IEEE Trans. Biom. Eng. 36 (1989) 1162–1168.
[118] S.T. Flock, B.C. Wilson, M.S. Patterson, Monte Carlo modeling of light propagation in highly scattering tissues. II. Comparison with measurements in phantoms, IEEE Trans. Biom. Eng. 36 (1989) 1169–1173.
[119] Y. Hasegawa, Y. Yamada, M. Tamura, Y. Nomura, Monte Carlo simulation of light transmission through living tissues, Appl. Opt. 30 (1991) 4515–4520. *
[120] J.C. Hebden, R.A. Kruger, Transillumination imaging performance: a time of flight imaging system, Med. Phys. 17 (1990) 351–356.
[121] E.B. de Haller, C. Depeursinge, Simulation of time-resolved breast transillumination, Med. Biol. Eng. Comput. 31 (1993) 165–170.
[122] R. Graaff, M.H. Koelink, F.F.M. de Mul, W.G. Zijlstra, A.C.M. Dassel, J.G. Aarnoudse, Condensed Monte Carlo simulations for the description of light transport, Appl. Opt. 32 (1993) 426–434.
[123] E. Tinet, S. Avrillier, J.M. Tualle, Fast semianalytical Monte Carlo simulation for time-resolved light propagation in turbid media, J. Opt. Soc. Am. A 13 (1996) 1903–1915.
[124] R.F. Bonner, R. Nossal, S. Havlin, G.H. Weiss, Model for photon migration in turbid biological media, J. Opt. Soc. Am. A 4 (1987) 423–432.
[125] A.H. Gandjbakhche, H. Taitelbaum, G.H. Weiss, Random walk analysis of time-resolved transillumination measurements in optical imaging, Physica A 200 (1993) 212–221.
[126] M.S. Patterson, B. Chance, B.C. Wilson, Time resolved reflectance and transmittance for the noninvasive measurement of tissue optical properties, Appl. Opt. 28 (1989) 2331–2336. ***
[127] S.R. Arridge, M. Schweiger, M. Hiraoka, D.T. Delpy, A finite element approach for modeling photon transport in tissue, Med. Phys. 20 (1993) 299–309. *
[128] M. Schweiger, S.R. Arridge, M. Hiraoka, D.T. Delpy, The finite element method for the propagation of light in scattering media: Boundary and source conditions, Med. Phys. 22 (1995) 1779–1792.
[129] S.R. Arridge, M. Schweiger, Direct calculation of the moments of the distribution of photon time of flight in tissue with a finite element method, Appl. Opt. 34 (1995) 2683–2687.
[130] K.D. Paulsen, H. Jiang, Spatially varying optical property reconstruction using a finite-element diffusion equation approximation, Med. Phys. 22 (1995) 691–701.
[131] R. Model, M. Orlt, M. Walzel, R. Hümlich, Reconstruction algorithm for near-infrared imaging in turbid media by means of time domain data, J. Opt. Soc. Am. A 14 (1997) 313–324. *
[132] M.R. Jones, S.G. Proskurin, Y. Yamada, Y. Tanikawa, Application of the zooming method in near-infrared imaging, Phys. Med. Biol. 42 (1997) 1993–2009.
[133] S. Havlin, J.E. Kiefer, B. Trus, G.H. Weiss, R. Nossal, Numerical method for studying the detectability of inclusions hidden in optically turbid tissue, Appl. Opt. 32 (1993) 617–627.
[134] K. Michielsen, H. De Raedt, N. García, Time-gated transillumination and reflection by biological tissues and tissuelike phantoms: Simulation versus experiment, J. Opt. Soc. Am. A 14 (1997) 1867–1871.
[135] In the TDDE the speed of light v sets only the time scale. To rescale the results presented in this paper to the case where the speed of light in the medium is v', multiply all times by v/v'.
[136] B.C. Wilson, M.S. Patterson, The physics of photodynamic therapy, Phys. Med. Biol. 31 (1986) 327–360. *
[137] S.L. Jacques, S.A. Prahl, Modeling optical and thermal distributions in tissue during laser irradiation, Lasers Surg. Med. 6 (1987) 494–503.
[138] F.H. Long, R.R. Anderson, T.F. Deutsch, Pulsed photothermal radiometry for depth profiling of layered media, Appl. Phys. Lett. 51 (1987) 2076–2078.
[139] R.R. Anderson, H. Beck, U. Bruggeman, W. Farinelli, S.L. Jacques, J.A. Parrish, Pulsed photothermal radiometry in turbid media: Internal reflection of backscattered radiation strongly influences optical dosimetry, Appl. Opt. 28 (1989) 2256–2262.
[140] S.A. Prahl, I.A. Vitkin, Determination of optical properties of turbid media using pulsed photothermal radiometry, Phys. Med. Biol. 37 (1992) 1203–1217.

[141] A.A. Oraevsky, S.L. Jacques, F.K. Tittel, Determination of tissue optical properties by piezoelectric detection of laser induced stress waves, in: S.L. Jacques (Ed.), Laser Tissue Interaction IV, Proc. Soc. Photo-Opt. Instrum. Eng. 1882 (1993) 86–101.
[142] J. Langerholc, Beam broadening in dense scattering media, Appl. Opt. 21 (1982) 1593–1598.
[143] R.A.J. Groenhuis, H.A. Ferwerda, J.J. Ten Bosch, Scattering and absorption of turbid materials determined from reflection measurements. 1. Theory, Appl. Opt. 22 (1983) 2456–2462.
[144] R.A.J. Groenhuis, J.J. Ten Bosch, H.A. Ferwerda, Scattering and absorption of turbid materials determined from reflection measurements. 2. Measuring method and calibration, Appl. Opt. 22 (1983) 2463–2467.
[145] R. Bays, G. Wagnières, D. Robert, D. Braichotte, J.-F. Savary, P. Monnier, H. van den Bergh, Clinical determination of tissue optical properties by endoscopic spatially resolved reflectometry, Appl. Opt. 35 (1996) 1756–1766.
[146] W. Cheong, S.A. Prahl, A.J. Welch, A review of the optical properties of biological tissues, IEEE J. Quantum Electron. 26 (1990) 2166–2185.
[147] B.C. Wilson, Measurement of tissue optical properties: methods and theory, in: A.J. Welch, M.J.C. van Gemert (eds.), Optical-Thermal Response of Laser-Irradiated Tissue, Plenum press, New York, 1995, pp. 233–274.
[148] R. Cubeddu, A. Pifferi, P. Taroni, A. Torricelli, G. Valentini, Experimental test of theoretical models for time-resolved reflectance, Med. Phys. 23 (1996) 1625–1633. **
[149] P. Kubelka, New contributions to the optics of intensily light-scattering materials. Part I, J. Opt. Soc. Am. 38 (1948) 448–457.
[150] D. Contini, F. Martelli, G. Zaccanti, Photon migration through a turbid slab described by a model on diffusion approximation. I. Theory, Appl. Opt. 36 (1997) 4587–4599.
[151] F. Martelli, D. Contini, A. Taddeucci, G. Zaccanti, Photon migration through a turbid slab described by a model on diffusion approximation. II. Comparison with Monte Carlo results, Appl. Opt. 36 (1997) 4600–4612.
[152] S.A. Prahl, M.J.C. van Gemert, A.J. Welch, Determining the optical properties of turbid media by using the adding-doubling method, Appl. Opt. 32 (1993) 559–568.
[153] M.H. Eddowes, T.N. Mills, D.T. Delpy, Monte Carlo simulations of coherent backscatter for identification of the optical coefficients of biological tissues in vivo, Appl. Opt. 34 (1995) 2261–2267.
[154] A. Kienle, M.S. Patterson, Determination of the optical properties of turbid media from a single Monte Carlo simulation, Phys. Med. Biol. 41 (1996) 2221–2227.
[155] A.H. Gandjbakhche, R. Nossal, R.F. Bonner, Scaling relationships for theories of anisotropic random walks applied to tissue optics, Appl. Opt. 32 (1993) 504–516.
[156] T.J. Farrell, M.S. Patterson, B. Wilson, A diffusion theory model of spatially resolved, steady-state diffuse reflectance for the non-invasive determination of tissue optical properties in vivo, Med. Phys. 19 (1992) 879–888.
[157] A.H. Hielscher, S.L. Jacques, L. Wang, F.K. Tittel, The influence of boundary conditions on the accuracy of diffusion theory in time-resolved reflectance spectroscopy of biological tissues, Phys. Med. Biol. 40 (1995) 1957–1975.
[158] W.M. Star, J.P.A. Marijnissen, H. Jansen, M. Keijzer, M.J.C. van Gemert, Light dosimetry for photodynamic therapy by whole bladder wall irradiation, Photochem. Photobiol. 46 (1987) 619–624.
[159] C.J.M. Moes, M.J.C. van Gemert, W.M. Star, J.P.A. Marijnissen, S.A. Prahl, Measurements and calculations of the energy fluence rate in a scattering and absorbing phantom at 633 nm, Appl. Opt. 28 (1989) 2292–2296.
[160] H.J. van Staveren, C.J.M. Moes, J. van Marle, S.A. Prahl, M.J.C. van Gemert, Light scattering in intralipid-10% in the wavelength range 400–1100 nm, Appl. Opt. 30 (1991) 4507–4514.
[161] S.T. Flock, S.L. Jacques, B.C. Wilson, W.M. Star, M.J.C. van Gemert, Optical properties of intralipid: a phantom medium for light propagation studies, Lasers Surg. Med. 12 (1992) 510–519.
[162] A.H. Hielscher, J.R. Mourant, I.J. Bigio, Influence of particle size and concentration on the diffuse backscattering of polarized light from tissue phantoms and biological cell suspensions, Appl. Opt. 36 (1997) 125–135.
[163] S.J. Madsen, B.C. Wilson, M.S. Patterson, Y.D. Park, S.L. Jacques, Y. Hefetz, Experimental tests of a simple diffusion model for the estimation of scattering and absorption coefficients of turbid media from time-resolved diffuse reflectance experiments, Appl. Opt. 31 (1992) 3509–3517.
[164] K. Symanzik, Proof and refinements of an inequality of Feynman, J. Math. Phys. 6 (1965) 1155–1156.
[165] N. Dunford, J.T. Schwartz, Linear Operators, Interscience, New York, 1958.
[166] J. Przeslawski, J. Calsamiglia, N. García, H. De Raedt, K. Michielsen, M. Nieto-Vesperinas, Detection of 1 mm size hidden objects in tissue-like phantoms by backscattered diffused light, Appl. Opt. (in press).